A Search for $t\bar{t}$ Resonances in the Lepton Plus Jets Channel from Proton-Proton Collisions at $\sqrt{s} = 8$ TeV with the ATLAS Detector

by

Christopher Pollard

Department of Physics
Duke University

Date: ______________________
Approved:

____
Ashutosh Kotwal, Supervisor

____
Ayana Arce

____
Shailesh Chandrasekharan

____
Gleb Finkelstein

____
Thomas Mehen

Dissertation submitted in partial fulfillment of the requirements for the degree of
Doctor of Philosophy in the Department of Physics
in the Graduate School of Duke University
2014

Abstract

A Search for $t\bar{t}$ Resonances in the Lepton Plus Jets Channel from Proton-Proton Collisions at $\sqrt{s} = 8$ TeV with the ATLAS Detector

by

Christopher Pollard

Department of Physics
Duke University

Date: ______________________
Approved:

____
Ashutosh Kotwal, Supervisor

____
Ayana Arce

____
Shailesh Chandrasekharan

____
Gleb Finkelstein

____
Thomas Mehen

An abstract of a dissertation submitted in partial fulfillment of the requirements for
the degree of Doctor of Philosophy in the Department of Physics
in the Graduate School of Duke University
2014

Abstract

A search for the resonant production of top quark pairs in proton-proton collisions at a center-of-mass energy of 8 TeV is presented. The Large Hadron Collider delivered 14 inverse femtobarns of collision data which were collected by the ATLAS detector. The lepton plus jets final state is used, and the top pair invariant mass spectrum is probed for local excesses above the Standard Model background prediction. No evidence for resonant top pair production is found. 95% credibility limits are set on the cross section times branching ratio of two signal benchmarks. A narrow leptophobic topcolor Z' boson decaying to top quark pairs and the Kaluza-Klein excitation of the gluon in a Randall-Sundrum model are excluded for masses below 1.8 and 2.0 TeV, respectively. The expected sensitivity to new physics at ATLAS with proton-proton collisions delivered by a High Luminosity Large Hadron Collider is also presented. The feasibility of analyses studying vector boson scattering, exotic resonances, and an extended Higgs sector with up to 3000 inverse femtobarns of integrated luminosity is investigated based on the fast simulation of proton-proton collisions at a center-of-mass energy of 14 TeV.

Contents

List of Tables

List of Figures

List of Abbreviations

Abbreviations

ATLAS	A Toroidal LHC ApparatuS
LHC	Large Hadron Collider
SM	Standard Model
BSM	Beyond the Standard Model
QCD	Quantum Chromodynamics
MC	Monte Carlo
KK	Kaluza-Klein
RS	Randall-Sundrum
PDF	Parton Distribution Function
SCT	Silicon Tracker
TRT	Transition Radiation Tracker
EM	Electromagnetic
LO	Leading Order
NLO	Next-to Leading Order

Acknowledgements

The work presented in this thesis would not have been possible without the support of my friends, family, and colleagues. I would first like to thank my Ph.D. advisor, Professor Ashutosh Kotwal, for the guidance and freedom he has given me over the last five years at Duke. The feedback I received from the members of my committee, comprised of Professors Arce, Chandrasekharan, Finkelstein, Mehen, and Wu, has also been invaluable.

The members of Duke ATLAS group have been a pleasure to work with since my arrival in Durham. Professors Arce, Goshaw, and Kruse have always been willing to answer my questions about not only physics, but also research funding, career choices, and local food, beer, and chocolate. My CERN roommates Andrea and Doug have my gratitude for their physics and software discussions, not to mention their advice for adjusting to life in France. I am forever indebted to Miriam and Jenni, who always made certain I never went into the red during my travels. None of the research presented herein would be possible without the generous support of the Department of Energy Office of Science for the ATLAS group at Duke.

Working within ATLAS would have been a far less productive and enjoyable experience without the people I have met along the way. Thank you first to my boosted and dilepton $t\bar{t}$ resonance partners-in-crime, Berndt, Bertrand, Emily, Elin, Marcel, Michele, Oliver, Sarah, and Stephen, who helped me keep my head above water during my first year of real research. James, Jiahang, and Samuel have given me indispensable feedback and guidance as I have continued my studies. I am particularly thankful for my many CERN friends who were not directly involved in my research, but who forced me to socialize, travel, and enjoy myself while away from home.

To my ATLAS officemates and friends—Bennie C, Dave, Kevin “K1”, Chen, Lei, and Mia “The Cat”—I am grateful for all the time we had (and will have) together. I am equally thankful for the support of my friends outside the ATLAS group, especially Aline, Bonnie, Jon, Kevin “K2”, Mallory, Sarah, Sean, Sukrit, and Venkitesh. I would also like to acknowledge those not affiliated with the department or the university—particularly my soccer teammates, neighbors, and college friends: your perspective from outside my field of research was invaluable.

My family has always been immensely supportive of me and my adventures for the last twenty-eight years. My parents, Mark and Nan, and brother, Stephen, never questioned my ambitions and helped me realize them. My aunts, uncles, cousins, and grandparents have gone out of their way to be interested in my endeavors and to voice their encouragement, and for that I am extremely grateful.

Finally, I would like to thank the numerous professors, teachers, administrators, staff members, friends, and colleagues that have helped make me who I am but whose contributions I cannot include in a limited number of words. You have my gratitude.

1

Introduction

The Standard Model has been immensely successful at describing experimental results in particle physics. The recent discovery of the Higgs boson was the latest observation to confirm what it had predicted well in advance.

However, the Standard Model is known to be an incomplete description of nature. Colliders such as the Tevatron and the Large Hadron Collider have been assembled to test the Standard Model at high energy scales in search of discrepancies between its predictions and experimental observation. Although no significant deviations between the two have yet been exposed in the realm of particle physics, dark matter, gravity, and the hierarchy problem all hint that there is a more fundamental theory waiting to be uncovered.

The top quark is peculiar among the fermions in that its mass is on the order of the weak energy scale. This not only makes it an interesting subject of study in and of itself, it suggests that it may have a larger role to play than it has been given in the Standard Model. In this thesis a search for the resonant production of top quark pairs beyond the Standard Model in proton-proton collisions is presented. Collision data were collected from the Large Hadron Collider with the ATLAS detector, and the subsequent analysis and interpretation of these data are presented herein.

The document is organized as follows. Chapter 2 introduces the Standard Model (SM) as well as extensions to the Standard Model that are tested in this thesis. The physics of proton collisions and the production of top quark pairs at the Large Hadron Collider (LHC) are also discussed. Chapter 3 describes the two primary components of the experimental setup: the LHC and the ATLAS detector. The ATLAS subdetectors are discussed in detail. Monte Carlo (MC) techniques are employed to simulate LHC proton collisions and the interactions of the resulting particles with the experimental apparatus. This is described in Chapter 4. The reconstruction of particles traversing ATLAS is discussed in Chapter 5. The focus of this thesis is Chapter 6, in which a search for resonant top pair production beyond the Standard Model (BSM) is presented: the analysis strategy, estimation of the background processes, uncertainties in the measurement, and final results. Chapter 7 describes techniques developed for the reconstruction of energetic top quarks. Finally, Chapter 8 details studies of the expected ATLAS sensitivity to BSM physics under the High Luminosity LHC upgrade scenario.

2

Theoretical Background

This chapter gives a brief introduction to the Standard Model, models beyond the Standard Model relevant to this thesis, and the physics of proton collisions.

2.1 The Standard Model

The Standard Model (SM) of particle physics is the most widely accepted theory for predicting the interactions of elementary particles. It describes all known fundamental particles and the strong and electroweak forces.

2.1.1 Particles and interactions

Particles in the SM are split into two categories: fermions with half-integer spin and bosons with integer spin. The fermions are further divided into those that have color and interact via the strong force (quarks), and those that do not (leptons). There are three generations of both quarks and leptons which are generally grouped in order of increasing mass. This is shown in Table 2.1. Quarks have non-integer charge and are grouped into "up-type" (u, c, t, with charge $+2/3$) and "down-type" (d, s, b, with charge $-1/3$) varieties. Leptons are grouped by their charges: electrons (e),

Table 2.1: The Standard Model fermions.

Quarks	$u^{+2/3}$ $d^{-1/3}$	$c^{+2/3}$ $s^{-1/3}$	$t^{+2/3}$ $b^{-1/3}$
Leptons	e^{-} ν_e	μ^{-} ν_μ	τ^{-} ν_τ

muons (μ), and tau leptons (τ) carry negative charge, and there is a corresponding chargeless neutrino (ν_ℓ) for each charged lepton. Antiparticles have identical masses but opposite charges. The fermion type is sometimes referred to as its flavor.

There are four vector bosons in the Standard Model which mediate interactions between particles. Gluons (g) interact with quarks and other gluons through the strong force described by quantum chromodynamics (QCD); they are massless. Photons (γ) and the massive weak bosons ($W^{\pm}$, Z) mediate the electroweak interaction, a unification of the electromagnetic and weak theories by Glashow, Salam, and Weinberg [1, 2, 3]. The W and Z bosons interact with all fermion flavors and each other. Photons are massless and only couple the charged fermions and the W boson.

The Higgs boson, which was the last predicted SM particle that had not been confirmed, was recently observed by experiments using collision data from the Large Hadron Collider (LHC) [4, 5]. In the SM, interactions with the Higgs field are responsible for the masses of quarks, charged leptons, and the W and Z bosons.

2.1.2 Quantum chromodynamics

Quantum chromodynamics describes the interactions of particles with a color quantum number: the quarks and gluons. Its dynamics are determined by the SU(3) gauge symmetry group. Quarks and gluons have never been observed as free particles; rather, they hadronize into mesons and baryons on the timescale $1/\Lambda_{QCD}$, where $\Lambda_{QCD} \sim 200$ MeV is the QCD scale. All mesons and baryons (or, collectively, hadrons) are color singlet.

The strength of QCD interactions is dictated by the strong coupling, α_S, which runs with the square of the momentum transfer, Q^2, between interacting particles. For interactions with a low momentum transfer α_S is large, and QCD predictions are difficult to calculate due to the non-perturbative nature of the interaction. At high momentum transfer, however, α_S is sufficiently small for the computation of rigorous perturbative predictions. The coupling α_S diverges in perturbation theory at Λ_{QCD}.

2.1.3 Electroweak interactions

The Standard Model electroweak theory is governed by the SU$(2)_L\times$U(1) symmetry groups that characterize the interactions of the electroweak vector bosons with quarks and leptons. The generators of these groups are the weak isospin, T, and the hypercharge, $Y = 2(Q - T_3)$, where Q is the electric charge and T_3 is the third component of the weak isospin operator. g_1 and g_2 are the couplings corresponding to the U(1) and SU$(2)_L$ symmetry groups.

The physical gauge boson fields can be written in terms of the pure SU$(2)_L$ and U(1) bosons, W^i_μ and B_μ:

$$A_\mu = B_\mu \cos\theta_W + W^3_\mu \sin\theta_W \tag{2.1}$$

$$W^+_\mu = \frac{1}{\sqrt{2}}(W^1_\mu - iW^2_\mu) \tag{2.2}$$

$$W^-_\mu = \frac{1}{\sqrt{2}}(W^1_\mu + iW^2_\mu) \tag{2.3}$$

$$Z_\mu = -B_\mu \sin\theta_W + W^3_\mu \cos\theta_W \tag{2.4}$$

where A_μ is the photon field, $W^\pm_\mu$ are the W boson fields, Z_μ is the Z boson field, and $\theta_W = \arctan(g_1/g_2) = \arccos(m_W/m_Z)$ is the weak mixing angle. Since the SU$(2)_L$ symmetry only applies to left-handed fermions, right-handed fermions do not interact with the W bosons and only interact with the Z boson through the original U(1) B_μ

boson.

The Higgs mechanism describes the process of electroweak symmetry breaking (EWSB), by which the W and Z bosons acquire mass. As a direct result, the Higgs boson emerges as an excitation above its vacuum expectation value, v. A summary of the fermion Yukawa couplings, y_f, to the Higgs is shown in Figure 2.1 [6]. Fermion masses are defined in terms of the Yukawa couplings as

$$m_f = \frac{v}{\sqrt{2}} y_f. \tag{2.5}$$

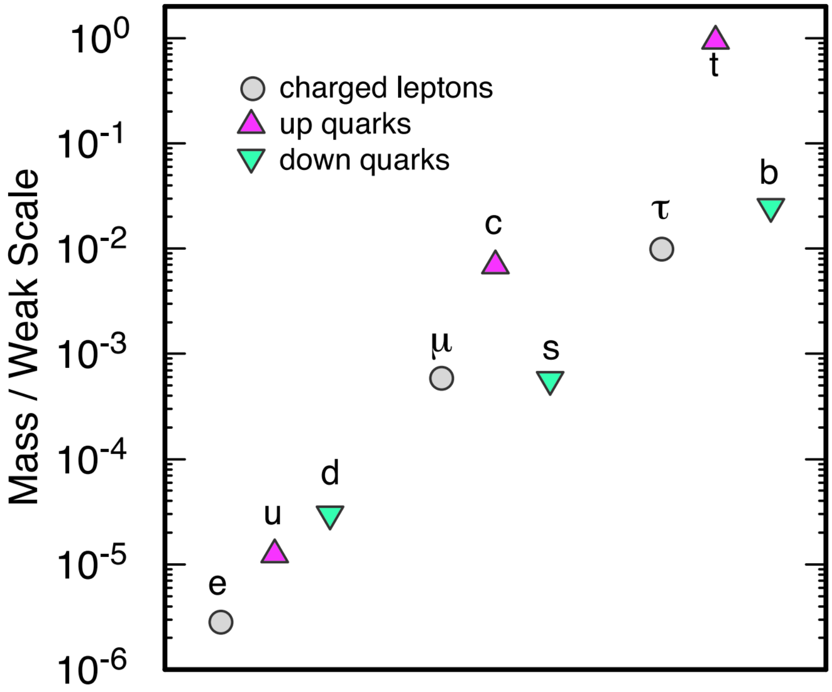

FIGURE 2.1: Yukawa couplings of the quarks and charged leptons to the Higgs boson, $y_f = m_f/(v/\sqrt{2})$. Note the range of the scales covered. The top quark is the only fermion with a Yukawa coupling on the order of the weak scale, $v/\sqrt{2}$ [6].

2.2 Models with $t\bar{t}$ resonances

Although the Standard Model has been very successful at predicting and describing recent experimental results in particle physics, it does not explain all known physical phenomena. The gravitational force is yet to be successfully integrated into the framework of quantum field theory (QFT), and dark matter, dark energy, the asymmetry between matter and antimatter, and the discrepancy between the electroweak (~ 1 TeV) and Planck ($\sim 10^{16}$ TeV) scales (the hierarchy problem) all pose questions that the Standard Model cannot answer at present.

Numerous models which tackle one or more of these issues have been developed, and a subset of these predict significant deviations from the Standard Model at the TeV scale. Colliders such as the Tevatron and the LHC and their associated detectors aim to carefully probe the predictions of new models by producing very energetic particle interactions. Two such models that are used as benchmarks in the $t\bar{t}$ resonances search presented in Chapter 6 are introduced in the following sections.

2.2.1 Massive Z' boson through topcolor assisted technicolor

The top quark's large mass suggests that it may play a role in the mechanism for electroweak symmetry breaking. Topcolor assisted technicolor models generate EWSB through the formation of a condensate of top quarks [7, 8, 9].

In these models, there are two SU(3) gauge symmetry groups, one which couples preferentially, for example, to the first- and second-generation quarks ($\mathrm{SU}(3)_1$), and one preferentially to the third ($\mathrm{SU}(3)_2$). These symmetries are broken to yield the $\mathrm{SU}(3)_{QCD}$ gauge symmetry of the strong interaction: $\mathrm{SU}(3)_1 \times \mathrm{SU}(3)_2 \rightarrow \mathrm{SU}(3)_{QCD}$.

However, this formulation predicts degenerate masses of the top and bottom quarks at approximately 600 GeV [10]. Various corrective methods have been implemented to break the mass degeneracy and reduce the top mass to its observed value. The salient feature of each of them is the introduction of, and subsequent breaking of, additional U(1) gauge symmetry groups. These new symmetry groups, $\mathrm{U}(1)_1$ and $\mathrm{U}(1)_2$, also couple preferentially to the first two generations and the third generation, respectively, and are broken to yield the U(1) gauge symmetry of the Standard Model: $\mathrm{U}(1)_1 \times \mathrm{U}(1)_2 \rightarrow \mathrm{U}(1)_Y$. This gives rise to a new massive vector boson that, in order to break the degeneracy of the top and bottom quarks with the appropriate mass hierarchy, results in an attractive force for $t\bar{t}$ condensates and a repulsive one for $b\bar{b}$ condensates. Due to its similarities with the SM Z boson—it is a neutral, massive vector boson—it is referred to as a Z' boson.

There is some freedom in the model: the pairing of generations in the symmetry groups is arbitrary. The combination with the most enhanced production cross sections at a proton collider makes the first and third generations couple strongly to the first $\mathrm{SU}(3)_1 \times \mathrm{U}(1)_1$, while the second generation of quarks to the second set of symmetry groups. This is named Model IV in Ref. [11].

The width of the new Z' boson is also a free parameter in the model. Figure 2.2 shows the cross section times branching ratio of the topcolor Z' boson decaying to $t\bar{t}$ pairs for $\sqrt{s} = 8$ TeV proton-proton collisions.

2.2.2 Kaluza-Klein gluon excitation in Randall-Sundrum models

In the Standard Model, particle fields are confined to the conventional four dimensions of space-time. However, the possibility of small, compact additional spatial dimensions has not been ruled out by current experiments. The momentum of a particle propagating in an extra dimension will manifest itself as apparent additional mass, and the mass spectrum will be discrete if the dimension is compact. These discrete modes are called Kaluza-Klein excitations [12, 13].

Randall-Sundrum (RS) models address the hierarchy problem through the introduction of warped extra dimensions [14]. The extra dimension, or “bulk,” connects

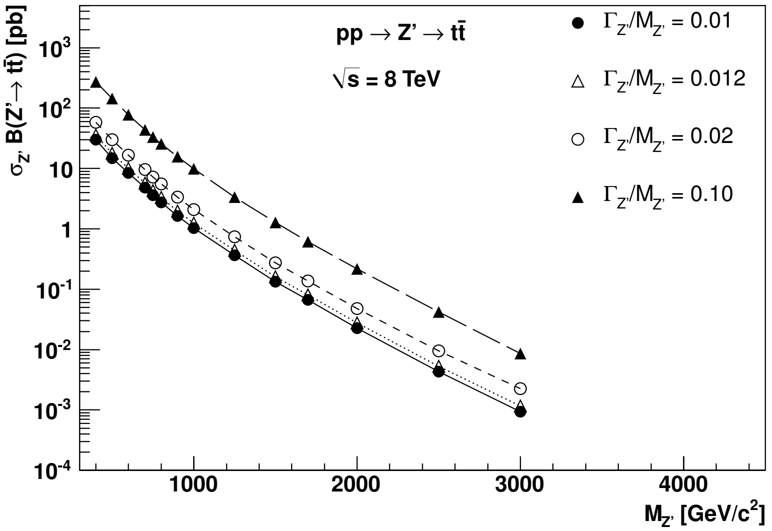

FIGURE 2.2: Cross sections times branching ratios of the topcolor $Z' \to t\bar{t}$ in $\sqrt{s} =$ 8 TeV proton-proton collisions for various masses and widths of the new boson [10].

the usual TeV scale space-time, the infrared (IR) "brane," with the observed spectrum of particle masses to a Planck scale UV brane, on which the gravitational and electroweak scales are unified. The metric in this space is defined as

$$ds^2 = e^{-2k|y|}\eta_{\mu\nu}dx^{\mu}dx^{\nu} - dy^2, \tag{2.6}$$

where k is the curvature of the warped extra dimension, and y is the coordinate in the extra dimension. $y = 0$ is defined as the location of the UV brane, and the IR brane is at $y = r$.

Due to the exponential dependence of the metric on y, masses on the TeV scale brane, m, are related to the more fundamental masses on the Planck scale brane, m_0, by

$$m = e^{-kr\pi}m_0. \tag{2.7}$$

Standard model particles are mostly localized close to the UV brane to account for their small masses; the top quark is accordingly farthest from $y = 0$.

The first indication that such an extra dimension exists will likely be through observation of the Kaluza-Klein excitation of Standard Model fields in the bulk. At the LHC, the production of high-energy gluons makes the bulk excitation of the gluon (g_{KK}) have a relatively higher cross section than other excitations. Since the gluon excitation is localized near the IR brane, the wave function overlap between the g_{KK} and the top quark is much higher than its overlap with other particles. Therefore, the dominant decay mode of the Kaluza-Klein gluon in this particular model is to $t\bar{t}$ pairs, provided the mass of the first excitation is at least twice m_{top}.

Figure 2.3 shows the total production cross section of Kaluza-Klein gluons and their branching ratios for this model as a function of the apparent mass of the excitation.

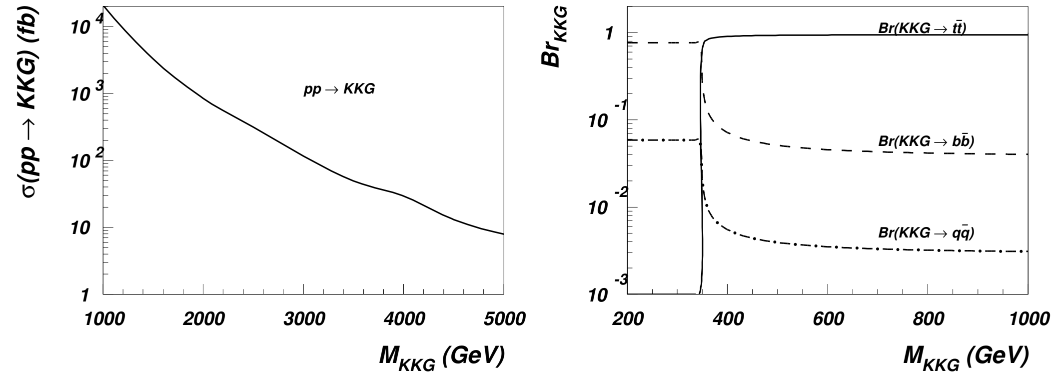

FIGURE 2.3: The production cross section (left) and branching ratios (right) of Randall-Sundrum Kaluza-Klein gluon excitations in LHC proton-proton collisions as a function of the g_{KK} mass [15].

2.3 The physics of proton collisions

Protons are composite particles, made up of constituent quarks and gluons which, at sufficient momentum transfer, individually undergo interactions with other particles.

In proton collisions these interactions are described chiefly by quantum chromodynamics.

2.3.1 Low-Q^2 QCD at the LHC

Although the LHC was designed to probe physics at center-of-mass energies well above ~ 10 GeV, most proton collisions at the LHC involve momentum exchange that is below this scale. When low-energy collisions take place simultaneously with the high-energy collisions, their effect on the reconstruction of the high-energy collision must be taken into account. These simultaneous collisions are known as pile-up events, and their cross sections and kinematics are calculated using models implemented with Monte Carlo techniques [16].

2.3.2 Hard scatter events

At high momentum transfer, the collision of two protons can be treated as a direct interaction between their constituent quarks and gluons (partons). To model this correctly, the internal structure of the proton must be understood.

This is chiefly accomplished through the deep inelastic scattering (DIS) of a lepton and a proton. In DIS experiments, a lepton interacts directly with a parton inside the proton; the interaction cross section and scattered lepton kinematics as a function of the momentum transferred are sensitive to the proton's structure. The data from ep experiments (e.g. ZEUS and H1 at HERA [17]), μp experiments (BCDMS [18], E665 [19]), and νp experiments (CHORUS [20], NuTeV [21]), are used to derive parton distribution functions (PDFs). PDFs describe the probability of a parton of a certain flavor to carry the fractional momentum, x, of the proton at a momentum transfer Q^2.

Results from fixed target experiments, lepton-proton colliders, and hadron colliders (primarily for high-Q^2) are combined and fit to obtain an accurate representation of the proton structure over a range of x and Q^2. Figure 2.4 shows the MSTW2008NNLO PDFs [22] at two exemplary energy scales.

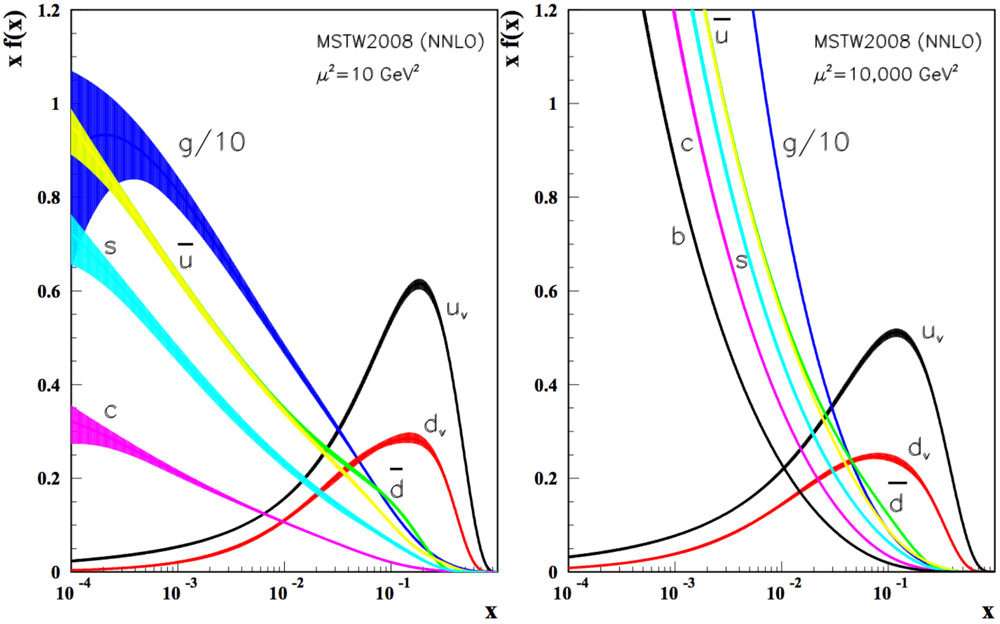

FIGURE 2.4: Distributions of x times the parton distributions $f(x)$ and their associated uncertainties using the MSTW2008NNLO parameterization at a scale of 10 GeV^2 (left) and 10,000 GeV^2 (right) [23].

2.3.3 Top quark pair production and decays

High-Q^2 collisions at the LHC produce a variety of final state particles at different rates. Figure 2.5 summarizes the cross sections of a selection of the SM processes as a function of the center-of-mass energy of the collision.

At leading order there are two primary production processes for $t\bar{t}$ pairs: quark-antiquark annihilation and the fusion of two gluons. Gluon-gluon fusion accounts for about 80% of the $t\bar{t}$ production cross section at the LHC. The diagrams corresponding to these processes are shown in Figure 2.6. The total $t\bar{t}$ cross section with $\sqrt{s} = 8$ TeV proton-proton collisions is $238.1^{+23.3}_{-25.2}$ pb at next-to-next-to leading order according to HATHOR [25].

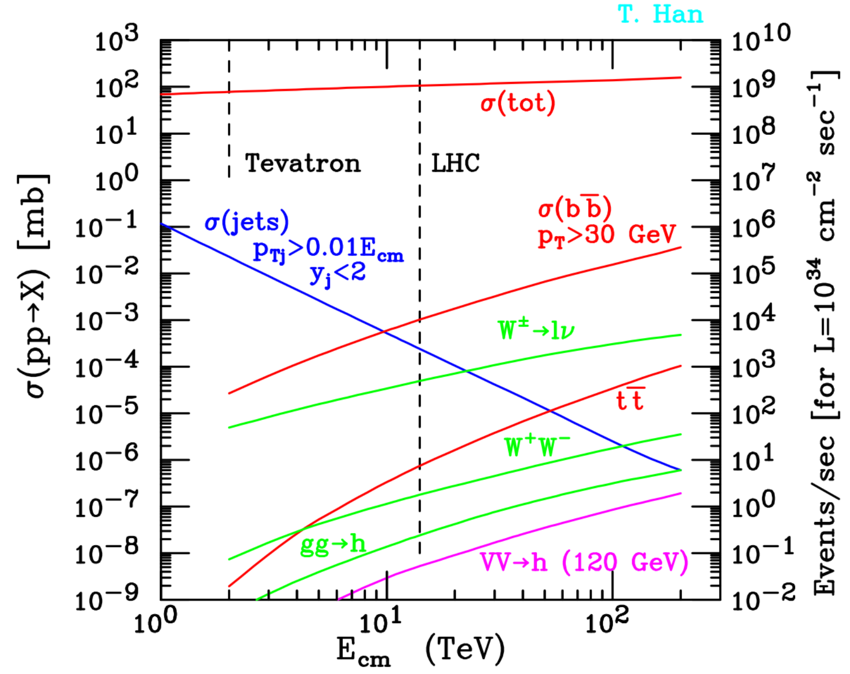

FIGURE 2.5: Production cross sections of selected SM processes in proton collisions as a function of the proton-proton center-of-mass energy [24]. Processes whose production is dominated by QCD interactions are colored red or blue. Electroweak processes are green and magenta.

The mass of the top quark as measured by the Tevatron experiments is 173.20 ± 0.87 GeV [26], and its lifetime is on the order of 10^{-24} s. Since its lifetime is smaller than the QCD timescale, $1/\Lambda_{QCD}$, the top quark does not hadronize, but immediately decays to a W boson and a b quark with a branching fraction of greater than 99.9%. Because of this, the top quark decay mode is almost entirely dependent on the decay of its W boson daughter.

W bosons decay approximately 10% of the time to each charged lepton and its corresponding neutrino. The other 70% of W decays result in a quark and antiquark of different flavors. Given the W boson decay modes, about 44% of $t\bar{t}$ pairs result in the production of exactly one lepton. Figure 2.7 illustrates the $t\bar{t}$ decay modes pictorially.

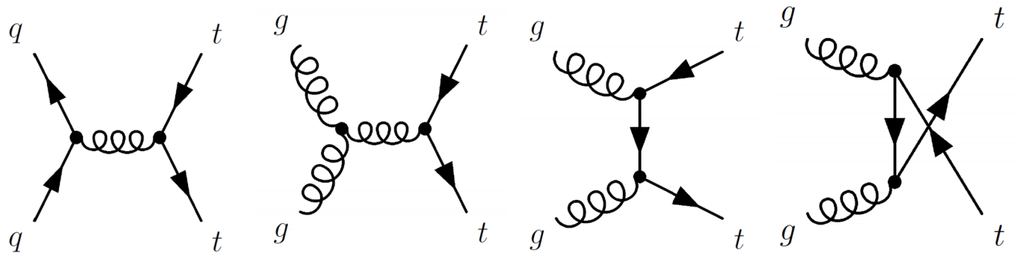

FIGURE 2.6: The dominant production modes of $t\bar{t}$ pairs at the LHC [27]. The left-most diagram illustrates quark-antiquark annihilation to produce $t\bar{t}$ pairs. The other three plots, from left to right, show s-, t-, and u-channel $t\bar{t}$ production from the fusion of two gluons.

$t\bar{t}$ events are therefore characterized by the production of two high-p_T b quarks and two W bosons. The analysis presented in Chapter 6 reconstructs $t\bar{t}$ pairs in the single lepton channel, in which one W boson decays to a charged lepton and a neutrino and the other to two quarks.

Since the initial state particles in proton collisions are quarks and gluons, leptons and neutrinos are only created through electroweak processes at the LHC. The dominant non-$t\bar{t}$ background process which mimics $t\bar{t}$ events in the single lepton channel is W+jets production, wherein the W boson decays leptonically. Although the $W\text{+jets} \rightarrow \ell\nu\text{+jets}$ cross section is larger than that of $t\bar{t}$ at the LHC, additionally searching for a final state consistent with 4 quarks, two of them being high-p_T b quarks, reduces the W+jets background significantly.

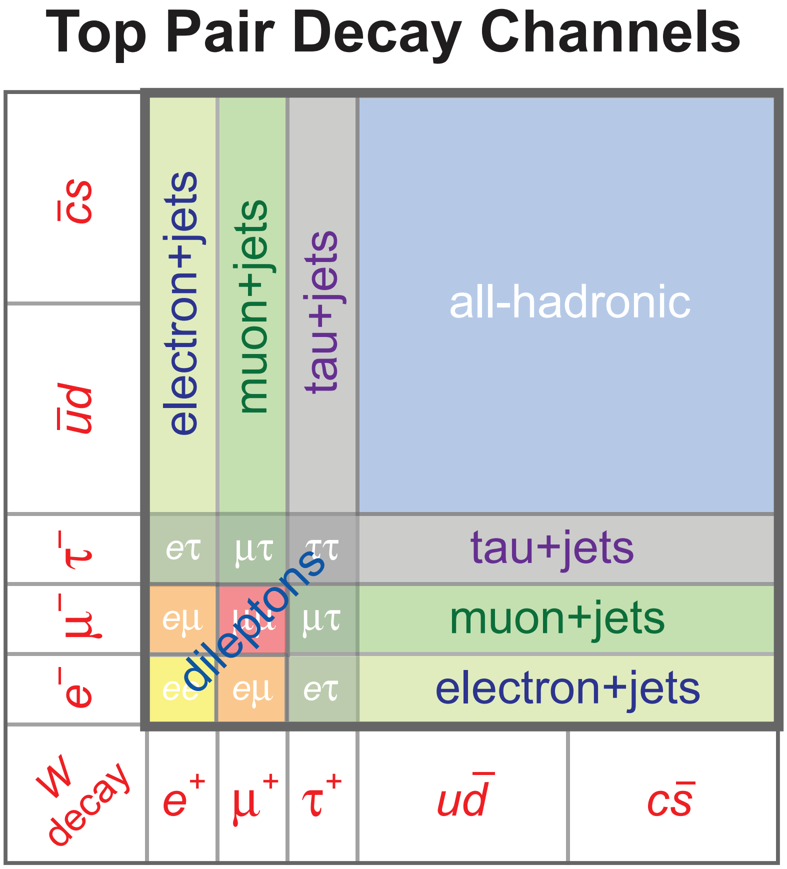

FIGURE 2.7: Decay modes of $t\bar{t}$ pairs. The dilepton, lepton plus jets, and all-hadronic decay modes account for 10.5, 43.8, and 45.7% $t\bar{t}$ decays, respectively.

3

The Large Hadron Collider and the ATLAS Detector

3.1 The Large Hadron Collider

The Large Hadron Collider accelerates two beams of protons to 4 TeV each, producing collisions at a center-of-mass energy of 8 TeV. Its single-beam energy is expected to reach 6.5 TeV in 2015 operations. The LHC is located at the European Council for Nuclear Research (CERN) campus, near Geneva, Switzerland, and its beamline ring is 27 km in circumference and buried between 50 and 175 m under parts of both Switzerland and France.

Protons are initially accelerated linearly by the Linac 2, then are ramped up in energy by the Proton Synchrotron Booster, the Proton Synchrotron, and the Super Proton Synchrotron, and finally are deposited into the main LHC beam pipes. Superconducting dipole and quadrupole magnets respectively bend and focus the beams. Protons move in bunches around the ring, and each bunch is about 30 cm long; almost 3000 bunches can travel around the ring at a given time.

The two beams circulate counter to each other and are crossed at four interaction points where collisions occur. In 2012 data taking, an average of approximately 20 proton-proton interactions took place for each pair of bunches that crossed at these locations. Four primary detectors are arrayed around the ring at the interaction points. Two of these, ATLAS and the Compact Muon Solenoid (CMS), are general-purpose detectors capable of probing a wide variety of physics processes. The data presented in this thesis were collected with the ATLAS detector, which is discussed in detail below.

3.2 The ATLAS Detector

The ATLAS (A Toroidal LHC ApparatuS) detector measures properties of final state particles created by the LHC's proton-proton collisions [28]. A schematic of the detector is shown in Figure 3.1. The ATLAS coordinate system, its three major sub-detectors (the inner detector, calorimeters, and muon system), and the trigger system are described in this chapter.

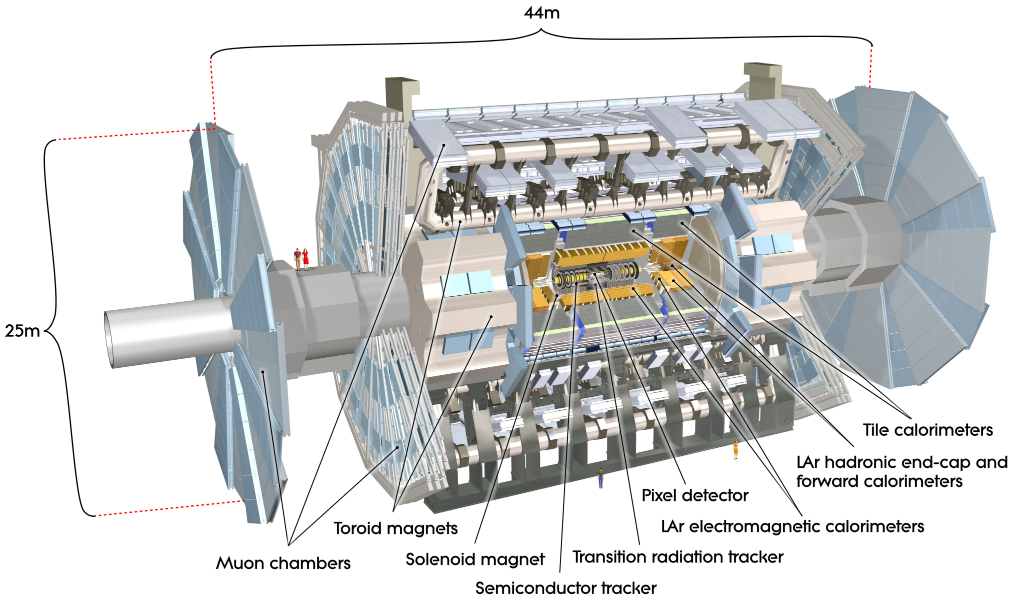

Figure 3.1: Schematic of the ATLAS detector

3.2.1 Coordinate system

ATLAS uses a right-handed coordinate system with the origin defined by the location of the nominal interaction point. The z-axis is aligned with the beam, the positive x-axis points from the interaction point to the center of the LHC ring, and the positive y-direction is defined upwards. The azimuthal angle, ϕ, is measured from the positive x-axis around the beam, with the positive y-axis at $\phi = \pi/2$; the radial distance is given by $R = \sqrt{x^2 + y^2}$. The polar angle, θ, is measured from the positive z-axis with the x-y plane at $\theta = \pi/2$. The rapidity, $\xi = \ln \sqrt{(E + p_z)/(E - p_z)}$, is a convenient angular coordinate because differences in ξ are Lorentz invariant under boosts along the beam axis. For massless particles, this reduces to the pseudorapidity, $\eta = -\ln \tan(\theta/2) = \ln \sqrt{(|\mathbf{p}| + p_z)/(|\mathbf{p}| - p_z)}$. The angular distance measure $\Delta R = \sqrt{\Delta\eta^2 + \Delta\phi^2}$ is similarly invariant.

The detector is split into three regions: one central barrel region ($|\eta| < 1.5$) and two forward ($|\eta| > 1.5$) end-cap regions. Transverse quantities, e.g. the transverse momentum p_T and transverse energy E_T, incorporate only vector components projected onto the x-y plane unless stated otherwise.

3.2.2 Inner detector

The ATLAS inner detector (ID) tracks charged particles as they leave the interaction vertex. It is made up of three subsystems: the Pixel Detector (pixels), the Semiconductor Tracker (SCT), and the Transition Radiation Tracker (TRT). Figures 3.2 and 3.3 show schematics of the inner detector barrel and end-cap regions, respectively.

The entire inner detector is surrounded by a large solenoid magnet which induces a nearly-constant 2 Tesla magnetic field in the z direction. The transverse momentum of a charged particle traversing the inner detector is directly proportional to the

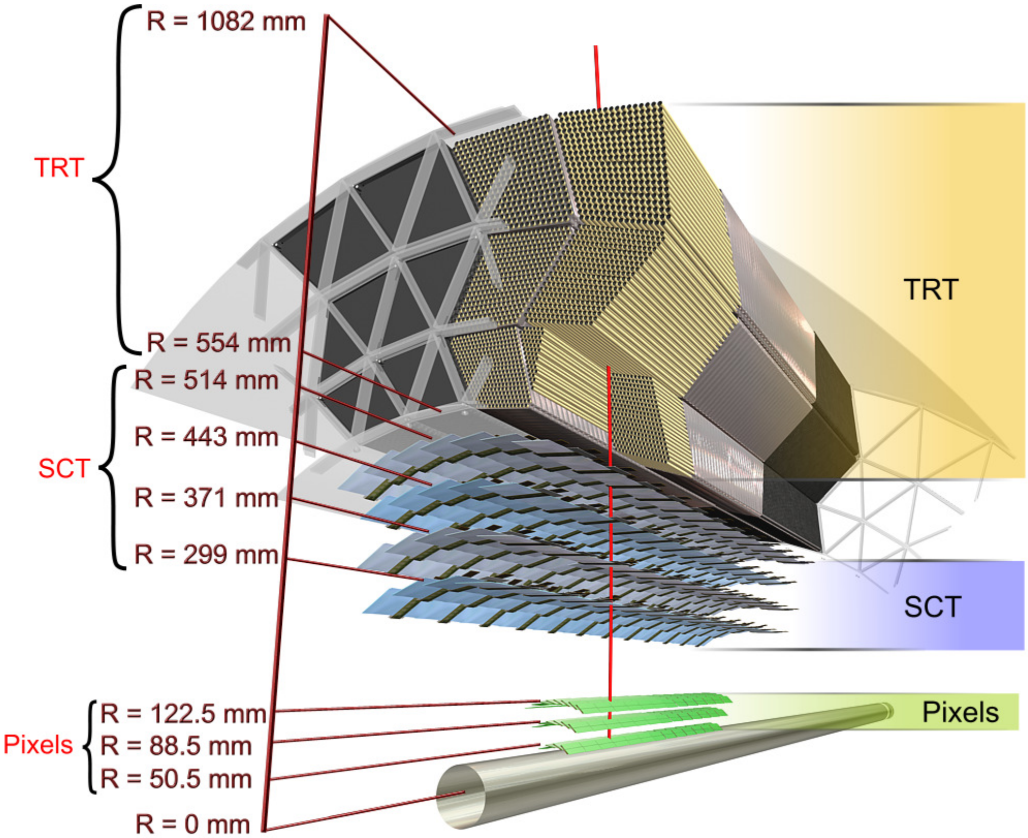

FIGURE 3.2: Schematic of the ATLAS inner detector barrel region with a central track traversing the inner detector subsystems

radius of curvature of its track.

3.2.2.1 The pixel detector and silicon tracker

The pixel subsystem is closest to the beam pipe and is composed of three layers of silicon, each pixel measuring approximately 50 μm × 400 μm in the R-ϕ and z directions, respectively. There are more than 80 million readout channels, one for each pixel. In the central region of the detector, the pixels form concentric cylinders around the beam pipe; they are arranged in disks perpendicular to the beam in the end-cap regions. Due to its granularity, very precise position measurements are possible, with an intrinsic resolution of 10 μm in the ϕ direction and 115 μm in the z (R) direction in the barrel (end-cap). The first pixel layer is about 50 mm from the

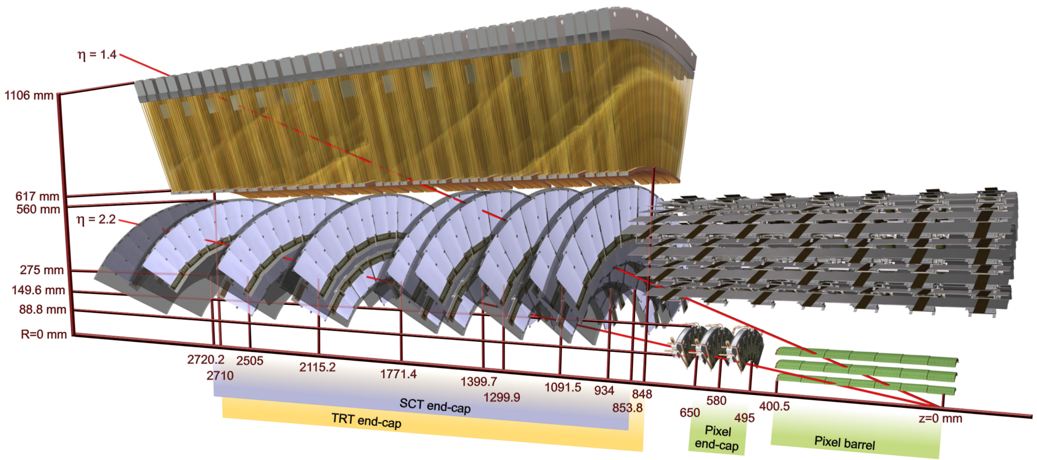

FIGURE 3.3: Schematic illustrating the ATLAS inner detector end-cap region with forward ($\eta = 1.4$ and $\eta = 2.2$) tracks traversing the inner detector subsystems

center of the beam pipe. Its proximity to the interaction point is especially useful for differentiating tracks which originate at the primary interaction from decays-in-flight.

The SCT surrounds the pixel detector and is comprised of about 6 million channels read out from strips of silicon. There are four double-layers of strips, allowing for a possible eight crossings by each track. The closest of these layers is approximately 300 mm from the beam. The intrinsic resolution of each strip detector is 17 μm in ϕ and 580 μm in z (R) in the barrel (end-cap).

3.2.2.2 Transition radiation tracker

The TRT is the largest inner detector subsystem, filling the space between 0.5 m and 1.0 m from the beam out to $|\eta| = 2.0$. It is made of long 4 mm-diameter straws filled with a mixture of Xe (70%), CO_2 (27%), and O_2 (3%) gas. The TRT is divided into four sections: two in the barrel region separated by the $z = 0$ plane and one in each end-cap. Straws are oriented parallel to the beam in the barrel and arrayed radially outward in the end-caps. Beyond this course segmentation in z, only R-ϕ information is available for each hit in the TRT; the intrinsic R-ϕ resolution per straw is 130 μm.

As a charged particle moves through a TRT straw it ionizes the enclosed gas. The resulting free electrons drift to the central anode wire, further ionizing the gas as they do so. Drifting ions induce a current on it which is subsequently read out. Thin layers of polypropylene foam fill the space between TRT straws to produce transition radiation, causing photons to be emitted as charged particles cross the boundary between materials with different indices of refraction. The amount of radiation emitted at the material interfaces grows with the γ-factor of the charged particle.

3.2.3 Calorimeters

The ATLAS detector has two calorimeter subsystems: the electromagnetic (EM) calorimeter and the hadronic calorimeters (HCAL). Their coverage reaches to $|\eta| = 4.9$, and their design is complementary to that of the inner detector for the purpose of precision electron, photon, jet, and $E_{\mathrm{T}}^{\mathrm{miss}}$ measurements. It is important that electromagnetic and hadronic showers are fully-contained by the respective calorimeter for accurate particle reconstruction and to prevent punch-through into the muon system. The calorimeters are a total of 11 interaction lengths (λ) thick at $\eta = 0$, which allows them to adequately perform in both respects.

3.2.3.1 Electromagnetic Calorimeter

The EM calorimeter is sectioned into one barrel ($|\eta| < 1.475$) and two end-cap ($1.375 < |\eta| < 3.2$) regions. It is made up of alternating absorbing (lead) and active (liquid argon) layers arranged in an accordion pattern as shown in Figure 3.5. This layout provides uniform resolution in ϕ while avoiding cracks in coverage due to electronics and other services. In total, the EM calorimeter is approximately 22 radiation lengths (X_0) thick in the barrel and more than 24 X_0 in the end-caps.

There are three active layers for $0 < |\eta| < 2.5$ (the precision measurement region)

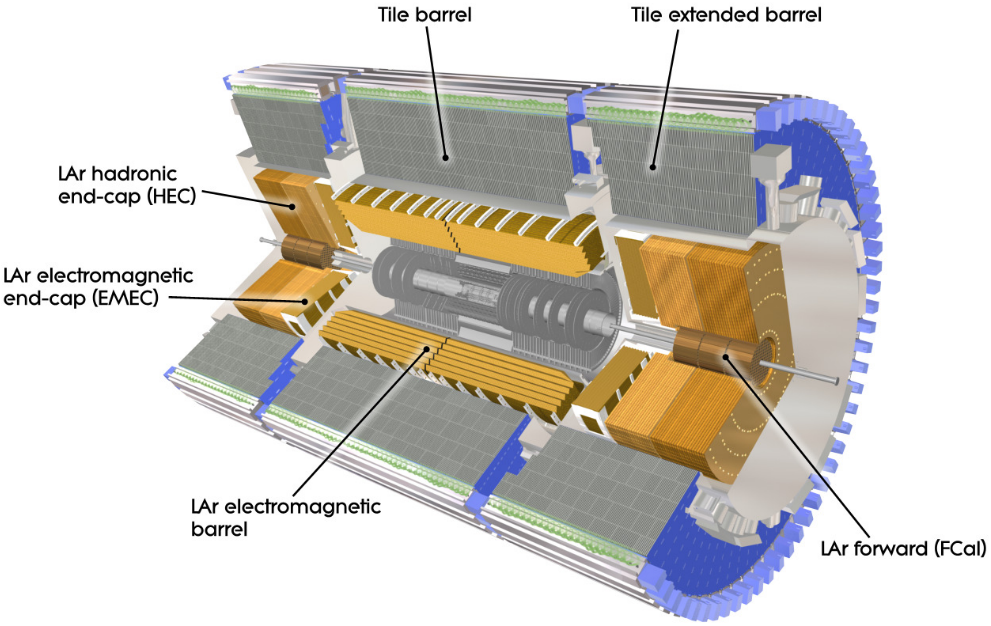

FIGURE 3.4: Schematic of the ATLAS calorimeters

and two at higher eta, $2.5 < |\eta| < 3.2$. Corrections for electron and photon energy losses in the inner detector are made using a liquid argon presampling layer out to $|\eta| = 1.8$.

In order to achieve good angular resolution, the closest layer to the inner detector is finely granulated, particularly in η ($\Delta\eta \times \Delta\phi = 0.0031 \times 0.01$ for $|\eta| < 1.40$). It is approximately 4 X_0 thick. The primary sampling layer surrounds the first layer and, at 16 X_0 thick, absorbs most of the energy from the electromagnetic shower. It is less finely segmented in η than the first, but more so in ϕ ($\Delta\eta \times \Delta\phi = 0.025 \times 0.025$ for $|\eta| < 1.40$). The third layer is more coarsely segmented ($\Delta\eta \times \Delta\phi = 0.050 \times 0.025$), but provides further containment and longitudinal shower shape information.

The design energy resolution of the EM calorimeter for electrons and photons in

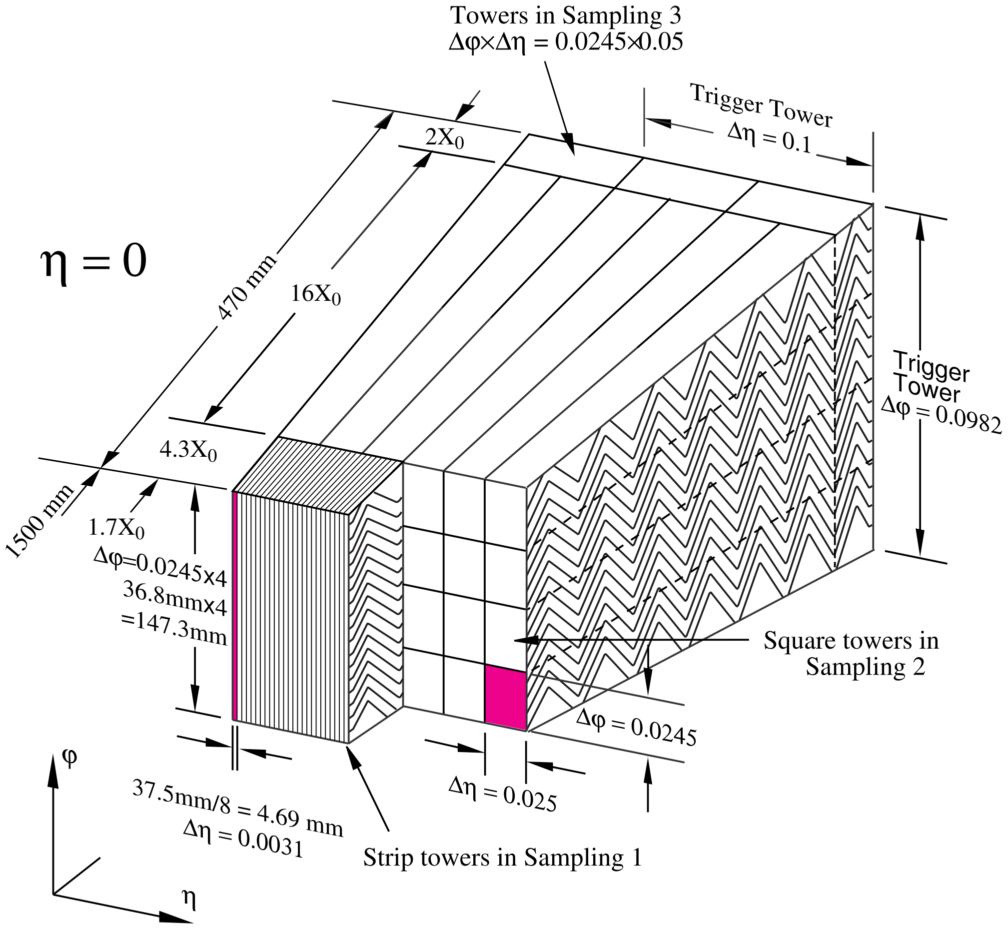

FIGURE 3.5: Schematic of the electromagnetic calorimeter accordion structure

both the barrel and end-caps is given by

$$\frac{\sigma_E}{E} = \frac{10\%}{\sqrt{E/\text{GeV}}} \oplus 0.7\%. \tag{3.1}$$

3.2.3.2 Hadronic calorimeters

There are three ATLAS hadronic calorimeters: the tile calorimeter, the hadronic end-cap calorimeter, and the forward calorimeter (FCal).

The tile calorimeter is made of steel as the absorber and scintillating tiles as the active medium. It is situated just outside the electromagnetic calorimeter from a radius of 2.28 m to 4.25 m, or 7.4λ. It has coverage out to $|\eta| = 1.7$ and is divided into a central barrel ($|\eta| < 1.0$) and two forward extended barrels ($0.8 < |\eta| < 1.7$). Each barrel contains 64 $\Delta\phi \approx 0.1$ wedges of steel and scintillator. The wedges are divided into three longitudinal layers of thickness 1.5, 4.1, and 1.8 λ (1.5, 2.6, and 3.3 λ) in the central (extended) barrel(s).

The hadronic end-cap calorimeter is a sampling calorimeter made of copper and liquid argon and covers the eta range $1.5 < |\eta| < 3.2$. It is divided into two wheels (one front and one rear) in each end-cap, each wheel consisting of two longitudinal sections, and each section segmented into 32 wedge-shaped modules. Readout cells vary in size depending on the η range: $\Delta\eta \times \Delta\phi = 0.1 \times 0.1$ for $|\eta| < 2.5$ and 0.2×0.2 otherwise.

The FCal provides coverage over the eta range $3.1 < |\eta| < 4.9$ and is segmented into three distinct layers: one with copper as the absorber and two with tungsten; liquid argon is the sampling material in each. The copper/argon layer is located closest to the interaction point and is optimized for detecting electromagnetic showers. The second and third tungsten layers primarily measure hadronic activity.

3.2.4 Muon system

The outermost sub-detector of ATLAS is the muon system, which detects and measures charged particles that leave the calorimeter systems out to an $|\eta|$ of 2.7. Precision tracking chambers and fast trigger chambers respectively fulfill its primary purposes: to accurately measure and trigger on high-momentum muons.

Muon trajectories are bent by large superconducting toroid magnets located outside the hadronic calorimeter. Central ($|\eta| < 1.4$) and forward ($1.6 < |\eta| < 2.7$) muons are chiefly deflected by barrel and end-cap toroid magnets, respectively; transition region ($1.4 < |\eta| < 1.6$) muons are deflected by fields from both sets of magnets. This geometry produces a magnetic field that is generally perpendicular to the muon tracks, which is ideal for momentum measurements.

Three layers of precision tracking chambers measure muon trajectories across the covered η range. In the barrel region, monitored drift tube (MDT) chambers filled with Ar and CO_2 gas are arranged in concentric cylinders surrounding the beam. Each chamber is composed of between three and eight layers of drift tubes with an approximate spatial resolution of 35 μm per chamber. In the end-caps, the tracking chambers are laid out in disks perpendicular to the beam. MDTs make up all three layers out to $|\eta| = 2.0$. Due to the higher particle flux in the forward region, cathode-strip chambers (CSCs), which have significantly better time resolution than MDTs, make up the first tracking layer for $|\eta| > 2.0$.

Complementary to the precision tracking chambers, fast trigger chambers provide track information within tens of nanoseconds of a particle traversal. The central ($|\eta| < 1.05$) muon trigger system employs three layers of resisitive plate chambers (RPCs) arranged in concentric cylinders, each with the possibility of recording two hits per track, while forward ($1.05 > |\eta| > 2.40$) muons pass through up to seven layers of thin gap chambers (TGCs). In addition to providing quick readout for trigger purposes, track information from RPCs and TGCs is combined with that from the precision tracking chambers to improve muon momentum measurements.

The total momentum resolution in the muon spectrometer is approximately 10% for 1 TeV muons, but accurate momentum and charge measurements are possible over a wide range of muon energies, from 3 GeV to 3 TeV.

3.2.5 Trigger systems

The purpose of the ATLAS trigger system is to quickly identify potentially interesting collision events delivered by the LHC. The trigger is broken down into three progressively stricter selection levels, Level-1 (L1), Level-2 (L2), and event filter (EF). The L2 and EF triggers are known collectively as the high-level triggers (HLT).

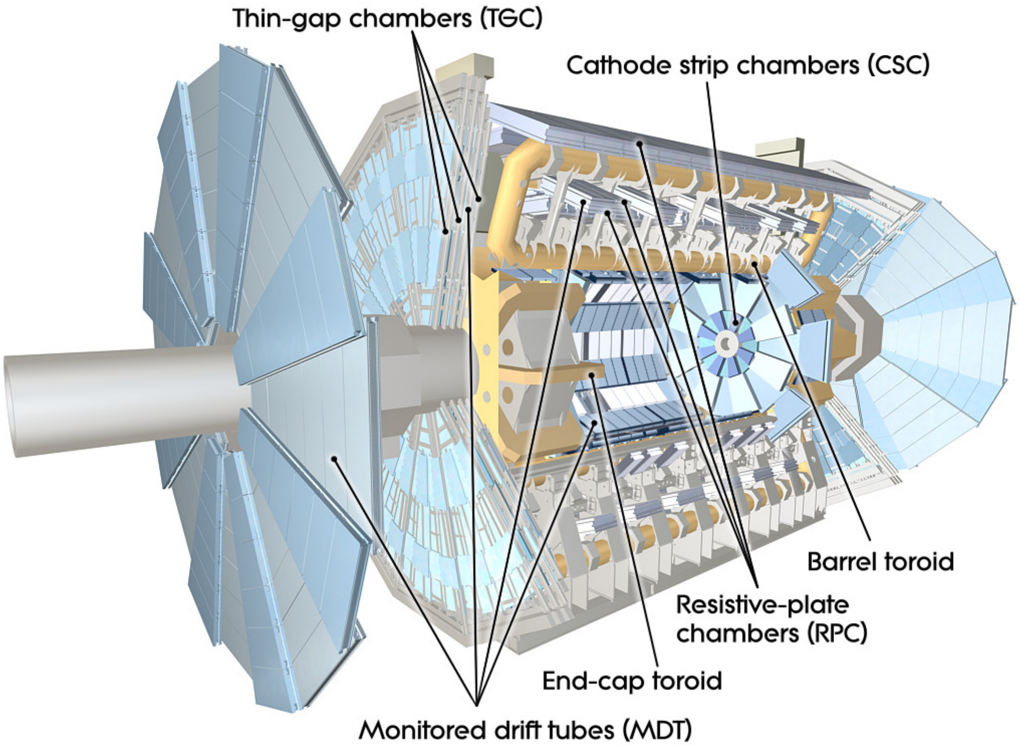

Figure 3.6: Schematic of the ATLAS muon systems

The L1 trigger identifies events with high-p_T muons, electrons, photons, jets, and τ-leptons in addition to high $E_{\mathrm{T}}^{\mathrm{miss}}$ in order to reduce the event rate from that delivered by the LHC (40 MHz) to about 75 kHz, taking less than 2.5 μs per decision. It uses a subset of the available detectors to define these objects: the muon trigger chambers and coarse-grained calorimeter information. At L1, calorimeter energy deposits are summed over towers, which incorporate all longitudinal cells in a given $\Delta\eta \times \Delta\phi = 0.1 \times 0.1$ region, but electromagnetic and hadronic towers are reported separately. Regions of interest (RoIs) in η-ϕ space around objects passing certain criteria (e.g. an energy threshold) are also designated by the L1 trigger and passed to the HLT.

The high-level triggers filter events based on all detector data, including tracking information, contained in the RoIs defined by the L1 trigger. Since the HLT operates at a lower event rate, particle, jet, and $E_{\mathrm{T}}^{\mathrm{miss}}$ definitions are refined using the additional detector information available, and tighter requirements (e.g. higher thresholds) are imposed on the objects in question. For example, complete calorimeter granularity is available at HLT, so jet and $E_{\mathrm{T}}^{\mathrm{miss}}$ definitions are improved from L1. A basic tracking algorithm is run on inner detector hit data at L2, while at EF it is feasible to leverage the full offline tracking machinery outlined in Section 5.1. Combined, the L2 and EF triggers reduce the event rate from 75 kHz to approximately 200 Hz, and about 1 MB per selected event is stored to disk.

4

Simulation of Proton Collisions

In order to accurately test models and measure physical observables, a method for predicting the outcome of proton collisions in the detector is needed. At ATLAS, a comprehensive framework that simulates events from the initial proton collision through detector readout was developed for this purpose [29]. Monte Carlo (MC) techniques are used to simulate a wide range of physical processes: from the kinematics of the interaction at the primary vertex to the detector element response during a particle traversal and the resulting readout of the associated electronics.

The simulation process is divided into three stages: event generation and immediate decays, particle interactions with detector elements, and digitization of the energy deposited in active regions of the detector. The output of the simulation is equivalent to that read out during data taking, so both collision data and theory predictions are processed by identical trigger and offline reconstruction algorithms.

4.1 Event generation

The event generation phase is comprised of the initial proton-proton interaction and prompt particle decays, parton showering, and hadronization; the resulting stable particles are passed to the detector simulation framework. Any particle with $c\tau >$ 10 mm is considered stable by the shower and hadronization generators and will be passed to the detector simulation. Those with $c\tau <$ 10 mm are decayed beforehand and their interactions with material and the magnetic field are ignored.

A variety of Monte Carlo based generators exist, but they are grouped into three broad categories here: event generators, parton shower generators, and specialized generators. Event generators simulate the hard scatter of a collision and produce an output of particles which are not required to be stable. Parton showering generators approximate the progression of the QCD shower in the event. Specialized generators target specific classes of decays or radiation to improve the predictions of event and parton showering generators.

4.1.1 Event generators

Event generators calculate the contribution of diagrams to a physics process to some fixed order in α_S. Common event generators used in ATLAS analyses include ALPGEN [30], MC@NLO [31], POWHEG [32], and MADGRAPH [33].

ALPGEN specializes in final states with a given number of well-separated jets by calculating the fixed-order QCD matrix element. It is a so-called leading order (LO) generator, meaning that it can only calculate tree-level diagrams up to a certain order in α_S. This is still useful for topologies with a high number of well-separated energetic jets since the matrix element is expected to yield better results than the shower approximation implemented in PYTHIA [34] or HERWIG [35], discussed in Section 4.1.2. However, the time required to compute the matrix element for a process scales with the factorial of the outgoing particle multiplicity, which becomes untenable for very high numbers of particles.

MADGRAPH similarly generates events by determining the set of Feynman diagrams that result in a given final state and calculating the matrix element for each.

It is particularly convenient for generating an inclusive sample of events based on the desired final state signature. For instance, by requesting processes that result in a lepton, neutrino, and at least two additional jets, one will obtain from MadGraph a representative mixture of $t\bar{t}$, W+jets, and diboson events, as well as any additional processes with that final state signature. Until the recent release of MadGraph aMC@NLO, MadGraph was also a tree-level generator and was only used as such in the analyses discussed in this thesis.

Limiting calculations to tree-level diagrams results in inadequate predictions for certain physics processes. Next-to-leading order (NLO) generators address this issue by including the contributions of loop diagrams and diagrams out to an order of $n+1$ for a process at order n in α_S. This improves the accuracy of the calculation and reduces the dependence on factorization and renormalization scales, but divergences can arise in the momentum integration of loops. These must be dealt with by the generator through cancellation with other divergences at the same order of α_S in order to yield useful results.

MC@NLO is widely used in ATLAS for the generation of W, Z, single top, and $t\bar{t}$ events. It includes one loop corrections to the LO calculation, which, for instance, leads to a more accurate top quark p_T spectrum than those of LO generators. Powheg is also often used for a number of processes, including $t\bar{t}$ production, as an alternative to MC@NLO.

4.1.2 Parton showering

Parton shower generators approximate the progression of QCD interactions to all orders in α_S in addition to the fixed order calculations of event generators. Pythia and Herwig are both commonly used shower generators at ATLAS. To approximate the QCD shower, hard partons are allowed to radiate softer partons down to some minimum energy scale. Emission is governed by the Sudakov form factor, which describes the probability that no particles are radiated above a certain energy threshold [36]. Below this threshold non-perturbative effects become important. This process is successively applied again to the incoming partons and to the emitted partons until no further energetic radiation is produced above the threshold.

Since parton shower generators describe the evolution of a shower to all orders of α_S, it is important to ensure that the shower generator avoid double counting the calculations included by the event generator. For example, a hard gluon emitted in the shower evolution is equivalent to gluon final state radiation produced by the fixed order generator. In order to avoid this calculation overlap, matching schemes have been developed to make event and parton shower generators compatible.

It is important that for a given process the calculations are performed to an appropriate order of α_S by the fixed order and parton shower generators. Fixed order generators do an excellent job of describing final state partons that are energetic and well-separated, while parton shower generators excel at collinear and soft interactions.

4.1.3 Hadronization and specialized generators

The transition from final state partons at the end of parton showering to the stable hadrons which interact with the detector is not determined by an exact theory. However, phenomenological models have been somewhat successful at describing this conversion. The Lund string model [37] and various extensions to it are implemented in PYTHIA. HERWIG uses the cluster model [38] for its hadronization step.

The decay of τ leptons and final state photon emission are simulated by dedicated generators, TAUOLA and PHOTOS respectively, during the hadronization stage. Parton shower generators are directed to consider τ leptons as stable and not to simulate electromagnetic radiation to avoid double counting, and their output is subsequently passed through TAUOLA and PHOTOS.

4.2 Detector simulation

The GEANT4 (GEometry ANd Tracking) [39, 40] toolkit is used to simulate energy deposits in the detector from particles produced in event generation. A complete description of the detector, including active detector elements, electronics, and support structure, was built using the GeoModel library [41]. This is comprised of more than 300,000 individual physical volumes which are loaded into GEANT. The ATLAS geometry is updated on a regular basis as misalignment and dead channel information is revised. Various geometries and detector conditions for individual runs are stored in a large database and are used to assess the effect of changes to the detector geometry on physical measurements. A detector layout which is purposefully distorted is also available to estimate the impact of subdetector distortions on jet and $E_{\mathrm{T}}^{\mathrm{miss}}$ reconstruction. The primary vertex position is smeared according to the size and shape of the luminous region of the beam in ATLAS before particles traverse the detector.

Particles produced during event generation are propagated through the detector using GEANT4 libraries. Interactions with the detector and decays-in-flight are simulated for particles with $|\eta| < 6.0$; particles with $|\eta| > 6.0$ are not simulated to save computing time and disk space. As a particle traverses the detector, energy deposit information is stored in a "hit" file. This file contains all input necessary for the digitization stage as well as information about the original particles from event generation, including their flavors and four-momenta.

Fast simulation, which uses parameterized detector responses for the slowest parts of the full GEANT simulation, is also available. This greatly reduces the computation time required to propagate particles at the cost of slightly less accurate event simulation. For example, the time required to simulate $t\bar{t}$ events using ATLFAST-II, the most commonly used fast simulation framework, is a factor of 20 smaller than that used by the full GEANT simulation.

4.3 Digitization

The digitization stage converts energy deposits from the hit file into "digits." When the current or voltage in a readout channel surpasses the required threshold, a digit is created. Digits can take several forms, for instance the time over threshold or the shape of the readout signal.

Each subdetector has its own digitization software that digitizes its hit information, taking into account particulars like electronic noise, and the digitization algorithms used are tuned to reproduce performance observed during commissioning. Run-specific information, such as noise rates and dead channels, is read from a database and reproduced in the simulation. In order to simulate the effect of pile-up, hit files from simulated minimum bias, cavern background, and beam halo events are overlaid.

5

Event and Particle Reconstruction

The data from each collision is organized into a set of reconstructed physics objects corresponding to observable particles and collections of particles. Electrons, muons, jets, and missing transverse energy are all examples of objects which are reconstructed in each event. A variety of algorithms are used to assemble them out of their respective detector signals—tracking hits, calorimeter deposits, etc.

Since data from real collisions and simulation contain equivalent information and are stored in the same format, both are analyzed using identical reconstruction algorithms. However, the reconstruction and identification of physics objects is not guaranteed to be perfectly modeled by simulation. Where possible, corrections are derived to take into account observed discrepancies between the data and the MC simulation. If this is not possible, then an appropriate uncertainty on the simulation must be taken into account when comparing it to data.

5.1 Inner detector tracks

Inner detector tracks are crucial for electron and muon reconstruction, as well as for determining the coordinates of the primary interaction and which objects originated from it. The ATLAS tracking algorithm [42] is composed of two consecutive sequences: inside-out reconstruction and outside-in tracking.

5.1.1 Inside-out sequence

The inside-out sequence begins with a collection of hits registered in the pixels and SCT. Track candidates, each a set of inner detector hits compatible with a single particle trajectory, are seeded using only these hits from the silicon detectors. Once seeded, detector elements that are likely to contain additional hits consistent with this track are assembled into a so-called "road." Additional hits along the road are subsequently added to the track, with the track parameters updated as each hit is incorporated.

After all seeded tracks have been extended through the inner detector, ambiguities must be resolved. Each track is ranked by a scoring system that takes into account the fit quality and favors longer tracks over shorter segments. Tracks with more precise hit measurements (e.g. from the central pixels) are given relatively higher scores than those with coarser hits. Hits that are associated with more than one track are given to whichever has a higher score, and the score of each affected track is subsequently updated.

Once all hits have been assigned to only one track candidate, tracks which fall below a quality threshold are discarded. TRT hits are added to those that remain, but the original silicon track is used for associating TRT hits; its parameters are not updated as TRT hits are incorporated. After track extension into the TRT is complete, the track parameters are re-fit using all associated hits.

5.1.2 Outside-in sequence

The outside-in tracking sequence aims to reconstruct tracks that were not seeded by the inside-out sequence. This can occur for a number of reasons. Hadron decays-in-flight which take place outside of the pixels are unlikely to be seeded. Similarly, electrons from photon conversions may not leave any hits in the silicon detectors and will not be seeded. In such cases, seeding tracks from the TRT is the most viable strategy.

TRT tracks are extended inwards towards the primary interaction vertex, and silicon hits along the associated track roads are added, again in sequence. Since the TRT hits only contain $R\phi$ ($z\phi$) information in the barrel (end-caps), the track finding is less efficient, especially for low-p_T tracks.

5.1.3 Reconstruction of primary vertices

An iterative vertex finding algorithm is used to identify primary vertices [43]. The z-position at the beamline of each reconstructed track in an event is used as a vertex seed. Each track is tested against each seeded vertex using a χ^2 fit; if the track is more than 7σ discrepant with a vertex, then it is used to seed a new vertex. This procedure is applied iteratively until all tracks are associated to a vertex. A minimum of two tracks are necessary to define a vertex, but collisions involving interesting physical processes generally produce more. The vertex with the highest scalar p_T sum of its constituent tracks is called the "hard scatter" vertex, and any physics objects with tracks are generally required to originate from it.

Figure 5.1 illustrates the spatial distribution of primary vertices reconstructed in minimum bias data. Figure 5.2 shows the average number of reconstructed primary vertices as a function of the average number of interactions per bunch crossing, $\langle\mu\rangle$.

5.2 Calorimeter clusters

Similar to how tracks are essentially organized collections of inner detector hits, calorimeter clusters are constructed from energy deposits in cells in the electromagnetic and hadronic calorimeters [45]. A single particle interacting with the ATLAS

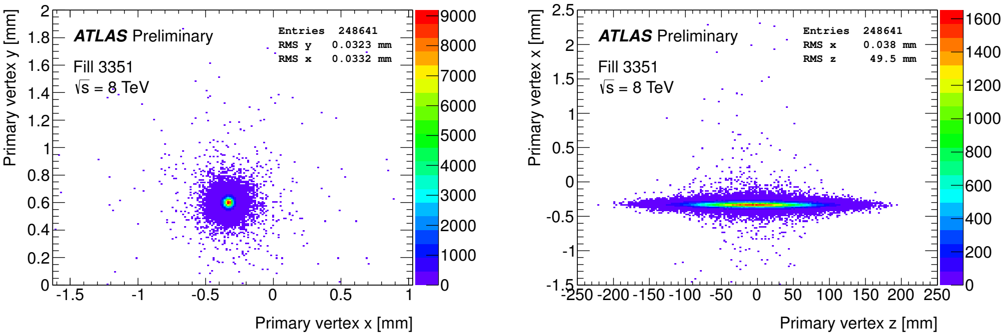

FIGURE 5.1: The spatial distribution of primary vertices with at least five associated tracks in minimum bias data in a particular run [44].

calorimetry systems generally deposits energy into more than one cell in both the longitudinal and lateral directions, so algorithms have been devised to collect them into clusters for the purposes of calibration and particle identification.

Two classes of clustering algorithms are used in ATLAS: sliding-window and topological.

5.2.1 *Sliding-window clustering*

The sliding-window clustering algorithm is used in electron reconstruction and is composed of three phases: tower building, seed finding, and cluster filling.

The calorimeter is first split into $N_\eta \times N_\phi = 200 \times 256$ "towers" of equal size in $\eta - \phi$ space: $\Delta\eta \times \Delta\phi = 0.025 \times 0.025$. Each tower's energy deposits are summed longitudinally to determine its total energy. These tower edges do not correspond to calorimeter cell boundaries, so the energy of a cell overlapping more than one tower is split proportionally by the fraction of the cell's area covered by each tower.

To seed the clusters, a window of size $N_\eta^{window} \times N_\phi^{window} = 5 \times 5$ (in units of towers) is moved over the towers built in the tower building phase. If the sum of the transverse energy in the towers of the window exceeds 3 GeV, it is considered a cluster seed. The location of the cluster seed in $\eta - \phi$ space is determined by the energy-

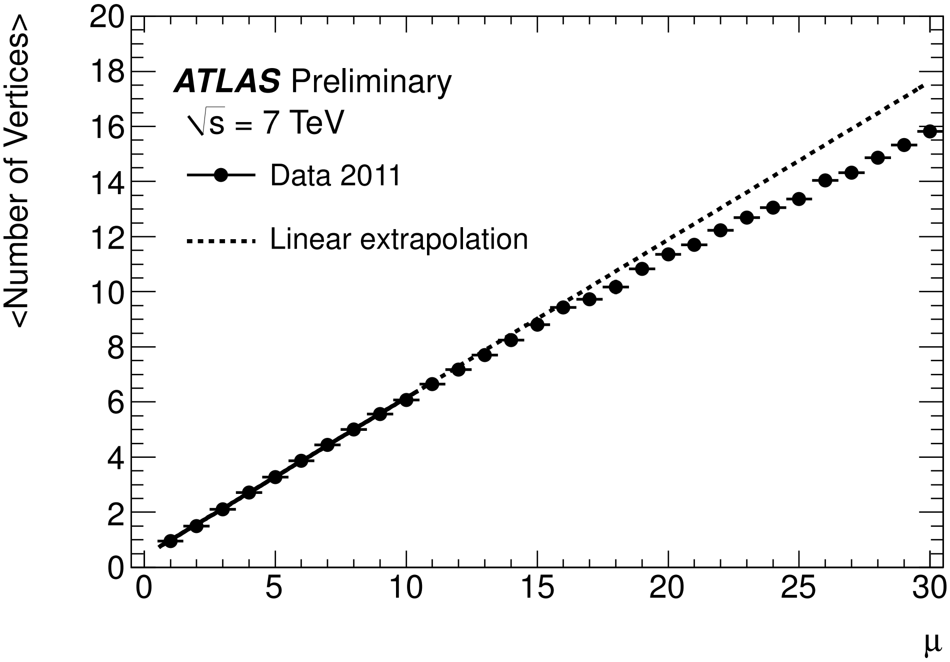

FIGURE 5.2: The average number of reconstructed primary vertices with at least three associated tracks as a function of the average number of interactions per bunch crossing, μ, in minimum bias data with the full 2011 ATLAS dataset.

weighted center of all cells within a smaller window of size $N_\eta^{pos} \times N_\phi^{pos} = 3 \times 3$. The smaller window size makes this calculation less susceptible to noise. If seed clusters are reconstructed within two towers of each other in either the η or ϕ directions, the one with the lesser E_T is discarded.

During cluster filling, the seeded clusters are constructed again using a 3×7 (5×5) tower window in the barrel (end-cap). The final cluster energy is then calculated based on the summed energy of the constituent towers, the estimated energy which does not fall within the final cluster window, and the estimated energy deposited in the inner detector. In MC simulations, an electron with $E_T \approx 15$ GeV has a cluster reconstruction efficiency above 99%, and the efficiency rises with E_T.

5.2.2 Topological clustering

Topological clusters (topoclusters) are formed by grouping neighboring cells with large energies compared to the expect noise threshold. Unlike sliding-window clusters, topological cluster may include a variable number of cells.

First, a list of seeds is built out of all cells with a signal-to-expected-noise (S/N) ratio above some threshold, t_{seed}. The expected noise is determined by the quadrature sum of the expected electronic noise and the expected average contribution from pile-up. The seeds are then ordered by their S/N, highest first, and any neighboring cell with a S/N above $t_{neighbor}$ which is not also a seed is added to the original to form a proto-cluster, and the procedure continues. If a neighbor cell with S/N above $t_{neighbor}$ is adjacent to more than one proto-cluster, the proto-clusters are merged.

Once all valid neighbor cells have been incorporated into proto-clusters, a cut of $E_T > E_T^{thresh}$ is applied to form the list of final proto-clusters. The same procedure is then repeated, but the seed cells are defined as those with $E > 500$ MeV, and only cells constituent in proto-clusters from the first round of clustering are included. The proto-clusters which are formed from this second iteration are the topological clusters. The second round of clustering helps to prevent clusters which could incorporate very large portions of the calorimeter systems.

In the EM calorimeter, $t_{seed} = 6$, $t_{neighbor} = 3$, and $E_T^{thresh} = 5$ GeV. In the hadronic calorimeter they are 4, 2, and 0 GeV, respectively.

5.3 Electrons

The loosest definition of an electron in the ATLAS detector is a sliding-window EM cluster with at least one inner detector track matched to it [46]. Electrons are reconstructed in the precision measurement region of the electromagnetic calorimeter, $|\eta| < 2.47$.

5.3.1 Electron track matching

In order to match an electron, a region of interest (ROI) with a cone size of $\Delta R = 0.3$ is defined around each EM cluster which passes a set of loose shower-shape cuts. If a track seed with $p_T > 1$ GeV and at least three silicon hits but which fails to accrue seven inner detector hits during track reconstruction falls within this ROI, it is constructed again using an altered tracking algorithm that allows for up to 30% energy loss through bremsstrahlung at each track-material interface. Any successfully rebuilt track is added to the list of viable tracks for matching purposes.

In order to be considered loosely matched to an EM cluster, tracks must fulfill one of two sets of criteria:

- (a) If the track has at least four silicon hits, it is extrapolated to the middle layer of the EM calorimeter. It must be within $\Delta\phi < 0.2$ of the EM cluster on the side that the track is bending toward or within 0.05 on the opposite side; it must also be within $\Delta\eta < 0.05$. The outermost hit of tracks with fewer than four silicon hits must satisfy the $\Delta\phi$ requirement, but not the $\Delta\eta$ one due to the lack of η information in the TRT.

- (b) After rescaling the track momentum to the measured cluster energy, the track is within $\Delta\phi < 0.1$ of the EM cluster on the side it is bending toward or within 0.05 on the opposite side; it must also be within $\Delta\eta < 0.05$.

The second criterion is designed to recover low-p_T tracks that undergo significant energy loss due to bremsstrahlung before reaching the EM calorimeter.

Once a track is matched to an EM cluster, the constituent hits are fed into a specialized Gaussian Sum Filter (GSF) [47], which recomputes the track parameters by taking into account bremsstrahlung effects. TRT-only tracks, which are not reparameterized, and the less than 0.01% of tracks that fail the GSF fit maintain their original track parameters. If more than one track is matched to an EM cluster, the best-match track is chosen using a score based on the ΔR distance between the cluster and track and the number of pixel hits in the track, with smaller distances and more pixel hits preferred.

5.3.2 Electron identification

Although an electron identification menu based on multivariate likelihood techniques has recently been developed at ATLAS, the analyses discussed in this thesis use a cut-based electron identification selection. After successfully matching a track to a cluster, several identification working points are defined in the cut-based menu with varying levels of background rejection and electron efficiency. The primary backgrounds to prompt electrons in ATLAS are hadronic jets, electrons from photon conversions, Dalitz decays, and semileptonic heavy flavor decays. The `loose++`, `medium++`, and `tight++` working points, listed here in increasing electron purity, are the most commonly used.

The `loose++` cuts include requirements on the fraction of the EM cluster E_T which leaks into the hadronic calorimeter, the shape of the electromagnetic shower, track quality requirements, and the $\Delta\eta$ distance between the track and the EM cluster. `medium++` electrons are a subset of the electrons which pass the `loose++` requirements, with tighter cuts on the number of hits in the silicon trackers and shower shape variables. `tight++` electrons are similarly a subset of `medium++` electrons with additional rejection of photon conversions, a maximum $\Delta\phi$ distance between the track and EM cluster, and an E/p requirement. In general these cuts are p_T and η dependent to provide consistent electron efficiency and background rejection power throughout the detector. The `medium++` and `tight++` definitions are designed to respectively reject 5,000 and 50,000 light jets for every one accepted.

Figure 5.3 shows the electron identification efficiency for several working points as a function of the electron η and p_T.

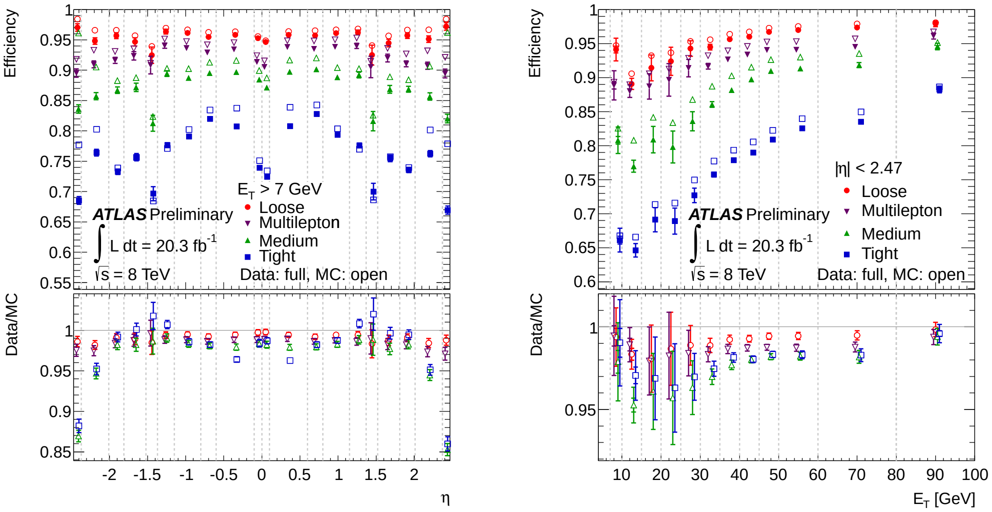

FIGURE 5.3: Identification efficiencies of various electron definitions for electrons from $Z \to ee$ decays in $\sqrt{s} = 8$ TeV data and MC as a function of the electron η (left) and E_T (right). "Loose," "Medium," and "Tight" definitions correspond to `loose++`, `medium++`, and `tight++`, respectively. The bottom panel of each figure shows the ratio of the efficiency measured in data and that measured in MC.

Additional cuts, known as isolation cuts, are often imposed on electrons after identification requirements. Isolation cuts remove electrons with significant nearby hadronic activity. This improves the purity of the selected electron candidates by rejecting those from light jets and heavy flavor decays. Electron isolation will be discussed in detail in Chapter 7.

5.3.3 Electron corrections

In order to take into account any discrepancies in electron reconstruction between the simulation and data, two corrections are applied to electrons. First, any difference in the actual and simulated reconstruction and identification efficiencies is corrected for by applying a weight to simulation events called a “scale factor.” The derivation of these weights will also be discussed in detail in Chapter 7. Second, $Z \rightarrow ee$ events are selected in Monte Carlo and data, and any difference in the position and width of the Z boson peak is corrected in data to match that in MC.

5.4 Muons

Muons at ATLAS are reconstructed using information from the muon spectrometer (MS) and inner detector (ID) with reconstruction coverage for muons with $|\eta| < 2.7$. There are several muon identification schemes available. Three are used in this thesis: stand-alone (SA), combined (CB), and segmented-tagged (ST) [48].

Stand-alone muons are reconstructed solely from MS hit information. Track segments are constructed in the precision chambers of the MS and confirmed, where possible, by the trigger chambers. Track segments which are consistent with the path of a muon moving through the toroid magnetic field are linked into a combined MS track. Segments which traverse precision chambers but leave no hit are strongly disfavored in the combination since the active regions of the drift tubes are nearly 100% efficient. MS tracks are extrapolated back to the interaction point, taking into account energy losses in the calorimeters, to obtain the original muon four-momentum.

Combined muons are seeded by stand-alone muon tracks, but are combined with independently reconstructed inner detector tracks. During back extrapolation and combination, ID tracks with higher numbers of hits and lower χ^2 are preferred. The hits of the combined ID-MS track are re-fit using the full information of both subdetectors to determine the four-momentum of the CB muon.

Segment-tagged muons are seeded by inner detector tracks. MS track segments are each tested for compatibility with nearby ID tracks. In the case of a successful match, the combined ID + track segment hits are re-fit to form the combined ST muon track and four-momentum.

Analyses may use any of these three algorithms to identify muons, but overlapping muons reconstructed using different algorithms are removed, with combined muons taking priority over ST muons. Muons with $|\eta| > 2.5$ have no ID tracks, so the SA muon reconstruction algorithm is used only in this region of the detector. Additional background rejection is achieved by imposing requirements on the number of silicon and TRT hits on CB and ST muon tracks and the number of matched track segments reconstructed in the MS. Muon isolation will be discussed in Chapter 6.

Figure 5.4 shows the muon reconstruction efficiency as a function of the muon η and p_T.

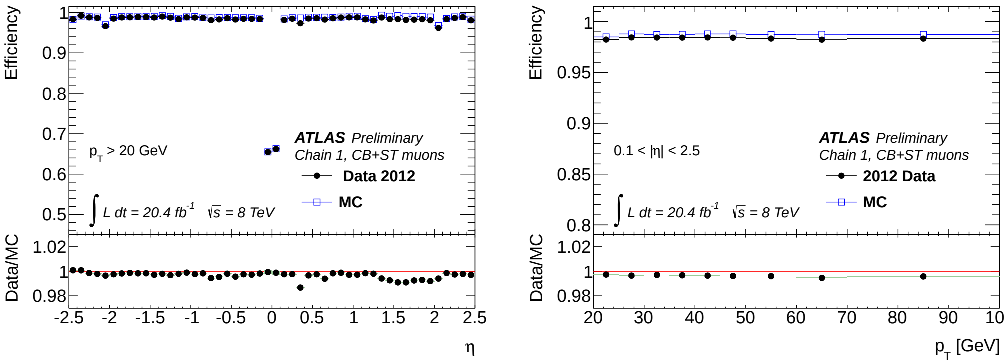

FIGURE 5.4: Reconstruction efficiencies for CB+ST muons from $Z \to \mu\mu$ decays in $\sqrt{s} = 8$ TeV data and MC as a function of muon η (left) and p_T (right). The bottom panel of each figure shows the ratio of the efficiency measured in data and that measured in MC.

Muons, like electrons, have corrections applied in the simulation to account for any mismodeling. $Z \to \mu\mu$ events are selected in data and simulation, and any difference in the position and width of the Z boson mass peak is corrected for in the simulation. Scale factors are derived to account for any discrepancy in the muon reconstruction efficiency.

5.5 Jets

Jets in the ATLAS detector represent a collection of nearby high-p_T particles. Groups of neighboring particles often originate from the resulting parton shower of a high-p_T quark or gluon, and in many analyses the jet four-momenta in an event are used as proxies for the four-momenta of the original partons. Only jets reconstructed from calorimeter clusters are discussed here, although they can be built from any set of four-momenta in an event, e.g. tracks.

5.5.1 Jet calibration and clustering

Topological clusters, introduced in Section 5.2.2, are used as inputs to jet clustering algorithms. Before jet building, clusters are calibrated using the local cluster weighting (LCW) calibration scheme [49]. Individual clusters are calibrated using the energy density of the constituent cells, the fraction of energy deposited in each calorimeter layer, the cluster isolation, and its depth in the calorimeter. The calibration weights are derived from MC simulations of charged and neutral pions based on the detector responses they induce.

Once all clusters in the event have been calibrated, they are grouped into jets using the anti-k_t algorithm [50]. In this document, a “jet” or “small-R” jet refers to an anti-k_t jet clustered with an R parameter of 0.4; “fat” or “large-R” jets are clustered with an R parameter of 1.0. A further calibration, derived from the response of jets built from final state truth electrons, photons, and hadrons, is applied to jets after clustering has finished. This is called the jet energy scale (JES) calibration.

5.5.2 Jet quality requirements

There are several sources of backgrounds to jets produced in ATLAS: interactions between the beam and the gas within the beam pipe, beam interactions with other structures external to ATLAS, cosmic ray muons, and calorimeter noise [51]. Suppression of these backgrounds is achieved through timing cuts and assessing both the fraction of the jet energy deposited in the EM calorimeter (f_{EM}) and the ratio of the p_T sum of associated charged tracks to the p_T of the jet ($p_T^{charged}/p_T^{jet}$). The efficiency of these quality requirements, measured in collision data, is approximately 99%.

5.5.3 Jet vertex fraction

The jet vertex fraction (JVF) of a jet estimates how much transverse momentum from a jet originates at the hard scatter vertex, which is defined as the primary vertex with the highest scalar p_T sum and at least five tracks. It is used to suppress the background of jets originating from pile-up vertices. In order to calculate the JVF of a jet, tracks are associated to it through a procedure known as ghost association [52].

In this technique, tracks are treated as extremely low-energy, e.g. 1 eV, clusters in the calorimeter and fed into the jet algorithm. This does not effect the event jet reconstruction because the track-clusters are so soft. After running the jet algorithm, the tracks will have each been clustered into a calorimeter jet. The track constituents of the calorimeter jets are their associated tracks.

The JVF of a jet measures the fractional p_T of its tracks which originate at the hard scatter vertex. It is defined as the scalar p_T sum of all associated tracks originating at the hard scatter vertex divided by the scalar p_T sum of all associated tracks,

$$\mathrm{JVF} = \Big(\sum_{\mathrm{HS\ tracks}} p_T^{\mathrm{track}} \Big) \Big/ \Big(\sum_{\mathrm{tracks}} p_T^{\mathrm{track}} \Big), \tag{5.1}$$

where the sums are over associated tracks, and HS tracks are those from the hard scatter vertex. The JVF of each jet is between 0 and 1 unless there are no tracks associated with a jet; in that case, the JVF is set to -1.

5.5.4 Jet grooming

Large-R jets undergo "trimming" [53] before any selection is imposed. Similar to the jet vertex fraction for small-R jets, trimming greatly reduces the contribution of particles originating from pile-up vertices. Since fat jets cover a larger area in the calorimeter than small-R jets, they are especially susceptible to this type of contamination.

The trimming procedure leverages the fact that particles from pile-up vertices are often softer than those from the hard scatter vertex. First, the jet constituents are reclustered using the k_t algorithm [54] with an R parameter R_{sub}. Any k_t subjet i with a p_T fraction $p_T^i/p_T^{jet} < f_{\text{cut}}$ is removed, where f_{cut} is a predetermined constant of the algorithm. Figure 5.5 illustrates this procedure in a schematic, and Figure 5.6 shows the effect of trimming on the leading jet mass in boosted hadronic top candidates. The default trimming parameters used at ATLAS and in the analysis presented in Chapter 6 are $f_{\text{cut}} = 0.05$ and $R_{\text{sub}} = 0.3$.

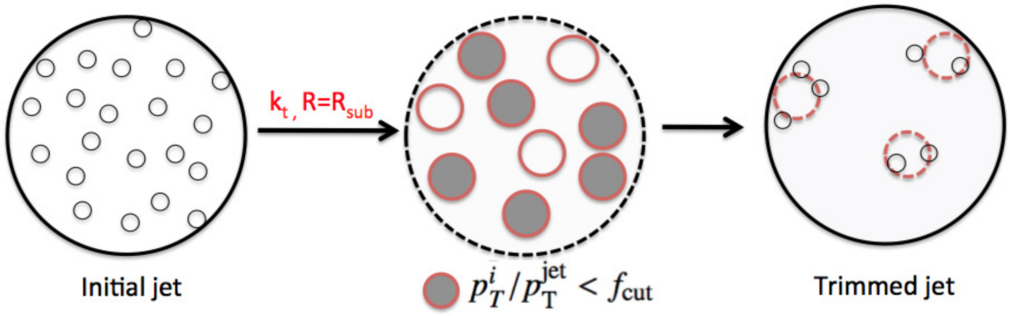

FIGURE 5.5: A schematic of the trimming procedure applied to large-R jets at ATLAS, showing the removal of soft clusters originating from primary vertices other than the hard scatter vertex [55].

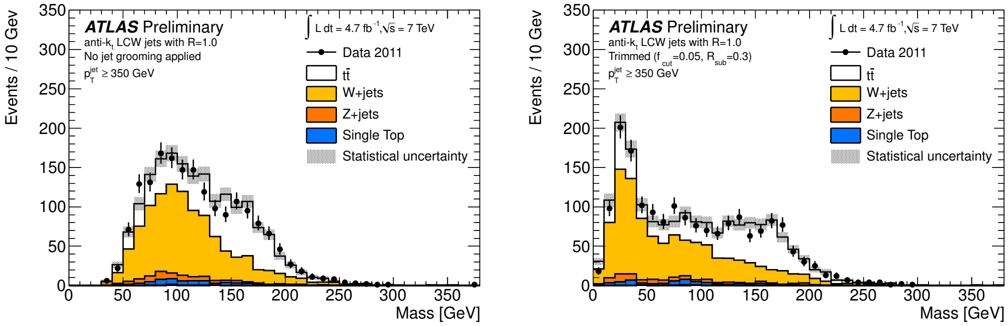

FIGURE 5.6: The large-R jet mass of hadronic top jet candidates before (left) and after (right) the trimming procedure has been applied. Note the emergence of a peak at the top quark mass after trimming [55].

5.6 Missing transverse energy

The momentum transverse to the beam line of a parton participating in the hard scatter of an LHC collision is negligible compared to the momentum transfer of the interaction. As a result, the total transverse momentum of the system is also very small. The missing transverse energy ($E_{\mathrm{T}}^{\mathrm{miss}}$) is defined as the negative vector sum of all particle momenta in the plane transverse to the beam [56] and is used to estimate the total transverse momentum of all particles produced in the collision that interact weakly with the ATLAS detector, e.g. neutrinos.

It consists of two components: the calorimeter and muon terms. The muon term is determined by the total transverse momentum of all muons in the event. The calorimeter term is calculated from all energy deposited by jets, photons, electrons, and τ leptons. Each of these objects, if appropriately identified, is calibrated to its final energy scale to improve the $E_{\mathrm{T}}^{\mathrm{miss}}$ resolution. An additional soft calorimeter term adds any topological clusters, LCW calibrated, that are not associated with an object already included in the calculation. Calorimeter clusters which are not associated to a jet but are within $\Delta R < 0.3$ of a muon are not included in the $E_{\mathrm{T}}^{\mathrm{miss}}$ calculation.

The resulting terms, $E^{miss}_{x(y),muon}$ and $E^{miss}_{x(y),calo}$ are added component-wise:

$$E^{miss}_{x(y)} = E^{miss}_{x(y),muon} + E^{miss}_{x(y),calo} \tag{5.2}$$

Figure 5.7 shows the $E_{\mathrm{T}}^{\mathrm{miss}}$ distribution of $\mu\mu$ events in data and MC at $\sqrt{s} = 8$ TeV.

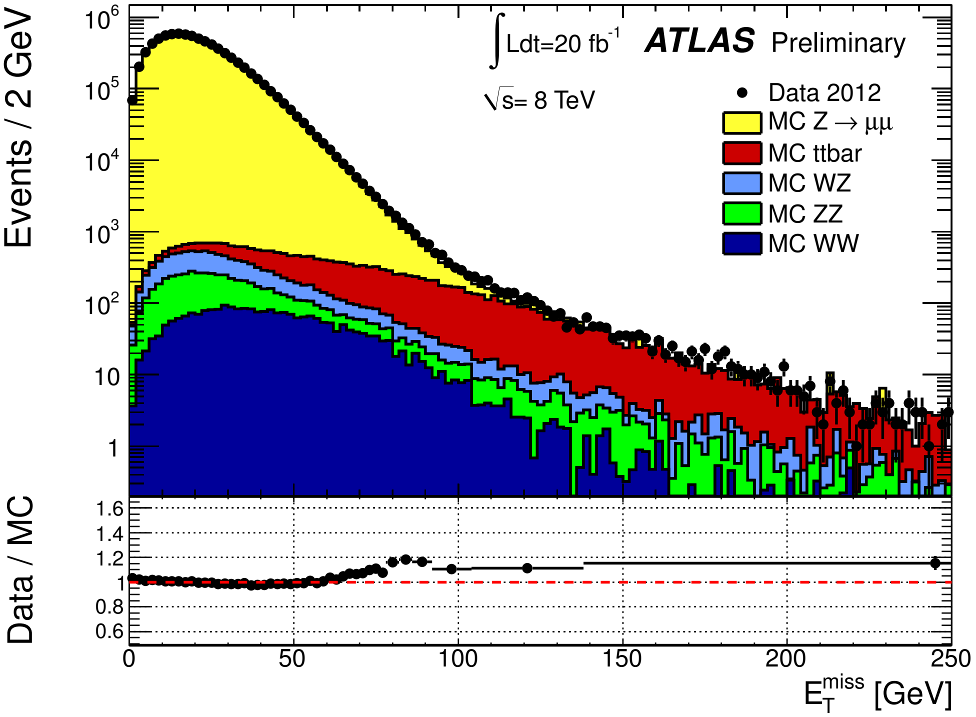

Figure 5.7: The $E_{\mathrm{T}}^{\mathrm{miss}}$ spectrum for $Z \to \mu\mu$ events in data and MC at $\sqrt{s} = 8$ TeV.

6

A Search for High-Mass $t\bar{t}$ Resonances

Searches for high-mass $t\bar{t}$ resonances were first performed at collider experiments at the Tevatron [57, 58], and several searches have been undertaken at ATLAS since the beginning of Run 1 data taking [59, 60].

This search employs a similar strategy to that of the most recent ATLAS search for $t\bar{t}$ resonances in the lepton plus jets channel at $\sqrt{s} = 7$ TeV [61].

6.1 Strategy

$t\bar{t}$ events are divided into four categories by the flavor of the selected lepton and the reconstruction of the hadronic top decay. First, events are separated into the electron and muon channels based on the type of lepton selected in the event. (“Lepton” in this chapter denotes an electron or muon, since τ leptons either decay to a neutrino and hadrons or two neutrinos and a lighter charged lepton.) Second, the events are divided by the reconstruction of the hadronic top quark decay into the boosted and resolved channels.

The boosted selection aims to identify events in which the hadronically decaying top quark's decay products are contained in one large-R ($R = 1.0$) jet. This becomes more likely as the hadronic top p_T grows at higher $m_{t\bar{t}}$. Figure 6.1 illustrates this effect.

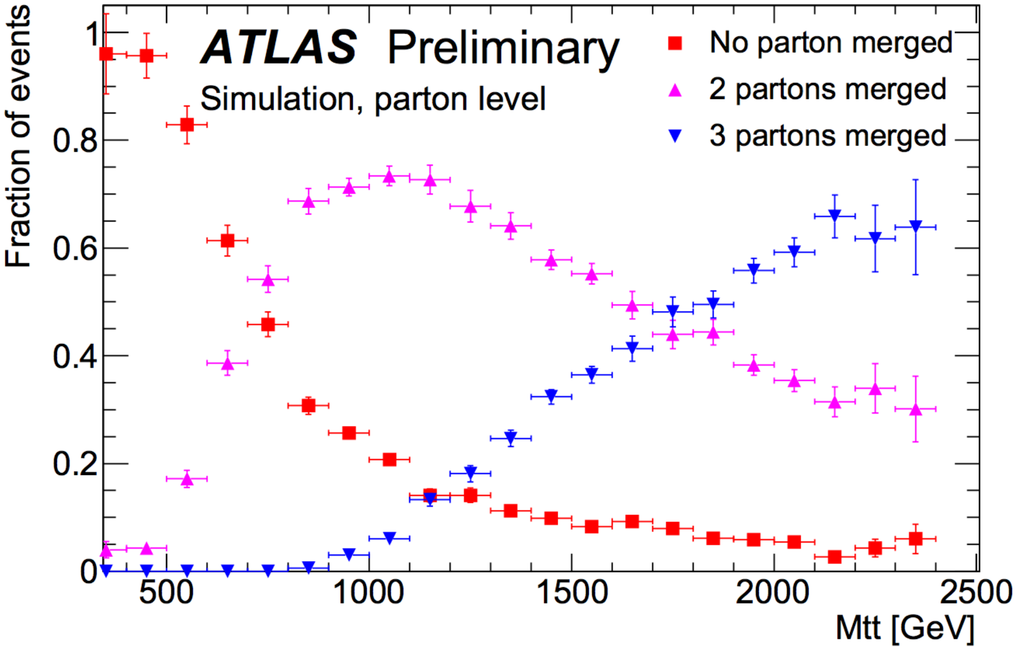

FIGURE 6.1: The probability that three partons from a hadronic top decay are contained in a cone of radius $\Delta R = 0.8$ as a function of the invariant mass of the $t\bar{t}$ system [62].

Events passing the resolved selection must contain several small-R jets consistent with a lower-p_T hadronic top quark decay in which the decay products are not fully merged into a $\Delta R = 1.0$ cone.

Since only events with one selected lepton are reconstructed, there is naturally no overlap in events passing selection in the electron and muon channels, but in order to maintain orthogonality between the boosted and resolved selections, only events failing the boosted selection criteria are categorized as resolved $t\bar{t}$ candidates.

Once event selection is complete, the invariant mass of the $t\bar{t}$ system is reconstructed.

Predictions for background processes are estimated through either Monte Carlo or data-derived methods, depending on the process. The Standard Model $t\bar{t}$ background prediction is derived with MC. After $t\bar{t}$ production, W+jets is the second largest background. Its shape is taken from the Monte Carlo prediction, but its normalization is calculated from the data. The background due to non-prompt leptons (the multijet background) is estimated entirely from data. All other background predictions are derived using MC methods.

The $t\bar{t}$ invariant mass ($m_{t\bar{t}}$) spectrum in the data is tested for local excesses given the Standard Model background predictions. In the absence of any significant deviation from the Standard Model, limits are set on the production cross section $\times$ branching ratio ($\sigma \times$ BR) of BSM particles decaying to $t\bar{t}$ pairs. The benchmark scenarios are the topcolor Z' boson and the RS g_{KK} introduced in Sections 2.2.1 and 2.2.2. The width of the topcolor Z' boson is set to 1.2% of its mass; a width of 15.3% of the mass is chosen for the RS g_{KK}. Monte Carlo simulations are used to generate BSM signal events. The $\sigma \times$ BR limits are subsequently converted into disallowed values of the new particle mass given a set of benchmark scenarios.

6.2 Data sample

Proton-proton collisions at $\sqrt{s} = 8$ TeV delivered by the LHC in 2012 are analyzed. The data are separated into temporal periods, labeled alphabetically, and this analysis utilizes data from periods A-G in which all detector subsystems were operating normally. This corresponds to a total integrated luminosity of $\int \mathcal{L}\, dt = 14.3$ fb^{-1}.

6.3 Monte Carlo samples

In this analysis, Monte Carlo methods are used to predict the $\sigma \times$ BR, efficiency of selection cuts, and $m_{t\bar{t}}$ shape of both the signal benchmarks and various SM backgrounds. The Monte Carlo predictions are normalized to the total integrated luminosity in the data sample, 14.3 fb^{-1}. Particle properties are taken from the Particle Data Group 2010 values [23], except for the top quark mass, which is set to 172.5 GeV. Pile-up events are simulated with PYTHIA8 [63].

6.3.1 $t\bar{t}$ *production*

Standard Model $t\bar{t}$ production is modeled with MC@NLO and HERWIG. MC@NLO [31] version 4.06 with the CT10 [64] parton distribution functions is used to generate events at NLO. Parton showering and hadronization are performed by HERWIG [35]. The $t\bar{t}$ cross section is calculated to be $238.1^{+23.3}_{-25.2}$ pb at approximate next-to-next-to leading order (NNLO) using HATHOR [25] with the MSTW2008NNLO PDF sets [22]. The calculation is confirmed using another approximate NNLO calculation implemented in Top++ 1.0 [65].

POWHEG [32] is used as an alternative to MC@NLO to assess the effect of different NLO generator predictions on the analysis result. POWHEG is also interfaced with both HERWIG and PYTHIA to estimate the influence of different parton shower generators. Predictions from ACERMC [66] interfaced to PYTHIA are used for systematic uncertainty calculations.

6.3.2 W+jets *production*

SM W+jets production is simulated using ALPGEN [30] interfaced to PYTHIA. The sample is exclusively split according to how many partons with $p_T > 15$ GeV are produced in addition to the W boson, from zero up to four ($W + 0$ partons to $W + 4$ partons). The production of more than four additional partons is inclusively generated in one sample ($W + 5$ or more partons). Dedicated MC samples have been produced for W production in association with heavy quarks and additional partons (from $W + c + 0$ partons to $W + c + 4$ or more partons). $W + c$+partons, $W + c\bar{c}$+partons, and $W + b\bar{b}$+partons samples are used. The W+jets normalization is derived from data as presented in Section 6.7.1.

6.3.3 Other backgrounds modeled with Monte Carlo

The additional backgrounds whose predictions are derived from Monte Carlo are single top, Z+jets, and diboson production. Single top events are simulated using two generators. AcerMC interfaced with Pythia is used to model t-channel single top production. The s-channel and W associated t-channel single top production are generated with Powheg interfaced to Pythia.

Z+jets samples are generated similarly to W+jets, introduced in Section 6.3.2. Samples split by the number of additional partons produced are simulated using Alpgen interfaced to Pythia. Dedicated samples for Z bosons produced with heavy quarks are also used. The Standard Model diboson background is predicted using Herwig. Its contribution to the total background is very small, less than 1% in the signal region.

6.3.4 Signal

The topcolor Z' boson signal benchmarks are simulated with Pythia8. Events for a selection of Z' masses between 0.5 and 3.0 TeV were generated using the MSTW2008LO PDF set. The width of the resonance was set to 1.2% of the pole mass.

KK gluon samples were produced with MadGraph [33], and the parton showering was performed with Pythia8. The MSTW2008LO PDF set was again used, and a resonance width of 15.3% of the pole mass was chosen.

6.4 Object selection

6.4.1 Jets

An introduction to jets at ATLAS is presented in Section 5.5. Two jet collections are used in this analysis, anti-k_t with $R = 0.4$ (a "small-R jet" or simply a "jet") and $R = 1.0$ (a "large-R jet" or "fat jet"). LCW calibrated topological clusters are input to the clustering algorithms.

All small-R jets considered in this analysis are required to have $p_T > 25$ GeV, be central: $|\eta| < 2.5$, and have more than 50% of their total track p_T come from the hard scatter: $|\text{JVF}| > 0.5$. The JVF cut is about 90% efficient for jets from the hard scatter vertex with $p_T = 25$ GeV and 98% efficient at 100 GeV. Jets with no associated tracks (and therefore a JVF of -1) automatically pass the JVF requirement.

Large-R jets are only used in the boosted channel of this analysis. Fat jets undergo trimming, as introduced in Section 5.5.4, before any selection is imposed. Once the trimming procedure is complete, large-R jets are required to have $p_T > 300$ GeV, be central: $|\eta| < 2.0$, have a first k_t splitting scale $\sqrt{d_{12}} > 40$ GeV, and have jet mass $m_{jet} > 100$ GeV.

The mass of a jet is given by

$$m_{jet} = \sqrt{\Big(\sum_j E_j\Big)^2 - \Big(\sum_j p_j\Big)^2} \tag{6.1}$$

where the sum is over all jet constituents. The first k_t splitting scale of a jet, $\sqrt{d_{12}}$, is calculated by reclustering the jet constituents using the k_t algorithm [54] and undoing the last step in the cluster sequence. This yields two subjets, for which $\sqrt{d_{12}} = \min(p_T^1, p_T^2) \times \Delta R_{12}$, where ΔR_{12} is the ΔR distance between the two subjets.

The $\sqrt{d_{12}}$ and m_{jet} cuts are motivated by optimizing the rejection of jets from

W+jets and the efficiency of hadronic top decays which are fully-enclosed by the large-R jet [55].

6.4.2 Electrons

The reconstruction of electrons at ATLAS is introduced in Section 5.3. The transverse energy of an electron is defined using the energy of the EM cluster and the pseudorapidity of the track, $E_T = E_{cl}/\cosh\eta_{track}$. This produces the most accurate E_T measurements since the angular resolution of the inner detector is better than the calorimeter's, but the calorimeter has superior energy resolution, especially at high electron transverse momenta. The E_T of an electron must be greater than 25 GeV. The EM cluster associated with an electron is required to be within the precision measurement region of the EM calorimeter, $|\eta| < 2.47$, excepting the transition region, $1.37 < |\eta| < 1.52$. Electrons are also required to pass the `tight++` identification cuts and to be mini-isolated. Lepton mini-isolation will be discussed in detail in Chapter 7, but it is briefly defined here as the scalar sum of the transverse momenta of all tracks within a ΔR cone of radius (10 GeV/p_T^ℓ) excluding the track of the lepton:

$$I^\ell_{mini} = \sum_{tracks} p_T^{track} \qquad \text{with } \Delta R(\ell, track) < 10 \text{ GeV}/p_T^\ell. \tag{6.2}$$

The sum is over all tracks with $p_T > 1$ GeV. Electrons must have $I^e_{mini}/p_T^e < 0.05$.

6.4.3 Muons

An introduction to muon reconstruction at ATLAS can be found in Section 5.4.

Muons in this analysis are required to be combined, have $|\eta| < 2.5$, and have a transverse momentum $p_T > 25$ GeV. The longitudinal impact parameter relative to the primary vertex, $|z0|$, must be smaller than 2 mm; this reduces the number of accepted muons originating from heavy flavor decays. Muons are further required to pass a set of inner detector track criteria: there must be at least one pixel hit and four SCT hits. If a muon passes through a dead sensor silicon sensor, these requirements are reduced by one. The muon should also have a successful track extension into the TRT as long as it is within the pseudorapidity range covered by the TRT.

Muons must pass the same isolation requirement as electrons, $I^{\mu}_{mini}/p^{\mu}_{T} < 0.05$. In order to reduce the non-prompt muon background from heavy quark decays, they are also required to be separated by at least $\Delta R(\mu,\ jet) > 0.1$ from the nearest small-R jet which passes the jet p_T and JVF cuts.

6.4.4 Object overlap removal

Since both electrons and jets are reconstructed from calorimeter deposits, it is possible that an accepted electron and an accepted jet will be built from the energy deposits from the same particle. To avoid this energy double counting, either the electron or jet must be removed when they overlap. If the closest jet to an accepted electron is within a ΔR distance of 0.2, the jet and electron are considered to be the same object, namely the electron, and the jet is removed from the event. Afterward, if the electron is still within a ΔR distance of 0.4 to the closest selected jet (not counting the one possibly removed in the previous step), the electron is considered a constituent of the jet and is removed to avoid energy double-counting.

Improvements to this overlap procedure developed by the author are discussed in depth in Section 7.3.

6.4.5 Missing transverse momentum

The missing transverse energy in this analysis is used to estimate the transverse momentum of the neutrino in the lepton plus jets final state. The calorimeter energy associated with any electron passing the `tight++` definition is calibrated as an electron and taken into account. Jets with $p_T > 20$ GeV are included next after being calibrated to the LC+JES energy scale. Next, the contributions of soft jets with 10 GeV $< p_T <$ 20 GeV and muons are added. Muons reconstructed in the full range of the muon systems are included in the $E_{\mathrm{T}}^{\mathrm{miss}}$ calculation, not only those with $|\eta| < 2.5$. Finally, the missing transverse energy from any cell not associated with a high-p_T object is taken into account.

In summary, the missing transverse energy of the event is given by

$$E_{x,y}^{miss} = E_{x,y}^{\mathrm{electrons}} + E_{x,y}^{\mathrm{jets}} + E_{x,y}^{\mathrm{soft\ jets}} + E_{x,y}^{\mathrm{muons}} + E_{x,y}^{\mathrm{other\ cells}}. \tag{6.3}$$

6.5 Event selection

The event selection is split into three parts: the common selection, the boosted selection, and the resolved selection. The common selection is shared between both the boosted and resolved channels and includes event quality cuts, trigger requirements, and cuts involving the leptonic W decay products. If an event passes the common selection, the boosted selection is applied. Events which pass the boosted selection criteria are considered $t\bar{t}$ candidate events and are used in the final $m_{t\bar{t}}$ spectrum. Those which fail the boosted selection criteria are subsequently passed through the resolved selection cuts. They are used in the final $m_{t\bar{t}}$ spectrum if they fulfill all the resolved selection requirements.

6.5.1 Common event selection

The common event selection is applied to all events in the following order.

6.5.1.1 Good runs list and $\langle\mu\rangle$ reweighting

Data events must come from LHC collisions for which the ATLAS detector subsystems were operating normally. A list of sections of runs, aptly named the "good runs list," that are deemed suitable for physics analysis is compiled with the input of subdetector experts, and events which are a part of unsuitable run sections are discarded.

No selection is applied to MC events at this stage, but a correction is applied to account for discrepancies in the distribution of the number of pile-up events in the data and simulation. Data runs are split into smaller periods called luminosity blocks, and the average number of interactions per bunch crossing, $\langle\mu\rangle$, is measured over them. Generated events are reweighted at this stage in order to bring the simulated $\langle\mu\rangle$ distribution in line with the actual $\langle\mu\rangle$ distribution in data.

6.5.1.2 Calorimeter quality

Events with corrupted data from the tile calorimeter or with excessive noise in the liquid argon calorimeter are removed next.

6.5.1.3 Trigger

Events are then required to fire one of four triggers. Electrons must fire either a trigger with a nominal p_T cut of 24 GeV or a high-p_T trigger with a p_T cut of 60 GeV. Both triggers require electrons to pass identification requirements similar to the `medium++` selection. The 24 GeV trigger has additional cuts on the hadronic activity near the electron to reduce the trigger rate. Muons must fire a 24 GeV or 36 GeV trigger, but the lower-p_T trigger rejects muons with a large amount of calorimeter activity nearby.

6.5.1.4 Hard scatter vertex quality

The primary vertex with the highest scalar sum of constituent track p_Ts is considered the hard scatter vertex. It is required to have 5 or more associated tracks with $p_T^{\text{track}} > 400$ MeV.

6.5.1.5 Leptons

Events with exactly one selected muon and zero selected electrons are muon channel candidate events, and those with exactly one electron and zero muons are electron channel candidate events. Events with zero or more than one selected lepton are discarded.

6.5.1.6 Trigger match

The selected lepton is required to match the lepton that fired the trigger. A maximum ΔR of 0.15 is allowed to separate the object that fired the trigger and the selected lepton. They must also be the same flavor.

6.5.1.7 Jet quality

If any jet in the event is determined to have come from interactions between the beam and the gas within the beam pipe, beam interactions with other structures external to ATLAS, cosmic ray muons, or calorimeter noise, the event is discarded.

6.5.1.8 Missing transverse energy and transverse mass

The decay of the W boson results in $E_{\mathrm{T}}^{\mathrm{miss}}$ in $t\bar{t}$ events that is generally larger than that of the non-prompt backgrounds. The multijet background is significantly reduced by cuts on the event $E_{\mathrm{T}}^{\mathrm{miss}}$ and transverse mass, m_T. The transverse mass is defined as

$$m_T = \sqrt{2p_T^{\ell} E_{\mathrm{T}}^{\mathrm{miss}}(1 - \cos\Delta\phi)}, \tag{6.4}$$

where $\Delta\phi$ is the azimuthal separation between the lepton and the missing transverse energy direction.

In the muon channel, a cut of $E_{\mathrm{T}}^{\mathrm{miss}} > 20$ GeV and $E_{\mathrm{T}}^{\mathrm{miss}} + m_T > 60$ GeV is applied. The $E_{\mathrm{T}}^{\mathrm{miss}} + m_T$ cut was derived based on the triangular shape of the non-prompt multijet background in $E_{\mathrm{T}}^{\mathrm{miss}} - m_T$ space in the muon channel.

The electron channel is more susceptible to non-prompt backgrounds from light quark jets, so a stronger $E_{\mathrm{T}}^{\mathrm{miss}}$ cut is made to reject these backgrounds: $E_{\mathrm{T}}^{\mathrm{miss}} > 30$ GeV and $m_T > 30$ GeV.

6.5.2 Boosted event selection

Events passing all common cuts are tested for compatibility with boosted $t\bar{t}$ event reconstruction. The boosted selection aims to identify events in which the hadronically decaying top quark's decay products are contained in one large-R jet.

6.5.2.1 Small-R jet from leptonically decaying top quark

First, the jet resulting from the leptonic top decay $t \to b\ell\nu$ is identified. An accepted small-R jet must be reconstructed within $\Delta R(\ell,\ jet) < 1.5$ of the selected lepton. The highest-p_T small-R jet that satisfies this requirement is assumed to represent the b quark from the leptonically decaying top quark. It is henceforth referred to as the leptonic top b jet.

6.5.2.2 Hadronic top quark jet

The boosted selection requires a high-p_T large-R jet with substructure that indicates it contains a hadronic top quark decay. In addition to the p_T, η, m_{jet}, and $\sqrt{d_{12}}$ requirements imposed on all large-R jets, the hadronic top quark candidate must be separated from the leptonic top b jet by $\Delta R > 1.5$. This ensures that no calorimeter cells are shared by the two jets. The large-R jet candidate must also be an azimuthal distance $\Delta\phi > 2.3$ from the selected lepton. If more than one fat jet fulfills these criteria, the one with the highest-p_T is assumed to be the hadronic top quark jet.

6.5.2.3 b-tagged jet

Finally, at least one selected small-R jet in the event must be b-tagged using the MV1 algorithm at the 80% efficiency operating point [67]. The MV1 algorithm uses both tracking and calorimeter information for a jet to determine the likelihood that it originated from a b-quark. For instance, due to the relatively long lifetime of B hadrons, a secondary vertex is often reconstructible from the tracks of its decay products. b-tagging algorithms take advantage of this in order to discriminate light-flavor jets from b jets. Only 5% of jets not originating from b quarks pass this requirement [68]. The b-tagged jet need not be the leptonic top b jet.

6.5.3 Resolved selection

Events passing the common selection cuts but failing the boosted selection are tested for consistency with a lower-p_T hadronic top decay than that assumed in the boosted scenario.

6.5.3.1 Small-R jets

The small-R jets requirement is split into two cuts, one of which must be passed. If there are four selected small-R jets in the event, the event is selected. Each jet corresponds to one quark in the $t\bar{t} \to b\bar{b}\ q\bar{q}\ \ell\nu$ event topology. If there are only three selected small-R jets in the event, one of them must have a mass $m_{jet} > 60$ GeV. This enhances the efficiency of events with a hadronic top decay that is not completely contained in large-R jet but with a high-p_T W boson whose decay products have merged into one small-R jet.

6.5.3.2 b-tagged jet

The resolved event selection has an identical b-tagged jet requirement to the boosted selection. At least one selected small-R jet in the event must be b-tagged using the MV1 tagger at the 80% efficiency working point.

6.5.4 Selection efficiency

Figure 6.2 shows the efficiency of the boosted and combined selections in each lepton flavor channel. The efficiency depends strongly on the top quark transverse momenta, which are correlated with the invariant mass of the $t\bar{t}$ system. Most accepted events with $m_{t\bar{t}} < 1$ TeV fall into the resolved category. This is largely because the hadronic top quark decay products are not fully contained in the large-R jet required by the boosted selection. However, the majority of accepted events with $m_{t\bar{t}} > 1.5$ TeV fall into the boosted category.

The muon channel is more efficient at high $m_{t\bar{t}}$ because muons are reconstructed closer to jets ($\Delta R > 0.1$) than electrons ($\Delta R > 0.4$). This is inefficient for highly boosted leptonically decaying tops because the lepton and b-quark are not well-separated. See Chapter 7 for more details. At low $m_{t\bar{t}}$ the efficiency difference between lepton channels is due to higher muon reconstruction efficiency and looser $E_{\mathrm{T}}^{\mathrm{miss}}$ and m_T cuts.

6.6 Event reconstruction

The invariant mass of the $t\bar{t}$ system is calculated differently in the boosted and resolved channels. If there are more than four accepted small-R jets in a resolved event, it must be determined which four were most likely to come from the hadronic top decay (3 jets) and the leptonic top decay (1 jet). In the boosted channel there is no ambiguity: the highest-p_T small-R jet close to the lepton and the chosen large-R jet are used. In both channels the neutrino p_z must be estimated.

6.6.1 Neutrino p_z

The longitudinal momentum of the neutrino, p_z, is not measurable by the ATLAS detector. It is calculated by requiring the invariant mass of the lepton-neutrino system to be the pole mass of the W boson, M_W [69]. This treatment yields the

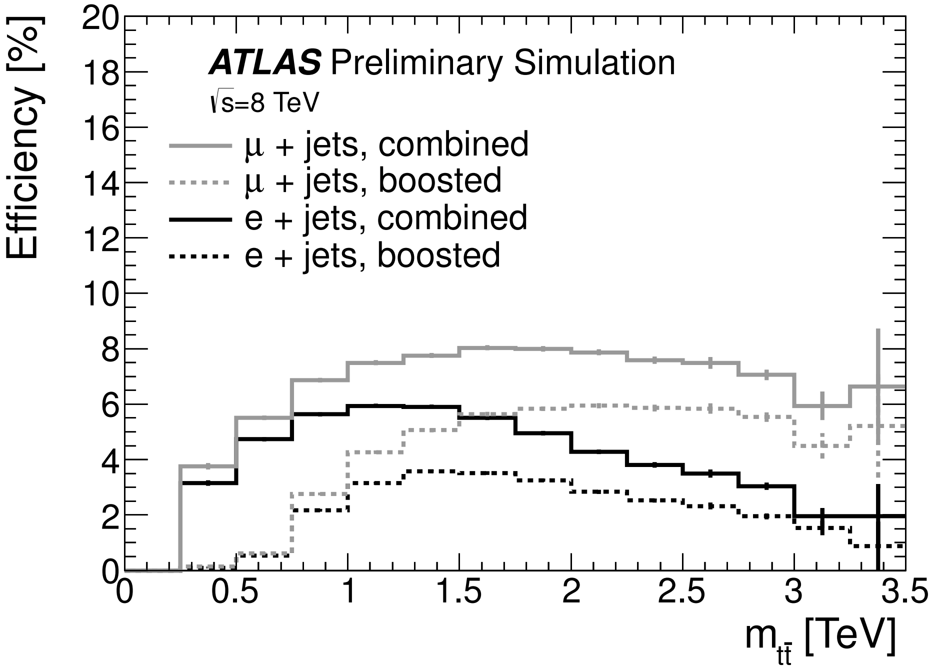

FIGURE 6.2: The selection efficiency of the $t\bar{t}$ resonances analysis as a function of $m_{t\bar{t}}$. The efficiency of the muon (gray) and electron (black) channels are shown separately. The boosted (solid) and combined boosted+resolved efficiencies are presented for each lepton flavor. The denominator of the efficiency measurement is the number of $t\bar{t}$ events which decay to an electron or muon, neutrino, and four quarks.

quadratic equation

$$p_{z,\nu}^{\pm} = \frac{\mu p_{z,\ell}}{p_{T,\ell}} \pm \sqrt{\frac{\mu^2 p_{z,\ell}^2}{p_{T,\ell}^4} - \frac{E_\ell^2 p_{T,\nu}^2 - \mu^2}{p_{T,\ell}^2}}, \tag{6.5}$$

where $\mu = M_W^2 + p_{T,\ell} p_{T,\nu} \cos \Delta\phi_{\ell\nu}$. About 70% of selected events have at least one real solution to this equation. If more than one solution exists, that with the smaller $|p_z|$ is used in the boosted channel. Figure 6.3 shows the difference between the reconstructed and true neutrino p_z in $t\bar{t}$ events when choosing the larger and smaller $|p_z|$ value.

In the resolved channel, both p_z solutions are considered; see Section 6.6.2 for details.

If $M_W^2 < 2p_{T,\ell}p_{T,\nu}(1 - \cos\Delta\phi_{\ell\nu})$ there will be no real solutions, and in this case the x and y components of the $E_{\mathrm{T}}^{\mathrm{miss}}$ are adjusted minimally until a real solution is found.

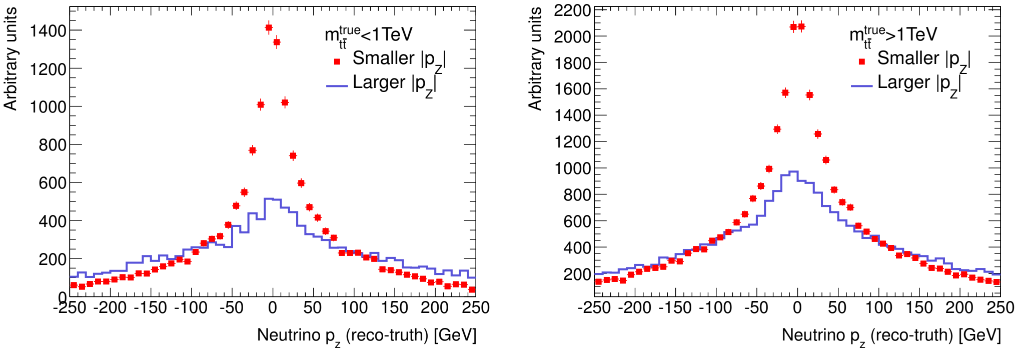

FIGURE 6.3: The difference between the computed and true neutrino p_z in $t\bar{t}$ events with $m_{t\bar{t}} < 1$ TeV (left) and $m_{t\bar{t}} > 1$ TeV (right). The choice of the smaller $|p_z|$ solution has a better resolution in both cases.

6.6.2 Resolved event reconstruction

If only three jets (one with $m_{jet} > 60$ GeV) are selected in an event passing the resolved selection, the four-momenta of those three jets are included in the $m_{t\bar{t}}$ calculation. Likewise, if only four jets (none with $m_{jet} > 60$ GeV) are selected, all of their four-momenta are used.

In all other cases, a χ^2 algorithm is used to determine which jets in the event most probably originated from the $t\bar{t}$ pair. Different permutations of jets are considered, and the permutation with the smallest χ^2 is used to reconstruct the invariant mass of the $t\bar{t}$ system. If two neutrino p_z solutions were found, they are both tested with all jet permutations.

The χ^2 for a set of three jets $(j1, j2, j3)$ and the b jet candidate (b) is defined as

$$\chi^2 = \left[\frac{m_{j1j2} - m_W}{\sigma_W}\right]^2 + \left[\frac{m_{bj1j2} - m_{j1j2} - m_{t_{had}-W}}{\sigma_{t_{had}-W}}\right]^2 + \left[\frac{m_{j3\ell\nu} - m_{t_{lep}}}{\sigma_{t_{lep}}}\right]^2 + \left[\frac{(p_{T,bj1j2} - p_{T,j3\ell\nu}) - (p_{T,t_{had}} - p_{T,t_{lep}})}{\sigma_{p_{T,diff}}}\right]^2. \tag{6.6}$$

Here the expected masses of the hadronic W (m_W), the hadronic top quark minus the hadronic W mass $(m_{t_{had}-W})$, and the leptonic top quark $(m_{t_{lep}})$ are derived from MC when the jets are chosen by matching them to the original quarks from the top quark decays. The expected difference in p_T between the hadronic and leptonic top quarks $(p_{T,t_{had}} - p_{T,t_{lep}})$ and the standard deviations (σ) are derived using the same MC matching criteria. Their derived values are shown in Table 6.1.

The first term of the χ^2 imposes the W mass constraint on two of the jets. The second term similarly imposes the top mass constraint on three of the jets, but the mass of the two jets from the hadronic W decay is subtracted in order to remove the correlation between terms. The third term is the mass constraint of the leptonically decaying top. The final term constrains the event to not have a large p_T difference between the two reconstructed top quarks, as is expected for Standard Model $t\bar{t}$ production and $t\bar{t}$ resonances.

If one of the selected jets has $m_{jet} > 60$ GeV, the χ^2 algorithm is altered to take this into account:

$$\chi^2 = \left[\frac{m_{Jj1} - m_{t_{had}}}{\sigma_{t_{had}}}\right]^2 + \left[\frac{m_{j2\ell\nu} - m_{t_{lep}}}{\sigma_{t_{lep}}}\right]^2 + \left[\frac{(p_{T,Jj1} - p_{Tj2\ell\nu}) - (p_{T,t_{had}} - p_{T,t_{lep}})}{\sigma_{p_{T,diff}}}\right]^2, \tag{6.7}$$

where J is the high-mass jet. The additional parameters are again derived from

Monte Carlo and are shown in Table 6.1.

Table 6.1: Monte Carlo-derived parameters for the resolved χ^2 event reconstruction algorithm

Parameter	Value
m_W	83.3 GeV
σ_W	10.8 GeV
$m_{t_{had}-W}$	91.1 GeV
$\sigma_{t_{had}-W}$	14.2 GeV
$m_{t_{lep}}$	168.2 GeV
$\sigma_{t_{lep}}$	20.6 GeV
$p_{T,t_{had}} - p_{T,t_{lep}}$	-8.7 GeV
$\sigma_{p_{T,diff}}$	55.0 GeV
$m_{t_{had}}$	173.5 GeV
$\sigma_{t_{had}}$	16.3 GeV

Once the jets and, if need be, the neutrino p_z solution have been chosen, the invariant mass of the $t\bar{t}$ system is constructed as the four-vector sum of all chosen jets, the neutrino, and the lepton.

Figure 6.4 illustrates the mass spectrum and the performance of the $m_{t\bar{t}}$ reconstruction for various signal benchmarks with resolved events. The reconstructed $m_{t\bar{t}}$ as a function of the true $m_{t\bar{t}}$ in resolved events is found in Figure 6.5.

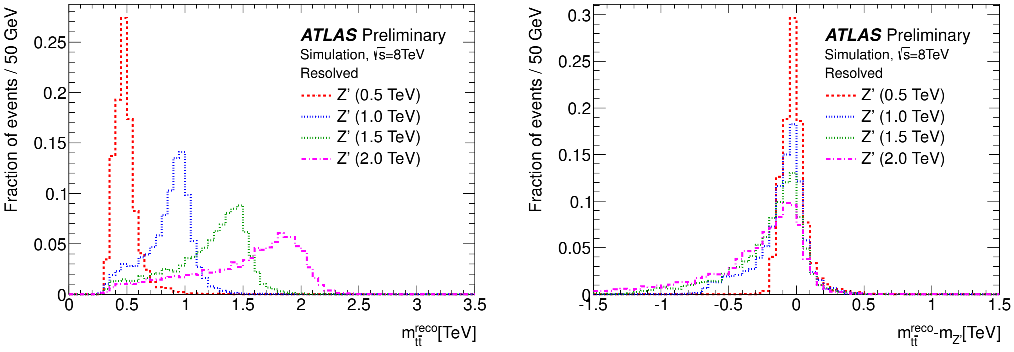

Figure 6.4: $m_{t\bar{t}}$ reconstruction performance in resolved events. The reconstructed $t\bar{t}$ invariant mass spectrum for a range of Z' masses (left) and the difference between the true and reconstructed Z' mass (right) are shown.

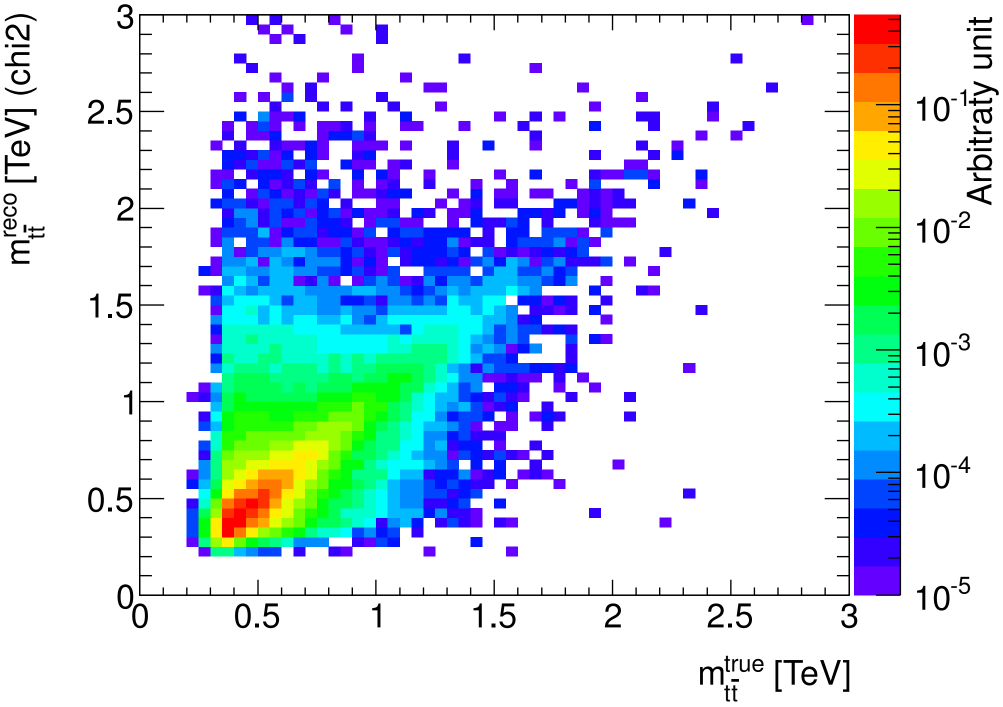

FIGURE 6.5: The true $m_{t\bar{t}}$ vs reconstructed $m_{t\bar{t}}$ in resolved events after full event selection and χ^2 selection of jets.

6.6.3 Boosted event reconstruction

The objects which are used in the $m_{t\bar{t}}$ reconstruction in the boosted channel are determined during event selection. The invariant mass of the $t\bar{t}$ system is defined as the mass of the summed neutrino, lepton, hadronic top jet, and leptonic top b jet four momenta.

Figure 6.6 shows the mass spectrum and the performance of the $m_{t\bar{t}}$ reconstruction for various signal benchmarks in boosted events.

6.7 Data-driven background estimation

Not all SM backgrounds to possible exotic $t\bar{t}$ resonances are accurately modeled with Monte Carlo methods. Estimates for the W+jets background and backgrounds with non-prompt leptons are derived partially or fully from the LHC collision data.

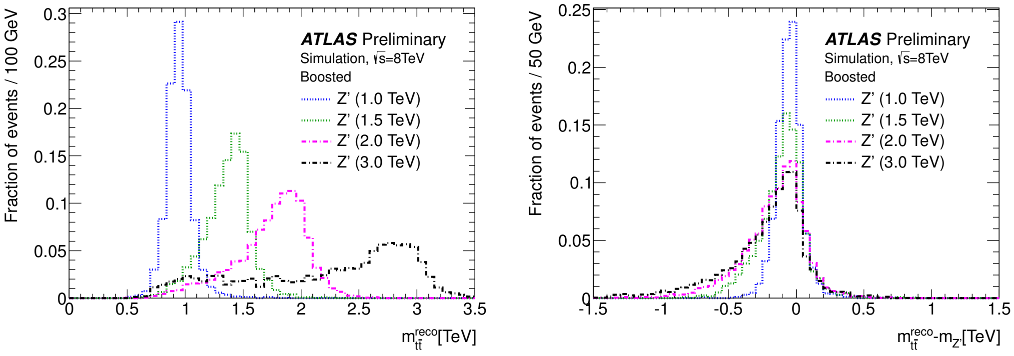

FIGURE 6.6: $m_{t\bar{t}}$ reconstruction performance in boosted events. The reconstructed $t\bar{t}$ invariant mass spectrum for a range of Z' masses (left) and the difference between the true and reconstructed Z' mass (right) are shown.

6.7.1 W+jets background

ALPGEN has been shown to model W+jets production accurately for leptons and jets with modest transverse momenta ($20-75$ GeV) [70], but the purpose of this analysis is to probe new physics above 1 TeV. It is not assumed that Monte Carlo correctly predicts the mixture of events with different extra parton multiplicities, nor is it assumed that ALPGEN produces the correct mixture of W+light- and heavy-flavor jets.

The W+jets MC predictions are corrected using scale factors (SFs) derived from data. Two different corrections are applied.

First, a correction is derived for the relative fractions of $W+c$, $W+c\bar{c}$, $W+b\bar{b}$, and W+light flavor jets predicted by the MC. A W+jets-enriched control region is defined by applying the common selection from Section 6.5.1, then requiring at least two small-R jets. The data from this control region are binned by their number of b-tagged jets (0, 1, or 2 or more) and the charge of the lepton, yielding a total of six bins. The W+jets samples are split into three components: W+light quarks, $W+c$, and $W+c\bar{c}$ or $b\bar{b}$. The normalization of each W+jets component is then floated to obtain the best fit to the data in the six bins. The ratio between the fitted normalization and the original normalization is the scale factor for a particular W+jets component and is applied to all MC W+jets events. An uncertainty on this method is assessed by floating the W+jets components together in three different ways: W+light and W+heavy, ($W + c\bar{c}$ or $b\bar{b}$) and (W+light or c); W+c and ($W + c\bar{c}$ or $b\bar{b}$ or light). The scale factors are redetermined for each grouping, and the difference from the nominal SF is taken as an uncertainty.

In the resolved channel, the overall W+jets normalization is obtained by measuring the ratio between W^+ and W^- events, which is understood to better precision than the inclusive $W^\pm$+jets cross section [71]. The major backgrounds in this control region ($t\bar{t}$ and multi-jet) are charge-symmetric. The total number of W+jets events in data, $N_{W^+} + N_{W^-}$, is given by

$$N_{W^+} + N_{W^-} = \left(\frac{r_{MC}+1}{r_{MC}-1}\right)(D_+ - D_-), \tag{6.8}$$

where r_{MC} is the ratio of the number of W^+ to the number of W^- events in the MC prediction and $D_\pm$ is the number of data events with a lepton of charge ± 1. The predicted contribution of charge-asymmetric events from smaller backgrounds (single top and diboson) is accounted for by subtracting their yields from the data counts. This calculation is performed for events passing the common selection with exactly three jets (for events with one jet having $m_{jet} > 60$ GeV) and those with four or more (for all other events). The uncertainty on the overall normalization is taken from statistical uncertainties and the object reconstruction uncertainties outlined in Section 6.9.2.

The W+jets overall normalization estimation in the boosted channel uses the same procedure as the resolved case, but instead of requiring 3 or more small-R jets, events with a large-R jet with $p_T > 300$ GeV are used.

6.7.2 Multijet background

Since the production rates of QCD processes are very large, a small amount of MC mismodeling in the misidentification of leptons from QCD sources will result in a large uncertainty on the prediction. The background from non-prompt lepton sources is therefore estimated from the collision data using the so-called matrix method.

First, the lepton identification cuts are loosened. A loose electron in this case must pass the `medium++` requirements and need not be isolated, while a loose muon must pass all identification cuts except the isolation requirement. The efficiency ϵ is defined as the probability that a loose lepton from a prompt source, e.g. a W or Z boson decay, passes the full lepton requirements of the analysis. The false-identification rate f is similarly defined: it is the probability that a loose lepton from a non-prompt source passes the full lepton requirements. ϵ and f are parameterized in terms of the lepton p_T and the ΔR distance to the nearest jet, which they were found to depend on strongly.

In order to measure f, a control region enriched with QCD events is defined for each channel to obtain a pure sample of non-prompt leptons. In the boosted channel, control region events must have no large-R jets with $p_T > 150$ GeV, and the $E_{\mathrm{T}}^{\mathrm{miss}}$ and m_T signal region cuts are inverted. In the resolved channel, only the $E_{\mathrm{T}}^{\mathrm{miss}}$ and m_T cuts are inverted. Once a sample of data events has been selected using these criteria, the contamination due to leptons from prompt sources is subtracted using Monte Carlo predictions. The false-identification rate is then derived by dividing the number of leptons passing the full analysis criteria by those passing the loose definition in bins of p_T and the ΔR distance to the nearest jet.

ϵ is measured using Monte Carlo samples. Events passing all selection cuts except the lepton requirement are first preselected. The number of events with a lepton passing the loose definition is the denominator of the efficiency, and the number with a lepton passing the full lepton selection is the numerator. Like the false-identification rate, ϵ is derived in the p_T and $\Delta R(\ell,\ jet)$ bins.

Once ϵ and f have been calculated, the resolved and boosted event selections are applied in the data, but events are only required to have a loose lepton. The number of loose leptons in this sample, N_L, is given by

$$N_L = N_p + N_{np}, \tag{6.9}$$

where N_p and N_{np} are the number of prompt and non-prompt leptons, respectively. After imposing the full lepton selection, the number of "tight" leptons, N_T, is given by

$$N_T = \epsilon N_p + f N_{np}. \tag{6.10}$$

Combining these two equations, the number of non-prompt leptons passing the full selection, fN_{np}, is

$$fN_{np} = \frac{(\epsilon - 1)f}{\epsilon - f} N_T + \frac{\epsilon f}{\epsilon - f} N_A, \tag{6.11}$$

where N_A is the number of leptons that pass the loose definition but fail the full selection, $N_L - N_T$.

The final prediction of the non-prompt contribution to the total yield is determined by weighting each data event with a loose lepton by the appropriate factor–$(\epsilon - 1)f/(\epsilon - f)$ if the lepton is tight and $(\epsilon f)/(\epsilon - f)$ if it is not tight. The uncertainty on this prediction is assessed by varying the loose lepton definition, the QCD control region cuts, and the parameterization of ϵ and f.

6.8 Data and background estimation comparisons

6.8.1 Event yield comparison

The detailed event yields in data and background predictions are presented by channel and lepton flavor in Table 6.2. 280,251 data events pass the resolved selection, while 5122 pass the boosted selection. The overlap between the two channels is 4589 events. These overlapping events are reconstructed using the boosted event reconstruction algorithm presented in Section 6.6.3.

The predicted background event yields in the resolved and boosted channels are 283000 ± 39000 and 5600 ± 1200, respectively. The uncertainties quoted here include systematic uncertainties, discussed in Section 6.9. The dominant Standard Model background is $t\bar{t}$ production, which accounts for approximately 75% (85%) of accepted events in the resolved (boosted) channel. W+jets and single top production are the next most significant backgrounds, making up about 15% and 5% (10% and 3%) of the total predicted background.

No significant excess or deficit is observed in the data when compared with the Standard Model expectation.

6.8.2 Comparison of kinematic distributions

A comparison of data and the background predictions for important kinematic distributions is presented in this section. The p_T of the leading (highest-p_T) selected jet in each data event passing the resolved selection is compared to the background prediction in Figure 6.7. The mass of the leptonically decaying top candidate, $m^{t,lep}$, in data and background is shown in Figure 6.8. Similar data and background comparisons for the hadronic top jet candidate mass and p_T are made in Figures 6.9 and 6.10, respectively.

No significant deviation from the predictions is observed in the data.

Table 6.2: The number of selected data events and SM background expectations after the full resolved or boosted selections. The Poisson statistical uncertainty is shown for data yields. The systematic uncertainties on the background yields, discussed further in Section 6.9 are also shown.

	Resolved selection		
	e	μ	Sum
$t\bar{t}$	94000 ± 15000	118000 ± 19000	211000 ± 33000
Single top	6800 ± 800	8400 ± 1100	15200 ± 1900
Multi-jet	3700 ± 1800	10000 ± 5000	14000 ± 6000
W+jets	16000 ± 4000	23000 ± 6000	39000 ± 10000
Z+jets	1800 ± 400	1800 ± 400	3600 ± 800
Di-bosons	230 ± 50	320 ± 60	550 ± 100
Total	121000 ± 17000	162000 ± 23000	283000 ± 39000
Data	119490 ± 346	160878 ± 401	280251 ± 529
	Boosted selection		
	e	μ	Sum
$t\bar{t}$	2100 ± 500	2800 ± 600	4900 ± 1100
Single top	71 ± 15	105 ± 22	176 ± 34
Multi-jet	39 ± 19	32 ± 16	71 ± 25
W+jets	170 ± 60	310 ± 90	480 ± 140
Z+jets	18 ± 11	33 ± 8	52 ± 15
Di-bosons	2.0 ± 0.8	1.5 ± 1.4	3.5 ± 1.8
Total	2400 ± 500	3300 ± 700	5600 ± 1200
Data	2177 ± 47	2945 ± 54	5122 ± 72

6.9 Systematic uncertainties

The sources of systematic uncertainty affecting this analysis are discussed in this section. They are broken up into two broad categories: uncertainties from the background and signal estimates and uncertainties due to object reconstruction and identification. The sources of uncertainty on the background and signal estimates include Monte Carlo modeling, luminosity, cross section, and data-driven backgrounds. The calibration and identification of electrons, muons, jets, and missing transverse energy are sources of systematic uncertainties on object reconstruction.

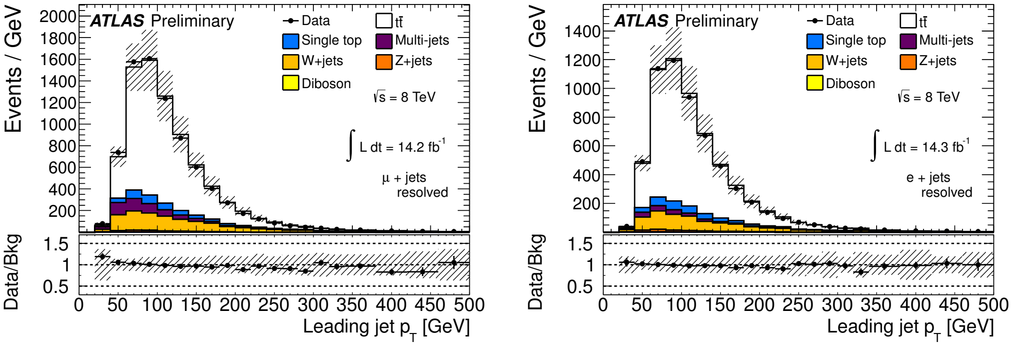

FIGURE 6.7: The leading jet p_T distribution in data and background in the resolved muon (left) and electron (right) channels. The shaded area indicates the total uncertainty on the background prediction. The Poisson statistical uncertainty on the data is also shown. The contribution of certain backgrounds may be too small to see in the figure. The right-most bin includes the contribution from overflow events.

Uncertainties can affect both the overall normalization of the predicted $m_{t\bar{t}}$ spectrum as well as its shape, so although the uncertainty in the event yield due to a systematic uncertainty may be small, its effect on the predicted $m_{t\bar{t}}$ distribution, and therefore the $\sigma \times$ BR limit for a signal benchmark, may be substantial.

6.9.1 Uncertainties affecting the background estimate

6.9.1.1 Luminosity

The uncertainty on the luminosity in 2012 LHC $\sqrt{s} = 8$ TeV data taking is 3.6%. This is applied as a constant shift to all background processes which are predicted entirely from Monte Carlo. Backgrounds whose normalization (W+jets, multijet) comes from the data are not affected by this uncertainty.

6.9.1.2 Parton distribution functions

The uncertainty due to choice of PDF is assessed for all signals and backgrounds except the multijet background, which is fully derived from data. The procedure outlined in the PDF4LHC recommendation [72] is used to evaluate it. The 68% confidence limit uncertainties on the CT10, MSTW2008NLO, and NNPDF2.3 [73]

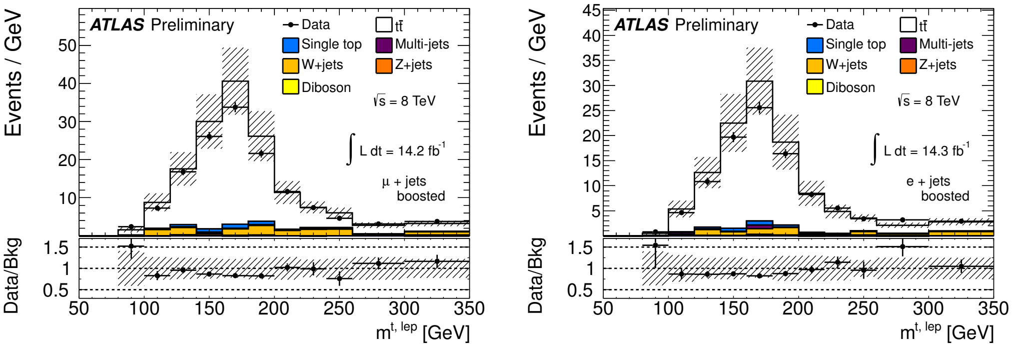

FIGURE 6.8: The leptonically decaying top quark candidate mass, $m^{t,lep}$, distribution in data and background in the boosted muon (left) and electron (right) channels. The shaded area indicates the total uncertainty on the background prediction. The Poisson statistical uncertainty on the data is also shown. The contribution of certain backgrounds may be too small to see in the figure. The right-most bin includes the contribution from overflow events.

PDF predictions are applied to each background.

In practice, this is performed by reweighting each event based on the relative probability of the hard scatter occurring according to a given PDF. Each PDF family is composed of between 40 and 100 PDFs which cover the 68% confidence interval. An uncertainty envelope prescribed by the PDF4LHC recommendation is defined for each PDF family, and the maximum deviation up and down from the nominal $m_{t\bar{t}}$ spectrum of all the envelopes is taken as the total PDF uncertainty.

Since the cross section uncertainty on background processes includes the uncertainty due to the choice of PDF, each background sample is normalized to the original number of events before cuts are applied.

6.9.1.3 Uncertainties on Standard Model $t\bar{t}$ production

Several systematic uncertainties related to the dominant SM $t\bar{t}$ background are assessed.

The largest normalization uncertainty on the overall background prediction is due to the uncertainty of the $t\bar{t}$ production cross section. It is evaluated with

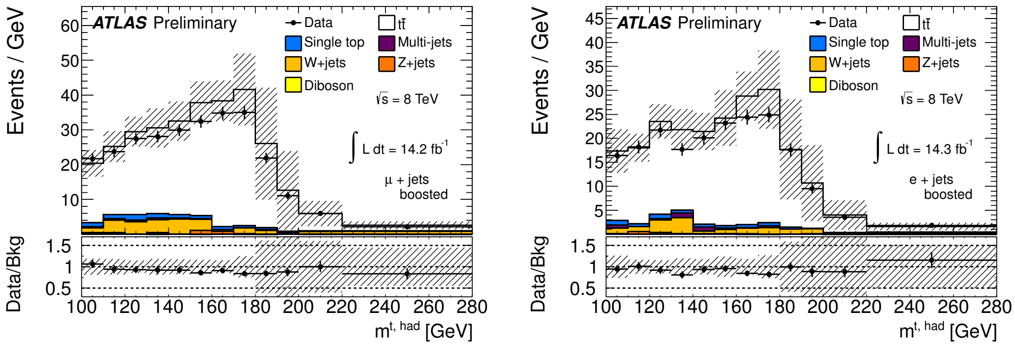

FIGURE 6.9: The hadronically decaying top quark candidate mass, $m^{t,had}$, distribution in data and background in the boosted muon (left) and electron (right) channels. The shaded area indicates the total uncertainty on the background prediction. The Poisson statistical uncertainty on the data is also shown. The contribution of certain backgrounds may be too small to see in the figure. The right-most bin includes the contribution from overflow events.

HATHOR [25] using the MSTW2008 90% confidence level NNLO PDF sets [22]. A further cross section uncertainty derived by changing the top quark mass by ±1 GeV is also included. Finally, the full uncertainty on the $t\bar{t}$ production cross section is calculated by adding both of these in quadrature with the normalization and factorization scale uncertainties. The overall uncertainty is found to be consistent with the Top++ [65] next-to-next-to-leading log calculation.

To assess the effect of the choice of NLO $t\bar{t}$ generator, the difference in the $m_{t\bar{t}}$ spectrum when using MC@NLO and POWHEG is considered an uncertainty on the SM $t\bar{t}$ background. HERWIG is used for parton showering in both cases. A similar comparison is made between POWHEG samples showered with PYTHIA and HERWIG, and the difference is taken as an additional systematic uncertainty.

A shape uncertainty due to value of the top quark mass is evaluated through the change in the $m_{t\bar{t}}$ shape with the top quark mass set to 170 and 175 GeV with MC@NLO. The difference in the $m_{t\bar{t}}$ spectrum between these two masses is divided by four to approximate a 1.25 GeV uncertainty on the top mass. To avoid double

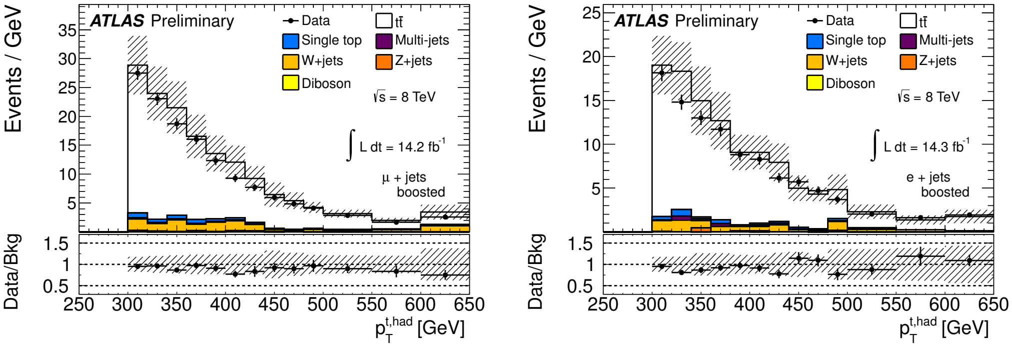

FIGURE 6.10: The hadronic top jet candidate p_T distribution in data and background in the boosted muon (left) and electron (right) channels. The shaded area indicates the total uncertainty on the background prediction. The Poisson statistical uncertainty on the data is also shown. The contribution of certain backgrounds may be too small to see in the figure. The right-most bin includes the contribution from overflow events.

counting the effect of the top mass on the $t\bar{t}$ production cross section, each variation is normalized to the nominal cross section.

Finally, the uncertainty due to initial and final state radiation (ISR, FSR) is evaluated by generating two $t\bar{t}$ Monte Carlo samples with ACERMC and PYTHIA. The two samples are produced by varying PYTHIA's ISR and FSR parameters up and down together. The variations are in accordance with a previous ATLAS measurement of $t\bar{t}$ production which vetoed central jet activity not directly descended from the $t\bar{t}$ decay products [74].

6.9.1.4 Uncertainties on W+jets production

Four uncertainties are evaluated exclusively for the W+jets process: the normalization uncertainty, the uncertainty on the heavy flavor content of W+jets events, a scale uncertainty, and an uncertainty due to the matching scheme implemented in ALPGEN.

The W+jets normalization uncertainty is the uncertainty on the data-derived W+jets scale factors. In the muon channel these are 0.95 ± 0.15 (0.81 ± 0.13) for the resolved (boosted) selection. Scale factors of 0.89 ± 0.16 (0.65 ± 0.14) were computed in the resolved (boosted) electron channel. The derivation of these scale factors is explained in Section 6.7.1. The uncertainty on the data-derived mixture of W+light and W+heavy flavor partons is also taken into account.

Two shape uncertainties are evaluated by varying ALPGEN parameters in the W+jets Monte Carlo samples. First, the functional form of the factorization and renormalization scale in ALPGEN is varied by changing its "iqopt3" parameter. Second, the minimum p_T of an outgoing parton is changed to 10 GeV from its nominal value of 15 GeV. The samples generated using both of these variations are normalized to the nominal number of W+jets events calculated in the scale factor evaluation since the W+jets normalization is data-derived.

6.9.1.5 Uncertainties on other backgrounds

The other electroweak backgrounds are scaled by constant factors up and down to evaluate the uncertainty on their normalizations. The variations are ±48% for Z+jets, ±34% for dibosons, and ±7.7% for single top. These are the theoretical uncertainties on their respective production cross sections plus a conservative 25% uncertainty for each small-R jet not originating from a top quark or vector boson decay, averaged over all events.

The uncertainty on the multijet background is described in Section 6.7.2

6.9.2 Uncertainties affecting reconstructed objects

6.9.2.1 Jets

Jet calibration and reconstruction are the source of several systematic uncertainties. The jet energy scale uncertainty, the jet energy resolution uncertainty, and the uncertainty in jet reconstruction and jet vertex fraction efficiencies all affect the reconstruction of small-R jets. Large-R jets have uncertainties evaluated for their mass scale, energy scale, and $\sqrt{d_{12}}$.

The jet energy scale uncertainty for small-R jets takes into account the uncertainty in the LC+JES calibration due to the flavor composition of the jet, the calorimeter response of different quark flavors, effects due to other close by jets, pile-up, and the uncertainty in the energy scale of jets constraining b-quarks [51]. The contributions to this uncertainty from its various parts are shown in Figure 6.11.

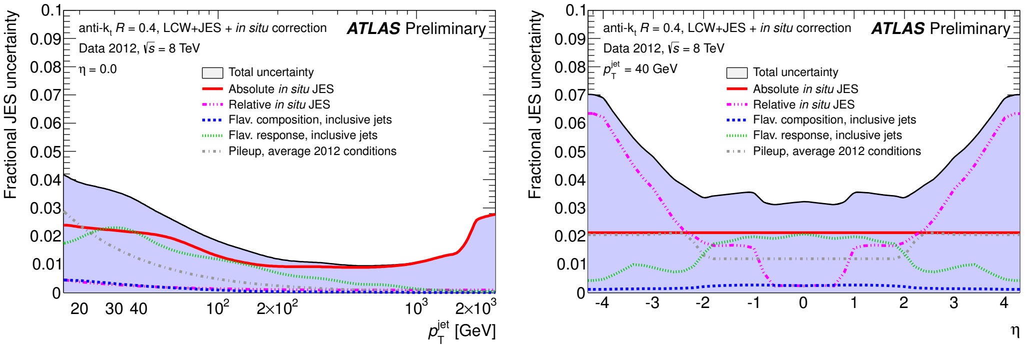

FIGURE 6.11: The jet energy scale uncertainties for small-R jets in ATLAS [75]. Example uncertainty components and total envelope are shown for jets at $\eta = 0$ over a range of transverse momenta (left) and for jets with $p_T = 40$ over a range of pseudorapidities (right).

The jet energy resolution in ATLAS is computed by measuring the energy difference of back-to-back jets. After taking into account other calorimeter deposits in the event, the resolution of the pair of jets is extracted by requiring that their transverse momenta be balanced. The jet energy resolution uncertainty is evaluated by smearing the energy of jets in the simulation by the uncertainty on the resolution measurement. The jet energy resolution can only be made worse in the simulation, so the effect of the smearing on the analysis is symmetrized.

The jet vertex fraction uncertainty is assessed using two methods. First, the efficiency of selecting jets from the hard scatter vertex and mistag rate of selecting jets from pile-up vertices are parameterized as a function of jet p_T using Z+jets events. The uncertainty on the fits is inflated as a conservative estimate of the systematic uncertainty. The selection of the Z+jets events is then varied to assess a second source of uncertainty in the measurement, and the uncertainties from the fits and the selection are combined in quadrature for the final systematic uncertainty.

The jet reconstruction efficiency uncertainty is assessed by randomly discarding jets from events. The probability of rejecting a jet ranges from 2 to 7% and is parameterized by the jet pseudorapidity. The effect of this uncertainty on the analysis was found to be negligible.

Systematic uncertainties for large-R jet mass and $\sqrt{d_{12}}$ are evaluated using the *in-situ* comparison of calorimeter and track jets [76]. Track and calorimeter jets within $\Delta R < 0.3$ of each other are matched, and the ratio of a variable X between a calorimeter jet and its corresponding track jet is defined as $r^{X}_{\text{track jet}}$. The double ratio of the variable X between data and Monte Carlo is defined as $R^{X}_{\text{track jet}} = r^{X,\text{data}}_{\text{track jet}}/r^{X,\text{MC}}_{\text{track jet}}$. Since the calorimeter and inner detector systematic uncertainties are largely uncorrelated, any deviation of $R^{X}_{\text{track jet}}$ is attributed to mismodeling in the simulation and is assessed as a systematic uncertainty accordingly. Figure 6.12 shows an example of the double ratio for large-R jet mass.

The jet energy scale uncertainty for the large-R jets uses the same methods as those defined for small-R jets.

6.9.2.2 Leptons

The reconstruction and identification of both muons and electrons are a source of uncertainty in this analysis. An uncertainty is assessed for their calibration using the Z boson peak. Efficiency scale factors are applied to Monte Carlo events to correct for the differences in efficiency observed in the data and Monte Carlo. The uncertainty due to these corrections must be taken into account. Scale factors are derived for trigger, identification, and isolation cuts on leptons. For a detailed description of the derivation of lepton scale factors and their associated uncertainties, see Section 7.2.2.

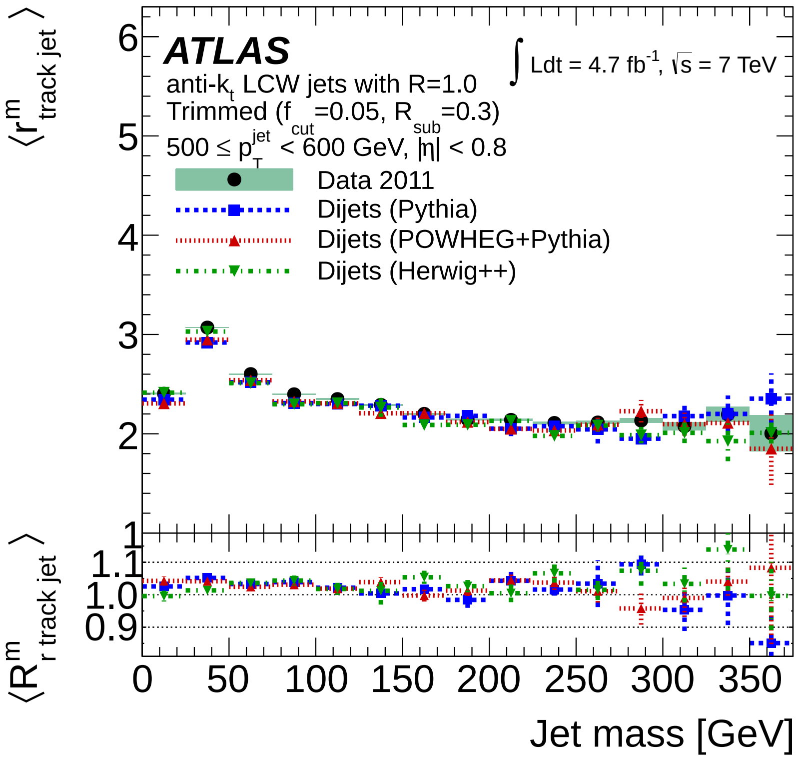

Figure 6.12: An example calorimeter to track jet ratio for *in-situ* jet mass uncertainty evaluation.

6.9.2.3 *Missing transverse momentum*

All energy scale and resolution uncertainties for objects included in the $E_{\mathrm{T}}^{\mathrm{miss}}$ reconstruction of an event are propagated into the $E_{\mathrm{T}}^{\mathrm{miss}}$ calculation—electrons, muons, and jets. In addition, the energy of the soft jets and clusters not associated with any identified object are varied based on parton shower tuning and detector modeling, and these variations are propagated into the $E_{\mathrm{T}}^{\mathrm{miss}}$.

6.9.3 *Summary of systematic uncertainties*

The systematics are evaluated separately in the resolved and boosted channels. Tables 6.3 and 6.4 summarize the effect of various systematic variations on the nominal SM background event yields and the event yield of a topcolor Z' boson with $m_{Z'} = 1.5$ TeV in the resolved and boosted channels, respectively.

Table 6.3: Summary of the effect of systematic variations on the SM background yield and that of a Z' boson with $m_{Z'} = 1.5$ TeV in the resolved channel. The variation is quoted as a percent variation from the nominal yield.

Systematic effect	tot	$t\bar{t}$	stop	Wjets	multi	Zjets	dbsn	Z'
Luminosity	2.9	3.6	3.6	0.0	0.0	3.6	3.6	3.6
ISR/FSR	0.2	0.2	0.0	0.0	0.0	0.0	0.0	0.0
PDF	2.9	2.9	5.1	3.0	0.0	4.4	2.0	4.6
$t\bar{t}$ norm	7.6	10.2	0.0	0.0	0.0	0.0	0.0	0.0
$t\bar{t}$ generator	1.5	2.0	0.0	0.0	0.0	0.0	0.0	0.0
W+jets norm	2.1	0.0	0.0	15.4	0.0	0.0	0.0	0.0
W shape ptjmin10	0.0	0.0	0.0	0.0	0.0	0.0	0.0	0.0
W shape iqopt3	0.0	0.0	0.0	0.0	0.0	0.0	0.0	0.0
W+jets $b\bar{b} + c\bar{c} + c$ vs. light	0.8	0.0	0.0	6.1	0.0	0.0	0.0	0.0
W+jets $b\bar{b}$+25%	0.2	0.0	0.0	1.7	0.0	0.0	0.0	0.0
W+jets c+25%	1.1	0.0	0.0	7.7	0.0	0.0	0.0	0.0
Multi-jets norm, e+jets	0.6	0.0	0.0	0.0	13.0	0.0	0.0	0.0
Multi-jets norm, μ+jets	1.8	0.0	0.0	0.0	37.0	0.0	0.0	0.0
JES0	5.7	4.9	7.7	11.1	0.0	12.0	11.4	2.1
JES1	2.0	1.7	3.0	3.6	0.0	5.6	4.2	0.7
BoostedJES0	0.3	0.3	0.1	0.2	0.0	0.2	0.1	3.6
BoostedJES1	0.0	0.0	0.0	0.0	0.0	0.0	0.0	2.0
BoostedJES2	0.0	0.0	0.0	0.0	0.0	0.1	0.0	0.1
JER0	1.6	0.2	2.4	8.2	0.0	11.1	9.2	0.2
JER1	0.2	0.1	0.1	0.4	0.0	3.1	0.4	0.3
JER2	0.0	0.0	0.0	0.1	0.0	0.1	0.0	0.1
Parton shower	4.5	6.1	0.0	0.0	0.0	0.0	0.0	0.0
Jet vertex fraction	1.7	1.7	1.7	2.6	0.0	2.6	2.2	2.3
c-tag	1.4	0.3	0.4	7.6	0.0	5.6	8.8	0.3
Mistag	0.7	0.2	0.3	4.0	0.0	4.6	3.3	0.3
b-tag	4.3	4.9	5.7	2.4	0.0	3.1	1.9	1.8
Electron scale factor	1.0	1.1	1.1	1.0	0.0	1.2	1.0	1.1
Muon scale factor	1.5	1.5	1.5	1.6	0.0	1.4	1.6	1.5
EW Sudakov	2.2	2.9	0.0	0.0	0.0	0.0	0.0	0.0
topmass	1.8	2.4	0.0	0.0	0.0	0.0	0.0	0.0

6.10 Results

The results of this analysis are assessed in two ways. First, the data are compared to the Standard Model background, and the compatibility of the data with the SM in the absence of any signal is evaluated. If no discrepancy is observed, upper cross section limits for the two signal benchmarks are computed and translated into excluded masses.

Figures 6.13 and 6.14 show the $t\bar{t}$ invariant mass distributions for data and the SM expectation in the resolved and boosted channels, respectively. Figure 6.15 shows the $m_{t\bar{t}}$ spectrum summed over all selection channels.

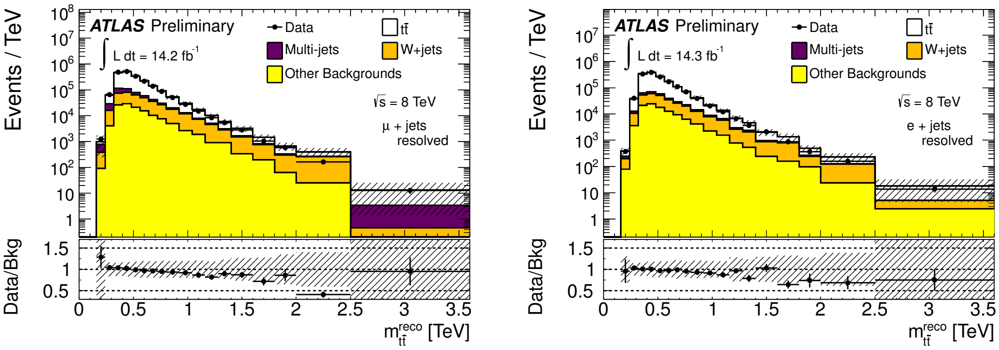

FIGURE 6.13: The $m_{t\bar{t}}$ distribution in data and background in the resolved muon (left) and electron (right) channels. The shaded area indicates the total uncertainty on the background prediction. The Poisson statistical uncertainty on the data is also shown. The right-most bin includes the contribution from overflow events.

6.10.1 Compatibility with the null hypothesis

After the $t\bar{t}$ invariant mass distribution has been constructed in the four selection channels, the data and simulation $m_{t\bar{t}}$ spectra are compared. `BumpHunter` [77] is used to perform this comparison systematically.

`BumpHunter` defines sliding windows of variable size (with a minimum width of 2 bins) and compares the data and predictions in each window. For each of the four

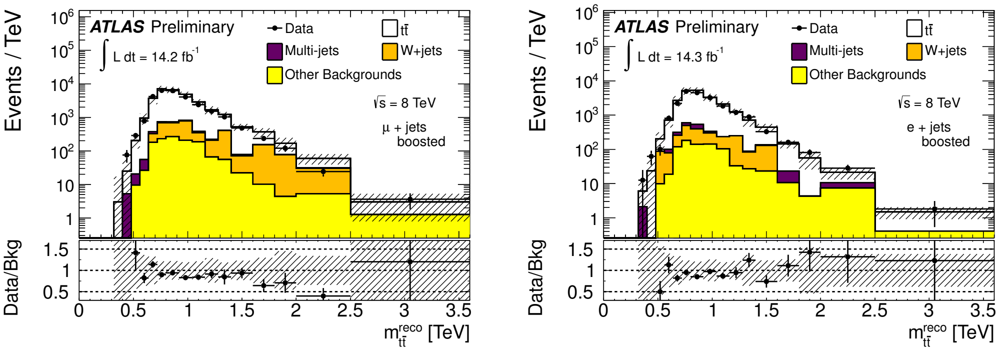

FIGURE 6.14: The $m_{t\bar{t}}$ distribution in data and background in the boosted muon (left) and electron (right) channels. The shaded area indicates the total uncertainty on the background prediction. The Poisson statistical uncertainty on the data is also shown. The right-most bin includes the contribution from overflow events.

channels, the Poisson probability of the most significant bump or dip is recorded. In a particular window i, the Poisson probability is given by

$$P(d_i, b_i) = \begin{cases} \Gamma(d_i, b_i) = \sum_{(n=d_i)}^{\infty} \frac{b_i^n}{n!} e^{-b_i} & \text{if } d_i \geq b_i \\ 1 - \Gamma(d_i + 1, b_i) & \text{if } d_i < b_i \end{cases} \tag{6.12}$$

where d_i and b_i are the data and background counts in the window i. This equation is valid when looking for an excess in the data; deficits are searched for by reversing the inequalities. The smallest Poisson probability from all the windows is recorded as P_i^{min}, and the `BumpHunter` test statistic, t, is defined in terms of it:

$$t = \begin{cases} 0 & \text{if } d_i \leq b_i \\ -\log P_i^{min} & \text{otherwise.} \end{cases} \tag{6.13}$$

10,000 pseudoexperiments are generated, where pseudodata are produced by sampling Poisson fluctuations of the background prediction. The p-value of the most significant bump is calculated by comparing the test statistic from the data with the

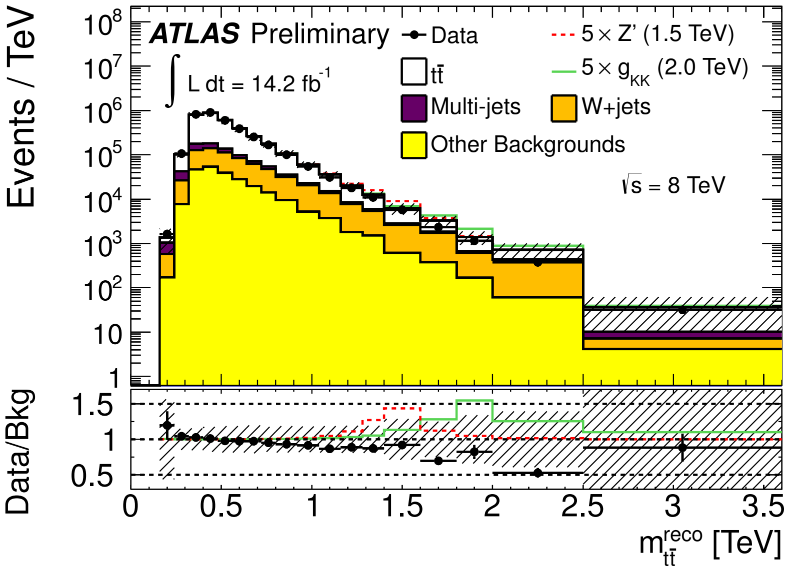

FIGURE 6.15: The $m_{t\bar{t}}$ distribution in data and background summed over all channels. The shaded area indicates the total uncertainty on the background prediction. The Poisson statistical uncertainty on the data is also shown. Two $m_{t\bar{t}}$ spectrum from signal benchmarks is added to the background prediction to show the effect on the total invariant mass distribution. The right-most bin includes the contribution from overflow events.

test statistics calculated from the pseudoexperiments.

$$p\text{−value} = \frac{\int_{t_{obs}}^{\infty} f(t)}{\int_{0}^{\infty} f(t)} \tag{6.14}$$

Here t_{obs} is the test statistic observed in the most interesting window and $f(t)$ is the distribution of test statistics found in the pseudodata. p-values close to one signify agreement between the data and prediction.

`BumpHunter` combines the four selection channels in two ways: by simply summing the $m_{t\bar{t}}$ spectra from each channel or by scanning all four simultaneously. If there is overlap between the most significant excesses or deficits in more than one channel, the test statistic is calculated with the combined probability of the excesses or deficits in the overlapping channels.

Table 6.5 summarize the most significant excesses and deficits in each channel, with all channels summed, and with the channels scanned simultaneously (combined) using only statistical uncertainties. Table 6.6 is equivalent, except that systematic uncertainties are also taken into account.

6.10.2 Upper cross section times branching ratio limits for $t\bar{t}$ resonances

With no significant excess in the data over the Standard model background prediction, upper limits on the production cross section times branching fraction are set. This is accomplished following the procedure laid out by the D0 Collaboration [78]. The likelihood L_ν for a resonance mass ν with cross section σ_ν is the product of the Poisson probabilities of the data measurement given an expectation of the signal plus background in each bin:

$$L_\nu(D|\sigma_\nu, a_\nu, b) = \prod_{i=1}^{N} \frac{e^{-(a_{\nu,i}\sigma_\nu + b_i)}(a_{\nu,i}\sigma_\nu + b_i)^{D_i}}{\Gamma(D_i + 1)}, \tag{6.15}$$

where the product is over all bins, i; D_i and b_i are the number of data events and the total predicted background yield in bin i, respectively; and a_ν is the acceptance times luminosity for the signal.

A Gaussian prior is used for systematic variations unless the relative variation exceeds 20%; in that case a log-normal distribution is used to prevent negative background expectations. Systematic uncertainties are included in the cross section upper limit calculation by randomly sampling each prior to produce a shifted background prediction. The signal cross section prior is flat and zero for negative cross sections; the 95% credibility level of the cross section is calculated by integrating the posterior probability to 95%.

Upper cross section limits as a function of the topcolor Z' and RS KK gluon masses are shown in Tables 6.7 and 6.8, respectively. Figure 6.8 illustrates these results.

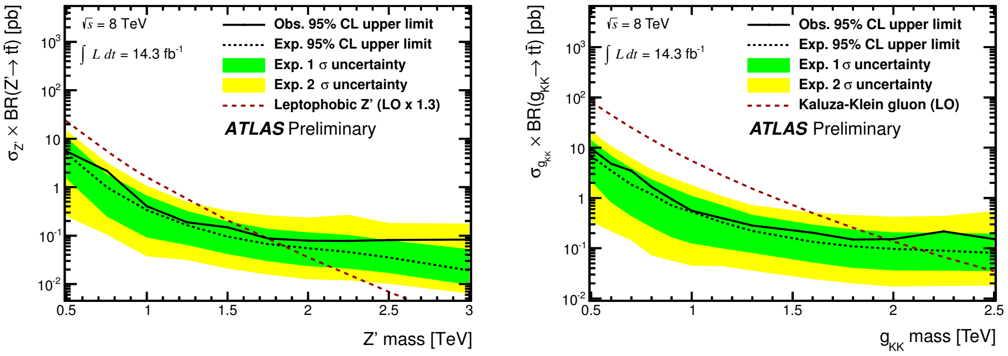

FIGURE 6.16: The observed and expected upper limits on the cross section times branching ratio of a topcolor Z' boson (left) and RS KK gluon (right) decaying to $t\bar{t}$. The dashed and solid black lines are the expected and observed upper limits, and the green and filled areas denote the 1 and 2σ uncertainty bands on the expected limit.

6.11 Conclusions

A search for the resonant production of $t\bar{t}$ pairs in proton-proton collisions at $\sqrt{s} = 8$ TeV was performed with the ATLAS detector with 14.3 fb^{-1} of integrated luminosity. No significant deviations from the Standard Model predictions were observed in the $m_{t\bar{t}}$ spectrum. In light of this, upper limits on the cross section times branching ratio of two benchmark models, the topcolor Z' boson and the Randall-Sundrum Kaluza-Klein gluon, were set at the 95% credibility level. The narrow topcolor Z' is excluded in the mass range 0.5 TeV $< m_{Z'} < 1.8$ TeV, and the RS g_{KK} is excluded in the range 0.5 TeV $< m_{g_{KK}} < 2.0$ TeV at the 95% credibility level.

Table 6.4: Summary of the effect of systematic variations on the SM background yield and that of a topcolor Z' boson with $m_{Z'} = 1.5$ TeV in the boosted channel. The variation is quoted as a percent variation from the nominal yield.

Systematic effect	tot	$t\bar{t}$	stop	Wjets	multi	Zjets	dbsn	Z'
Luminosity	3.3	3.6	3.6	0.0	0.0	3.6	3.6	3.6
ISR/FSR	0.7	0.8	0.0	0.0	0.0	0.0	0.0	0.0
PDF	5.8	5.8	7.2	6.3	0.0	8.7	6.6	2.9
$t\bar{t}$ norm	8.8	10.2	0.0	0.0	0.0	0.0	0.0	0.0
$t\bar{t}$ generator	1.6	1.9	0.0	0.0	0.0	0.0	0.0	0.0
W+jets norm	1.0	0.0	0.0	12.2	0.0	0.0	0.0	0.0
W shape ptjmin10	0.0	0.0	0.0	0.0	0.0	0.0	0.0	0.0
W shape iqopt3	0.0	0.0	0.0	0.0	0.0	0.0	0.0	0.0
W+jets $b\bar{b} + c\bar{c} + c$ vs. light	1.0	0.0	0.0	12.4	0.0	0.0	0.0	0.0
W+jets $b\bar{b}$+25%	0.4	0.0	0.0	5.2	0.0	0.0	0.0	0.0
W+jets c+25%	0.6	0.0	0.0	7.1	0.0	0.0	0.0	0.0
Multi-jets norm, e+jets	0.3	0.0	0.0	0.0	27.5	0.0	0.0	0.0
Multi-jets norm, μ+jets	0.3	0.0	0.0	0.0	22.5	0.0	0.0	0.0
JES0	0.7	0.6	1.5	1.3	0.0	3.0	0.9	0.5
JES1	0.2	0.4	0.5	0.6	0.0	2.5	3.9	0.2
BoostedJES0	16.4	16.8	16.7	13.9	0.0	16.6	32.8	2.9
BoostedJES1	0.5	0.4	0.6	0.9	0.0	0.0	0.0	1.6
BoostedJES2	0.1	0.1	0.1	0.0	0.0	6.3	0.0	0.1
JER0	0.6	0.2	2.0	9.4	0.0	10.6	13.3	0.6
JER1	0.1	0.2	0.0	0.3	0.0	6.1	0.0	0.1
JER2	0.1	0.1	1.5	0.9	0.0	1.9	9.0	0.2
Parton shower	4.1	4.7	0.0	0.0	0.0	0.0	0.0	0.0
Jet vertex fraction	2.1	2.1	2.1	2.0	0.0	2.7	2.1	2.4
c-tag	0.7	0.2	0.1	6.3	0.0	0.4	10.4	0.9
Mistag	0.7	0.2	0.0	6.0	0.0	0.1	2.1	0.1
b-tag	3.4	3.4	2.8	4.3	0.0	0.8	0.7	5.9
Electron scale factor	1.0	1.0	1.0	0.8	0.0	0.8	1.4	1.0
Muon scale factor	1.6	1.6	1.6	1.7	0.0	1.7	1.2	1.6
EW Sudakov	4.4	5.1	0.0	0.0	0.0	0.0	0.0	0.0
topmass	1.3	1.5	0.0	0.0	0.0	0.0	0.0	0.0

Table 6.5: The most significant deviations found in the $t\bar{t}$ mass spectra. Only statistical uncertainties are considered.

Excesses			
Channel	p-value	σ	mass range
e-resolved	0.0002 ± 0.0000	3.5827	240 – 480
μ-resolved	0.0000 ± 0.0000	> 5	240 – 480
e-boosted	0.1657 ± 0.0012	0.9715	1160 – 1400
μ-boosted	0.0023 ± 0.0002	2.8352	400 – 720
all added	0.0000 ± 0.0000	> 5	240 – 480
combined	1.0000 ± 0.0000	No Excess	0 – 0

Deficits			
Channel	p-value	σ	mass range (GeV)
e-resolved	0.0000 ± 0.0000	> 5	800 – 1800
μ-resolved	0.0000 ± 0.0000	> 5	2000 – 3600
e-boosted	0.7772 ± 0.0013	No Deficit	640 – 920
μ-boosted	0.0012 ± 0.0001	3.0307	1600 – 2500
all added	0.0000 ± 0.0000	> 5	920 – 1160
combined	1.0000 ± 0.0000	No Deficit	0 – 0

Table 6.6: The most significant deviations found in the $t\bar{t}$ mass spectra. Systematic and statistical uncertainties are considered.

Excesses			
Channel	p-value	σ	mass range (GeV)
e-resolved	0.0682 ± 0.0025	1.4893	240 – 400
μ-resolved	0.0154 ± 0.0012	2.1596	240 – 400
e-boosted	0.6715 ± 0.0047	No Excess	1800 – 2500
μ-boosted	0.8570 ± 0.0035	No Excess	400 – 560
all added	0.0266 ± 0.0016	1.9333	240 – 400
combined	1.0000 ± 0.0000	No Excess	0 – 0

Deficits			
Channel	p-value	σ	mass range (GeV)
e-resolved	0.7065 ± 0.0046	No Deficit	1600 – 2000
μ-resolved	0.9976 ± 0.0005	No Deficit	2000 – 3600
e-boosted	0.3868 ± 0.0049	0.2877	1400 – 1800
μ-boosted	0.8756 ± 0.0033	No Deficit	2000 – 3600
all added	0.7572 ± 0.0043	No Deficit	1600 – 2500
combined	1.0000 ± 0.0000	No Deficit	0 – 0

Table 6.7: Upper cross section times branching ratio limits at the 95% credibility level for a topcolor Z' decaying to $t\bar{t}$ using the combination of all channels. The observed and expected limits as well as the $\pm 1\sigma$ variation of the expected limit are shown for each resonance mass. The second column gives the theoretical predictions.

Mass (TeV)	$\sigma\times$ BR $\times 1.3$ [pb]	Obs. (pb)	Exp. (pb)	-1σ (pb)	$+1\sigma$ (pb)
0.50	23.	5.30	4.99	1.50	10.7
0.75	5.6	2.17	1.00	0.249	1.87
1.00	1.6	0.406	0.335	0.091	0.674
1.25	0.57	0.187	0.160	0.064	0.323
1.50	2.1×10^{-1}	0.148	0.096	0.041	0.198
2.00	3.9×10^{-2}	0.078	0.055	0.023	0.117
2.50	6.9×10^{-3}	0.081	0.035	0.017	0.081
3.00	1.5×10^{-3}	0.083	0.019	0.010	0.053

.

Table 6.8: Upper cross section times branching ratio limits at the 95% credibility level for an RS KK gluon decaying to $t\bar{t}$ using the combination of all channels. The observed and expected limits as well as the $\pm1\sigma$ variation of the expected limit are shown for each resonance mass. The second column gives the theoretical predictions.

Mass (TeV)	$\sigma\times$ BR [pb]	Obs. (pb)	Exp. (pb)	-1σ (pb)	$+1\sigma$ (pb)
0.50	82.	9.62	6.73	2.15	14.1
0.60	45.	4.79	3.48	0.813	6.98
0.70	25.	3.48	1.84	0.436	3.90
0.80	15.	1.66	1.19	0.262	2.37
0.90	8.8	0.948	0.711	0.165	1.60
1.00	5.5	0.561	0.529	0.125	1.11
1.15	2.8	0.394	0.329	0.100	0.720
1.30	1.5	0.282	0.221	0.081	0.464
1.60	0.50	0.204	0.134	0.052	0.296
1.80	0.26	0.149	0.109	0.041	0.237
2.00	0.14	0.153	0.097	0.036	0.209
2.25	0.067	0.218	0.089	0.036	0.203
2.50	0.035	0.152	0.080	0.035	0.196

7

Improved Reconstruction Methods for High-p_T Top Quark Decays with Electrons

The success of searches for high-mass exotic resonances decaying to $t\bar{t}$ pairs is strongly dependent on the reconstruction performance of high-p_T top quarks. The ΔR separation between the two-body decay products of a particle, a, is approximately given by

$$\Delta R_{decay} \approx \frac{2m^a}{p_T^a}. \tag{7.1}$$

Figure 7.1 shows the ΔR distance between the W boson and b quark from the decay of a top quark as a function of its p_T, illustrating this dependence.

For high-p_T top quark decays in which the W boson decays to a lepton and neutrino, the b quark and lepton are often very close to each other in $\eta - \phi$ space. Figure 7.2 illustrates the minimum $\Delta R(e,\ jet)$ separation in $t\bar{t}$ decays as a function of the invariant mass of the $t\bar{t}$ system.

The proximity of these particles poses two significant complications for the successful reconstruction of the lepton and b quark jet.

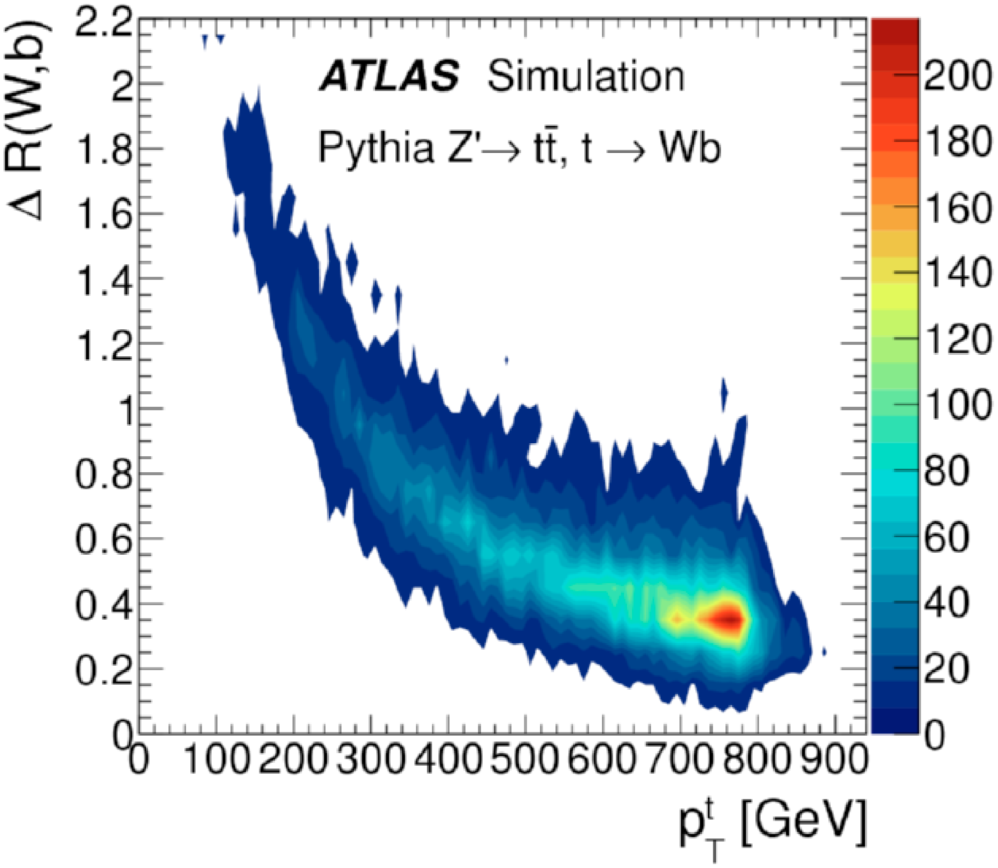

FIGURE 7.1: The ΔR separation between the top quark's decay products as a function of its p_T.

First, high-p_T particles originating from the b quark's parton shower interfere with the lepton isolation requirement. In order to reduce backgrounds from light quark jets, standard lepton isolation techniques construct a ring in $\eta - \phi$ space, usually of radius $R = 0.2$ or 0.3, surrounding the lepton candidate. The transverse momenta of all tracks or calorimeter deposits in the cone defined by that ring are summed, and if the p_T sum in the cone is greater than some threshold, the corresponding lepton is not selected. Track- and calorimeter-based algorithms are called `ptcone` and `etcone` isolation, respectively (`etcone` isolation with a cone size of 0.2 is often denoted `etcone`20). Higher thresholds are more efficient but reject fewer non-prompt

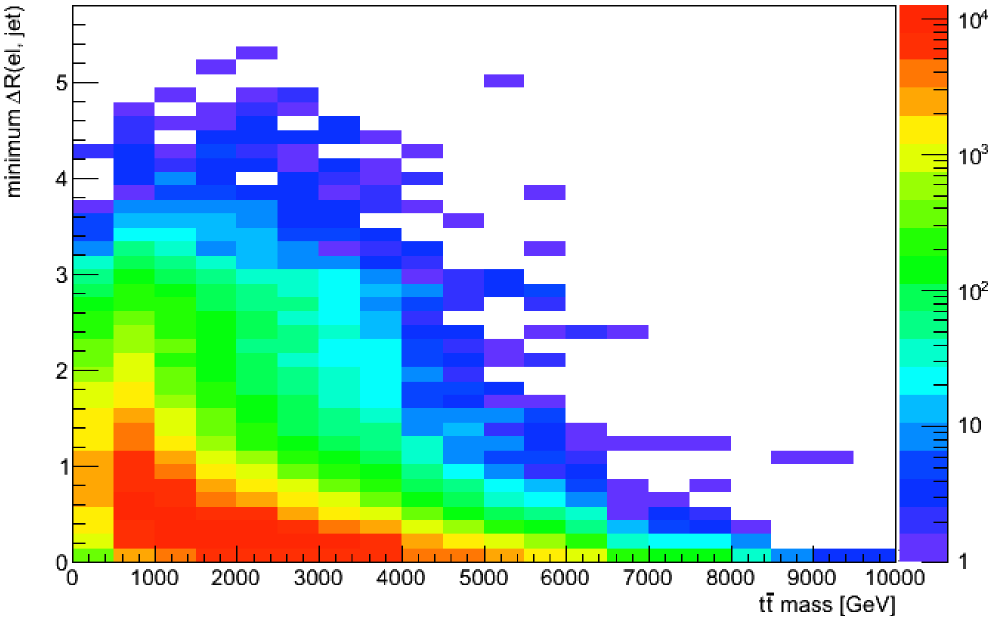

FIGURE 7.2: The $\Delta R(el,\ jet)$ separation for $t\bar{t}$ decays as a function of the $t\bar{t}$ invariant mass. Events were generated using PYTHIA 8.1. Jets were clustered from stable electrons, photons, and hadrons at truth-level using FastJet [79].

leptons. Likewise, smaller cone sizes accept more of both prompt and non-prompt leptons. The choice of the threshold value and cone size is therefore determined by the efficiency and background rejection needs of a particular analysis. Most analyses at ATLAS which study collisions producing $t\bar{t}$ pairs use a combination of `ptcone`20 and `etcone`20 isolation, each at approximately 90% efficiency for prompt leptons.

For high-p_T top quark decays, isolation algorithms with a fixed cone size become inefficient due to the nearness of the lepton to b quark decay products. Mini-isolation [80], which scales the isolation cone radius with $1/p_T^{lepton}$, was introduced to mitigate this effect. The commissioning, optimization, and performance of electron mini-isolation at ATLAS are discussed in Section 7.2.

Second, since topological clusters in the EM calorimeter are passed to jet reconstruction algorithms, the energy deposited by electrons will be included in the four-momenta of jets in the event. This is often the desired result. In the semileptonic decay of a B hadron, for instance, the electron carries some of the energy of the initial b quark. If the jet is used to represent the four-momentum of the b quark, the electron's energy deposits ought to be included in the jet for an accurate representation. However, for analyses which use the four-momenta of both prompt electrons and jets for event selection and reconstruction, this can lead to double counting of the electron energy. Such is the case for $t\bar{t}$ resonance searches, in which electron and jet four-momenta are summed to calculate the invariant mass of the $t\bar{t}$ system.

An electron-jet overlap removal procedure must be devised to cope with this issue. The standard overlap removal implemented in most $t\bar{t}$ analyses defines two distances in $\eta - \phi$ space: R_1 and R_2 with $R_1 < R_2$. Electrons and jets reconstructed within $\Delta R(e,\ jet) < R_1$ of each other are considered to represent the same object, namely the electron, and the jet is removed from the event; if more than one jet is within this distance to the electron, only the closest jet is removed. If they are separated by an intermediate distance, $R_1 < \Delta R(e,\ jet) < R_2$, then the electron is considered a jet constituent and is not selected. Electrons and jets separated by more than R_2 are treated as distinct objects and do not undergo overlap removal. For analyses targeting the $t\bar{t}$ final state using anti-k_t jets with $R = 0.4$, R_1 and R_2 are defined as 0.2 and 0.4, respectively.

However, this procedure becomes inefficient at high-p_T for top quarks in the electron decay mode because the electron and b quark are often within $\Delta R < 0.4$ of each other. Their calorimeter energy deposits are consequently included in one jet, representing the sum of their four-momenta. During overlap removal, either the jet or the electron is removed from the event. With one of the top quark decay products discarded, it is not possible to correctly reconstruct the event, leading either to event selection inefficiency or a mis-reconstructed $t\bar{t}$ system.

A new electron jet overlap removal procedure was developed by the author specifically for the boosted top quark topology in the electron decay mode. Details of this procedure are discussed in Section 7.3

The work presented in this chapter was performed entirely by the author unless otherwise noted.

7.1 Tag-and-probe techniques

In order to study the performance of prompt electron reconstruction and identification in collision event data, it is first necessary to obtain a pure sample of prompt electrons. One method for achieving this is known as the "tag-and-probe" technique.

Events are first "tagged" as likely to contain prompt electrons. This is accomplished by identifying and selecting a set of objects, one of which is an electron, that is expected to be produced through a well known physical process. This process should have a relatively small background of non-prompt electrons after the tag selection is imposed. Once the event has been tagged, the electrons in question can be studied—or "probed"—with the knowledge that they are likely prompt. Any remaining background contribution should be accounted for in the measurement performed.

Applying the tag-and-probe technique to $Z \to \ell\ell$ events (Z tag-and-probe) is the most common method for studying lepton reconstruction and identification [46]. It is introduced in Section 7.1.1. A novel approach, developed by the author, to evaluating the systematic uncertainty of Z tag-and-probe results uses $t\bar{t} \to b\bar{b}\ e\mu\nu\nu$ events to obtain a pure prompt electron sample ($t\bar{t}$ tag-and-probe). It is presented in Section 7.1.2.

7.1.1 Z tag-and-probe

$Z \to ee$ events are used to study electron identification and isolation efficiencies in the studies presented in this chapter. To select a pure sample of prompt electrons

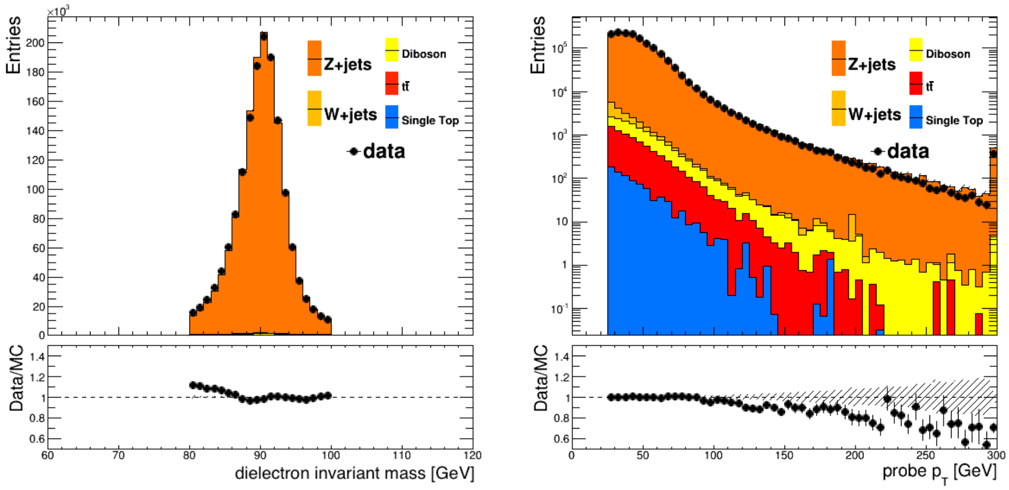

FIGURE 7.3: Example of the purity of probes obtained using the Z tag-and-probe technique for electrons in $\sqrt{s} = 8$ TeV data and MC. The dielectron mass of the tag-probe system (left) and the probe p_T (right) distributions are shown. The lower panels show the event yield ratio between data and the MC prediction in each bin. All labeled backgrounds are present in both plots, but their contribution is too small to see on a linear scale. A log scale on the y-axis is used in the right-hand plot in order to show the contribution of the non-prompt electrons from the W+jets background. Here, the tag electron is required to pass `tight++` identification and be mini-isolated, the probe electron is an EM cluster matched to track with no identification requirements, and their combined invariant mass must fall in the range 80 GeV $< m_{ee} <$ 100 GeV.

from $Z \rightarrow ee$ events, a tag electron with stringent identification requirements is selected. It is also required to fire the trigger. The invariant mass of the combined four-momentum of the tag and probe electrons must be near the pole mass of the Z boson, and they must be oppositely charged. These requirements alone yield a very pure sample of prompt probe electrons which can be studied.

The dominant background after these selection criteria is W+jets production, in which the prompt electron from the W boson is generally tagged, and the probe "electrons" are either misidentified light jets or heavy flavor decay products. Figure 7.3 illustrates the purity of prompt electrons obtained through an example tag-and-probe selection.

7.1.2 $t\bar{t}$ tag-and-probe

There is an important topological difference between $Z \to ee$ and $t\bar{t}$ events. $t\bar{t}$ events generally produce at least two high-p_T (i.e. $p_T > 25$ GeV) jets from the b quarks of the top decays, while the average number of high-p_T jets in $Z \to ee$ events is less than one. A distinct tag-and-probe technique was developed by the author in order to assess the uncertainty on electron isolation efficiencies due to this difference in topology. That study is presented in Section 7.2.

The $t\bar{t} \to b\bar{b}\ e\mu\nu\nu$ decay mode is used for two reasons: the presence of two leptons greatly reduces contamination from QCD processes, and requiring one electron and one muon does the same for Drell-Yan production of same-flavor leptons. Events are tagged by requiring an isolated muon, which the event is triggered on, and two b-tagged jets at the 80% efficiency working point. After these requirements, the primary background comes from $t\bar{t} \to b\bar{b}\ qq\ \mu\nu$ events, with the electron candidates originating from semileptonic b quark decays.

7.2 Electron mini-isolation

Due to the inefficiency of standard lepton isolation techniques for high-p_T top quark decays, mini-isolation [80] was introduced to the $t\bar{t}$ resonances analysis. The mini-isolation of a lepton is defined as

$$I^{\ell}_{mini} = \sum_{tracks} p_T^{track} \qquad \text{with } \Delta R(\ell, track) < 10 \text{ GeV}/p_T^{\ell}, \tag{7.2}$$

where the sum is over all tracks with $p_T > 1$ GeV except that of the lepton. Since the isolation cone size falls like $1/p_T^{\ell}$, this isolation definition allows the lepton to be accepted even if there is significant nearby hadronic activity, so long as it is energetic enough. Although the $\Delta R(\ell, b)$ separation in top quark decays falls like $1/p_T^{top}$, the lepton p_T is used as a proxy for p_T^{top} in this analysis.

The best results were achieved when a threshold was imposed on the relative mini-isolation of the lepton, $I^{\ell}_{mini}/p^{\ell}_{T}$. A comparison of isolation performance follows.

7.2.1 Mini-isolation performance

In order to gauge the performance of mini-isolation for the $t\bar{t}$ resonances analysis, a comparison is made between it and several other isolation algorithms. This is done by scanning threshold cuts for each algorithm and measuring the signal efficiency and the background fake rate at each threshold value.

For the signal efficiency calculation, all signal region selection cuts are applied to the event except the electron isolation. The number of events passing all but the electron isolation cut is the denominator of the efficiency measurement. The numerator is the event yield after imposing the electron isolation cut.

The background fake rate is measured in a control region enriched with non-prompt electrons. This is achieved by selecting events with exactly one electron, no muons, and inverted missing transverse energy cut and transverse mass cuts of $m_T < 30$ GeV and $E_{\mathrm{T}}^{\mathrm{miss}} < 30$ GeV. Once again, the denominator of the fake rate is the number of events passing all selection cuts except the electron isolation, and the numerator is the number of events also fulfilling the electron isolation requirement. The contribution of events with prompt electrons (from W+jets, Z+jets, $t\bar{t}$, or diboson production) passing these selection criteria is removed by subtracting the expected event yields given by Monte Carlo predictions.

Figures 7.4 and 7.5 compare the performance of various isolation definitions using the efficiency and fake rate. Operating points closer to the upper left corner are preferred since they yield a high signal efficiency at a given background fake rate. The relative mini-isolation achieves a high signal efficiency of 98% or above across a wide range of background fake rates. A cut of $I^{\ell}_{mini}/p^{\ell}_{T} < 0.05$, corresponding to a 99% efficiency for a 2 TeV Z' boson and 22% background fake rate, was chosen.

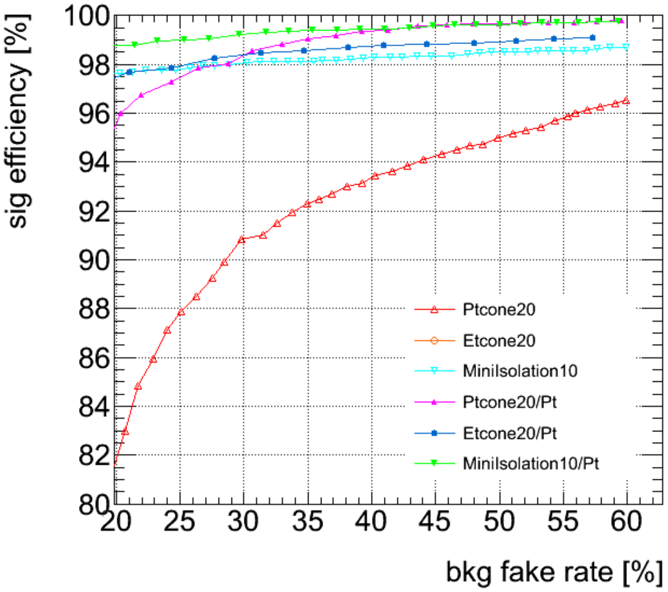

FIGURE 7.4: The signal efficiency as a function of background fake rate for electrons with various isolation definitions. A 2.0 TeV $Z'_{topcolor}$ benchmark is used for the signal efficiency calculation. Points closer to the upper left corner are preferred since they yield a high signal efficiency at a given background fake rate. The `etcone20` isolation has a signal efficiency below 80% for all background fake rates shown. From personal correspondence with Jiahang Zhong.

7.2.2 Data/MC scale factors

It is possible that mismodeling in the simulation causes the electron isolation cut efficiency to be different in the MC prediction than that in the data. Each Monte Carlo event in which an electron passes the isolation cut is given a weight, called a scale factor (SF), that compensates for this effect. Electron efficiency scale factors are derived on an electron-by-electron basis and are parameterized in terms of the electron p_T and η to account for any kinematic dependence of the mismodeling.

The nominal electron isolation efficiency is measured in data using the Z tag-and-probe technique introduced in Section 7.1.1. Events are considered $Z \to ee$ candidates if they fulfill the following criteria:

- there are exactly two oppositely charged electrons with $p_T > 25$ GeV;

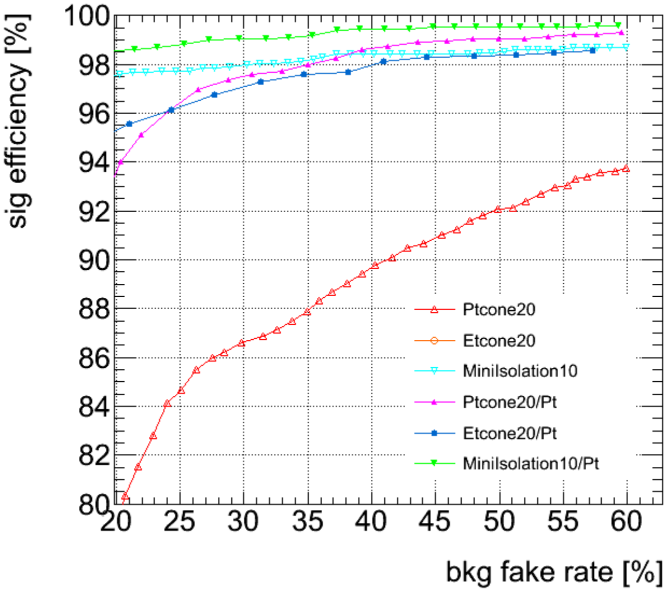

FIGURE 7.5: The signal efficiency as a function of background fake rate for electrons with various isolation definitions. A 3.0 TeV $Z'_{topcolor}$ benchmark is used for the signal efficiency calculation. Points closer to the upper left corner are preferred since they yield a high signal efficiency at a given background fake rate. The `etcone`20 isolation has a signal efficiency below 80% for all background fake rates shown. The author prepared inputs for this figure.

- one electron (the tag) must fire the trigger, pass `tight++` ID requirements, and have relative mini-isolation < 0.05;
- the second electron (the probe) must pass the `tight++` ID requirements;
- the invariant mass of the dielectron system must be within 80 GeV $< m_{ee} <$ 100 GeV.

The same selection is applied to Monte Carlo events.

The denominator of the efficiency measurement is the number of probes passing the `tight++` identification criteria. The numerator is the number which also fulfill the relative mini-isolation requirement. Figure 7.6 shows the efficiency of the relative mini-isolation cut in data and MC as a function of p_T and η. Figure 7.7 shows the resulting scale factor.

No significant η dependence was found in the scale factors, so they are only applied as a function of the electron p_T.

7.2.3 Scale factor uncertainties

Three sources of systematic uncertainty are considered in the scale factor calculation: variations due to the tag selection, the invariant mass window, and the difference in topology between $Z \to ee$ and $t\bar{t}$ events. To assess the effect of the tag selection on the scale factors, the isolation of the tag electron is removed and the scale factors rederived; the difference in the scale factors is taken as a systematic uncertainty. The invariant mass window is also enlarged to 75 GeV $< m_{ee} <$ 105 GeV, and the scale factors recalculated. The scale factor uncertainty due to these variations are on the order of 0.1%.

The difference in topology is a more challenging effect to assess. The $t\bar{t}$ tag-and-probe technique introduced in Section 7.1.2 is used to obtain a pure sample of $t\bar{t} \to b\bar{b}\ e\mu\nu\nu$ events. The effect of the non-prompt background was deemed to be negligible and is ignored in the scale factor derivation. Figure 7.8 shows the electron probe p_T spectrum for both the numerator and denominator of the efficiency calculation as well as the purity of the electron sample.

The electron mini-isolation efficiency is derived in p_T bins in both the data and MC, and the resulting scale factor difference between this SF calculation and that of the nominal scale factor from the Z tag-and-probe selection is taken as a systematic uncertainty. The derived scale factors and corresponding uncertainties are summarized in Table 7.1. The scale factors found are consistent with unity when the uncertainty due to the difference in event topology is taken into account.

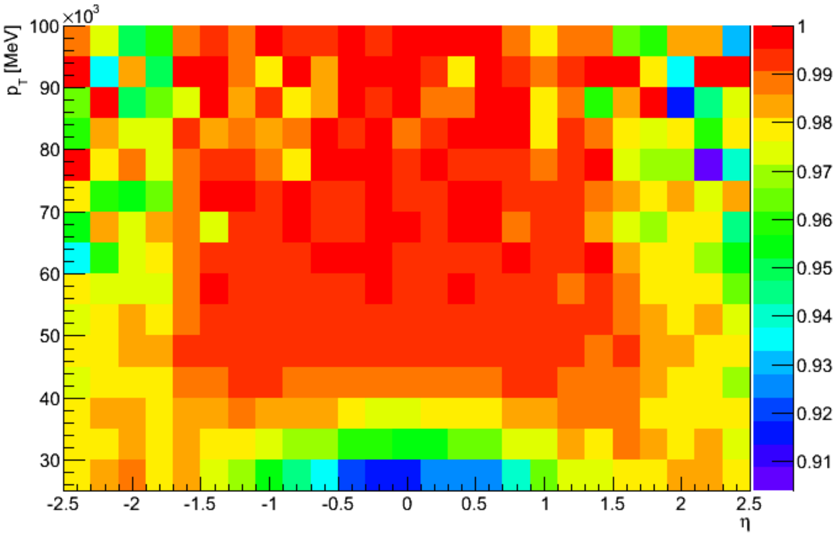

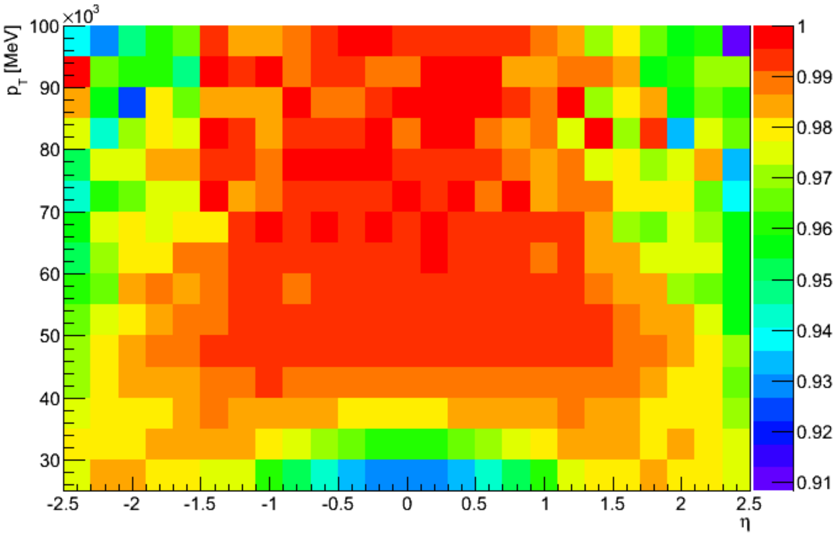

FIGURE 7.6: The efficiency of the relative mini-isolation requirement applied to probe electrons in data (top) and MC (bottom) parameterized by the probe η and p_T.

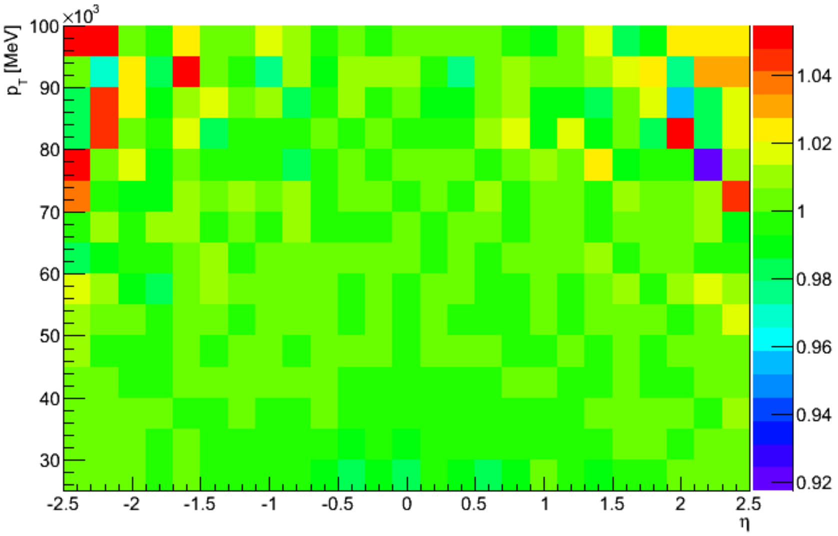

FIGURE 7.7: The derived data/MC scale factor of the relative mini-isolation cut applied to probe electrons as a function of η and p_T.

7.3 Improved electron-jet overlap removal

This section presents the electron-jet overlap removal procedure developed by the author for the single lepton $t\bar{t}$ resonances search. It is motivated by the difference in efficiency in the single lepton $t\bar{t}$ resonance search between the electron and muon channels at high invariant mass shown in Figure 6.2. The improvement over the standard overlap procedure used in $t\bar{t}$ analyses is significant. For 2.25, 2.5, and 3.0 TeV $Z'_{topcolor}$ resonances decaying to $t\bar{t}$ pairs, the selection efficiency in the boosted electron channel increases by 29, 33, and 51%, respectively.

The work discussed in this section was not included in the 14.3 fb^{-1} 8 TeV $t\bar{t}$ resonances result presented in Chapter 6. However, it is part of an improved analysis of the full 2012 8 TeV dataset which is in the later stages of approval within the ATLAS collaboration. A publication of the improved results is expected in the fall of 2014.

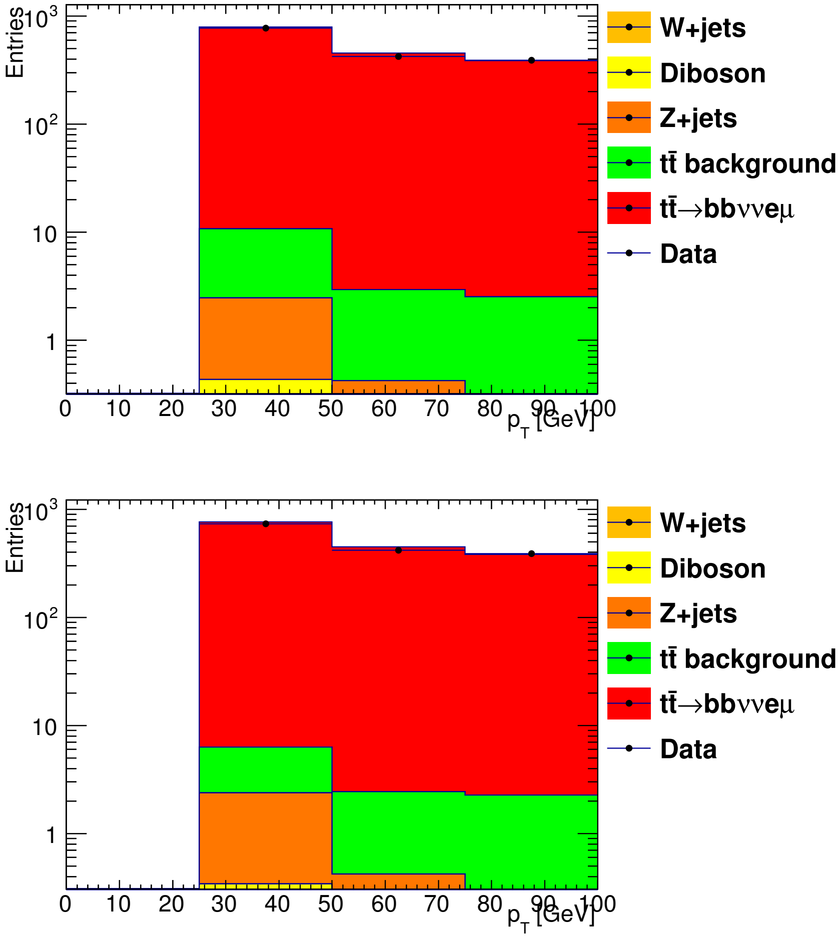

FIGURE 7.8: The probe p_T spectrum in $t\bar{t}$ tag-and-probe events before the mini-isolation requirement (top) and after (bottom) in data and MC. Note that a log scale is used for the y-axis in order to illustrate the contamination of the non-prompt background (green).

7.3.1 Electron-jet overlap removal procedure

The improved electron-jet overlap removal procedure attempts to separate electrons and b quark decay products that have been clustered into one jet. This is achieved by first identifying the electron and subsequently subtracting its four-momentum from the nearest jet (if any) that is within $\Delta R(e,\ jet) < 0.4$. If the electron and jet both originate from an electron, this subtraction will yield a subtracted jet with very little

Table 7.1: Summary of the mini-isolation scale factors and corresponding uncertainties derived for the $t\bar{t}$ resonances search. Here, the Z uncertainty denotes the statistical and systematic uncertainties from the Z tag-and-probe scale factor derivation described in Section 7.2.3. The $t\bar{t}$ uncertainty is the absolute value of the difference between the scale factor derived using the $t\bar{t}$ tag-and-probe selection and the nominal scale factor.

p_T range [GeV]	scale factor	Z uncertainty	$t\bar{t}$ uncertainty
$25 - 30$	0.9932	0.0008	0.004
$30 - 35$	0.9974	0.0005	0.009
$35 - 40$	0.9992	0.0003	0.011
$40 - 45$	0.9998	0.0002	0.012
$45 - 50$	1.0011	0.0002	0.014
$50 - 75$	1.0014	0.0003	0.018
$75 - 100$	1.0023	0.0011	0.018
> 100	1.0039	0.0018	0.005

transverse momentum. A p_T cut of 25 GeV is applied to the subtracted jet four-momenta to deal with such cases. Similarly, if both the electron and jet originate from hadronic decays, the two objects are likely to remain close to each other in $\eta - \phi$ space. This is taken into account by requiring the electron and jet to be separated by at least $\Delta R(e,\ jet) > 0.2$ after the subtraction takes place. However, if the electron and jet originate from distinct objects, each with high transverse momentum, the jet's subtracted four-momentum will be farther from the electron in $\eta - \phi$ space but retain the momentum of, in the case of high-p_T top decays, the b quark. In this case, the electron and jet are likely to be separated by $\Delta R(e,\ jet) > 0.2$ *and* pass the 25 GeV p_T cut.

Explicitly, the procedure is as follows:

1. Select good electrons. They must satisfy the full electron selection implemented in the analysis.
2. For each selected electron:
   - if the electron is within $\Delta R < 0.4$ of the nearest jet, mark the electron

  and nearest jet as needing to undergo overlap removal;
  - the electron cluster η and ϕ should be used for the ΔR calculation.

3. Select good jets in the event.
   - Apply $p_T > 25$ GeV and JVF cuts.
   - If this jet has been marked as needing to undergo overlap removal, the jet p_T and E cuts should be applied to the subtracted jet four-momentum.
   - If a matched electron's track was included in the jet's JVF calculation, the JVF cuts should be applied to the jet with the electron's track excluded.

4. For each selected electron
   - If $\Delta R < 0.2$ between the electron track and a selected jet, remove the electron from the event.
   - If the jet was marked as needing to undergo overlap removal, the ΔR separation between the electron and jet should be calculated using the subtracted jet four-momentum.

Note that the final observable of the $t\bar{t}$ resonances analysis, $m_{t\bar{t}}$, is *always* constructed using the fully calibrated jet (the *b*-jet candidate), never the subtracted jet four-momentum. If a jet marked as needing overlap removal is the only possible *b*-jet candidate on the leptonic side of the event, its subtracted four-momentum is required to have $p_T > 25$ GeV. Otherwise the jet will not be selected, and the event will be discarded.

7.3.2 Reconstruction performance of jets undergoing the overlap procedure

The p_T response of jets overlapping electrons is important; in some cases the jet in question is the only *b*-jet candidate on the leptonic side of the event, and must therefore have a $p_T > 25$ GeV with the overlapping electron four-momentum removed.

In order to measure the effect of the overlap removal procedure on the jets involved, the reconstructed jet is first matched to a corresponding particle jet. Particle jets (or truth jets) are constructed by clustering long-lived particles in simulation using the usual anti-k_t algorithm. The following scheme is used for the jet-truth jet matching:

- the truth jet must have a $p_T > 15$ GeV;
- the distance between them must be $\Delta R(\text{jet, truth jet}) < 0.2$.

If these requirements are met, the jet and truth jet are considered to represent the same object, and their properties are compared in the following plots.

Once reconstructed jets have been matched to jets at particle level, the overlap removal procedure must be reproduced for truth electrons and jets. If a reconstructed electron and reconstructed jet undergo the overlap removal procedure and if the electron has a matched electron at truth level which is within $\Delta R < 0.4$ of the truth jet, then the truth electron and truth jet undergo the same procedure as their reconstructed counterparts.

A comparison of p_T response between jets affected and unaffected by the overlap removal procedure jet is shown in Figure 7.9. In order to maximize statistics, an unweighted mixture of $t\bar{t}$ resonance Monte Carlo samples with several pole masses and widths were used. No significant degradation in the transverse momentum reconstruction performance is observed in jets undergoing the overlap procedure compared to those which do not.

7.3.3 Electron identification scale factors

The standard scale factors derived for `tight++` selection cuts are only valid for electrons well-separated from jets ($\Delta R(e,\ jet) > 0.4$), but under the developed overlap removal procedure, electrons and jets can be as near as $\Delta R(e,\ jet) = 0.2$. The

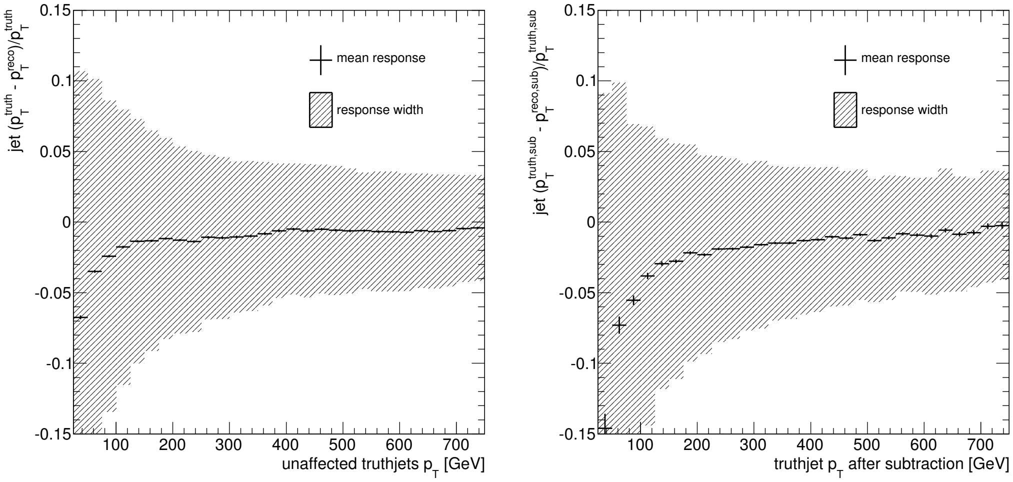

FIGURE 7.9: Comparison of the jet p_T response $(p_T^{truth} - p_T^{reco})/p_T^{truth}$ for jets unaffected by the electron overlap removal (left) and those undergoing overlap removal (right). The response after subtraction of the electron four-momentum is shown in the right-hand figure. No significant degradation in the jet response after subtraction is observed.

scale factors for the electron identification efficiency must be re-derived accordingly. Here the numerator of the efficiency is the number of prompt electrons passing the `tight++` requirements, and the denominator is the number of EM clusters matched to a track. The procedure outlined in this section for the scale factor derivation is based on that found in the ATLAS electron efficiency measurement [46].

7.3.4 $Z \to ee$ selection

The following tag and probe requirements are applied to each $Z \to ee$ candidate event, using the technique introduced in Section 7.1.1.

Tag selection	**Probe selection**
`tight++` identification	EM cluster matched to track
fires the trigger	$\lvert\eta\rvert < 2.47$ && $(1.37 < \lvert\eta\rvert < 1.52)$
$\lvert\eta\rvert < 2.47$ && $(1.37 < \lvert\eta\rvert < 1.52)$	$E_T > 25$ GeV
$E_T > 25$ GeV	
mini-isolation $/p_T < 0.05$	

The tag and probe are additionally required to be oppositely-charged and their invariant mass must fall in the window 80 GeV $< m_{ee} <$ 100 GeV.

7.3.5 Background estimation

It is non-trivial to measure the selection efficiency of prompt electrons in the data sample due to a significant non-prompt electron background for probes near jets. In order to describe the non-prompt background in the m_{ee} spectrum, data-driven templates are derived for both the denominator and numerator of the efficiency measurement. The template events are required to fail certain identification and isolation cuts, described in Section 7.3.5.1. Even after requiring failed ID and isolation cuts, there is some contamination of prompt electrons in the template. This contamination is accounted for by subtracting prompt electron events (predicted by MC) which also fail the ID and isolation cuts, yielding the corrected template. Once the background contribution is determined, the efficiency of prompt electrons is given by

$$\epsilon_{\mathrm{data}}^{tight} = \frac{N^{tight} - N_{bkg}^{num}}{N^{loose} - N_{bkg}^{denom}}, \tag{7.3}$$

where N^{loose} is the number of electrons which pass the probe selection, and N^{tight} is the number of electrons which additionally fulfill the `tight++` identification criteria. N_{bkg}^{num} and N_{bkg}^{denom} are the non-prompt contributions to the numerator and denominator of the efficiency calculation, respectively; their derivation is presented in the following two sections.

7.3.5.1 The non-prompt denominator contribution

The denominator of the efficiency measurement is contaminated with significantly more background than the numerator. In order to estimate the background contribution, the template of non-prompt electrons is normalized to the high-mass tail of the m_{ee} spectrum, 120 GeV $< m_{ee} <$ 250 GeV. This tail is far enough from the Z boson mass peak that the Drell-Yan contribution of prompt electrons in it is small compared to the background. Any Drell-Yan contamination in the tail is accounted for by subtracting the number of `tight++` electrons in the tail divided by the `tight++` efficiency taken from Monte Carlo. This procedure is summarized by the following equation:

$$N_{bkg}^{denom}\Big|_{peak} = N^{template}\Big|_{peak} \times \frac{N^{denom} - N^{num}/\epsilon_{\mathrm{MC}}^{tight}}{N^{template}}\Big|_{tail}. \tag{7.4}$$

The denominator m_{ee} distributions for two particular probe bins are shown in the left hand plots of Figure 7.10.

7.3.5.2 The non-prompt numerator contribution

For the numerator, the same background template is used as for the denominator, but it is normalized to the same-sign distribution in the high-mass tail of the m_{ee} spectrum, which is expected to be relatively free of prompt electrons:

$$N_{bkg}^{num}\Big|_{peak} = N^{template}\Big|_{peak} \times \frac{N_{SS}^{num}}{N^{template}}\Big|_{tail}. \tag{7.5}$$

The numerator m_{ee} distributions for two particular probe bins are shown in the right hand plots of Figure 7.10.

7.3.5.3 Reverse identification cuts for background templates

Two distinct sets of reverse identification cuts are considered in this study for the derivation of background templates. For the nominal template, probe electrons are required to fail the `loose++` identification cuts and isolation requirement. A second template is used to derive the uncertainty on the efficiency measurements due to the background template choice: probe electrons must fail the same cuts as for the nominal template, but the tag and probe electrons are required to have the same sign.

Figure 7.11 illustrates the same-sign background template in exemplary p_T and $\Delta R(e, \mathrm{jet})$ bins and can be compared to the corresponding nominal background template predictions in Figure 7.10.

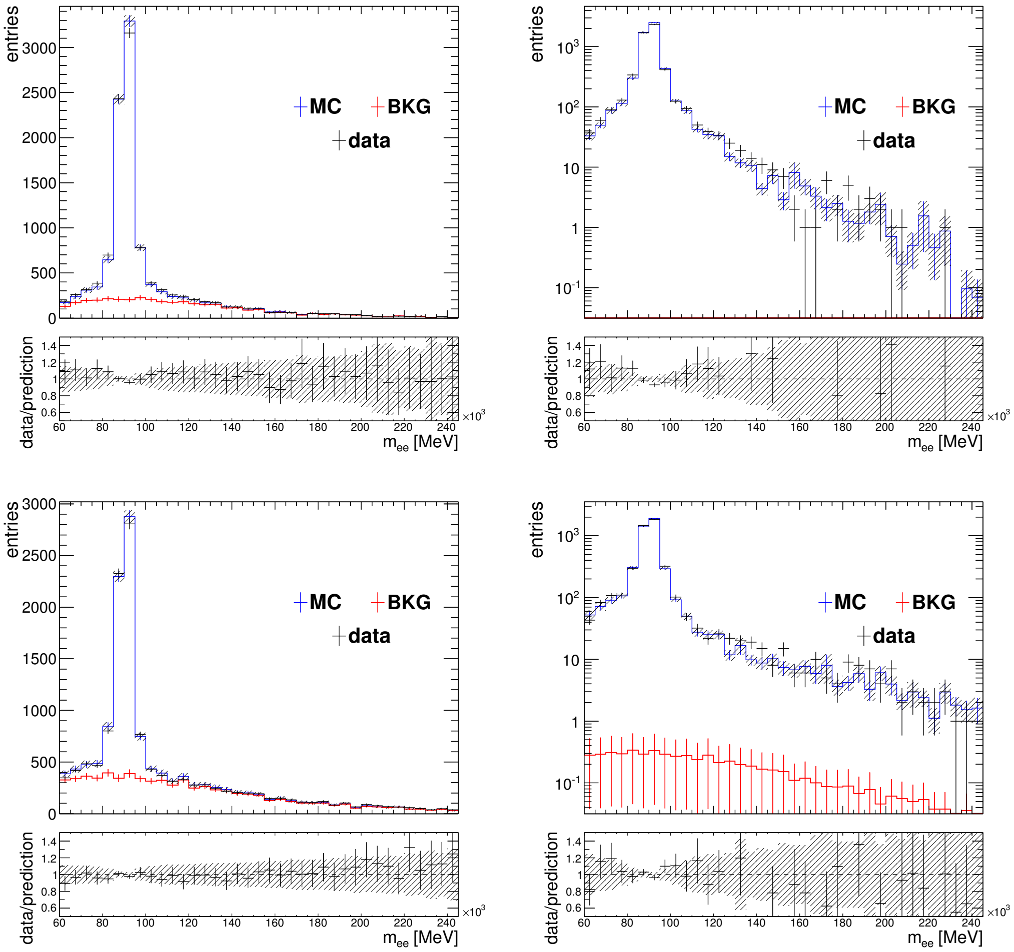

FIGURE 7.10: The data, background template, and MC m_{ee} spectra for the denominator (left) and numerator (right) of the electron identification efficiency. The lower panel of each figure shows the ratio between data and predicted yields in each bin. The top row shows the spectra for the 35 GeV $< p_T <$ 40 GeV bin. The bottom row shows the spectra for the $0.25 < \Delta R(e, \text{jet}) < 0.30$ bin. The background template shown is derived from the opposite-sign events whose probes fail the *loose*++ and isolation cuts. The nominal efficiency is calculated using this template. A log scale is used for the y-axis of the right hand plots so that agreement in the tail of the distribution is visible; note that the background template contribution is less than 0.05 events per bin for the upper right figure. The lower panel of each plot shows the ratio of the data prediction to that of the background template + MC. Only statistical uncertainties are shown.

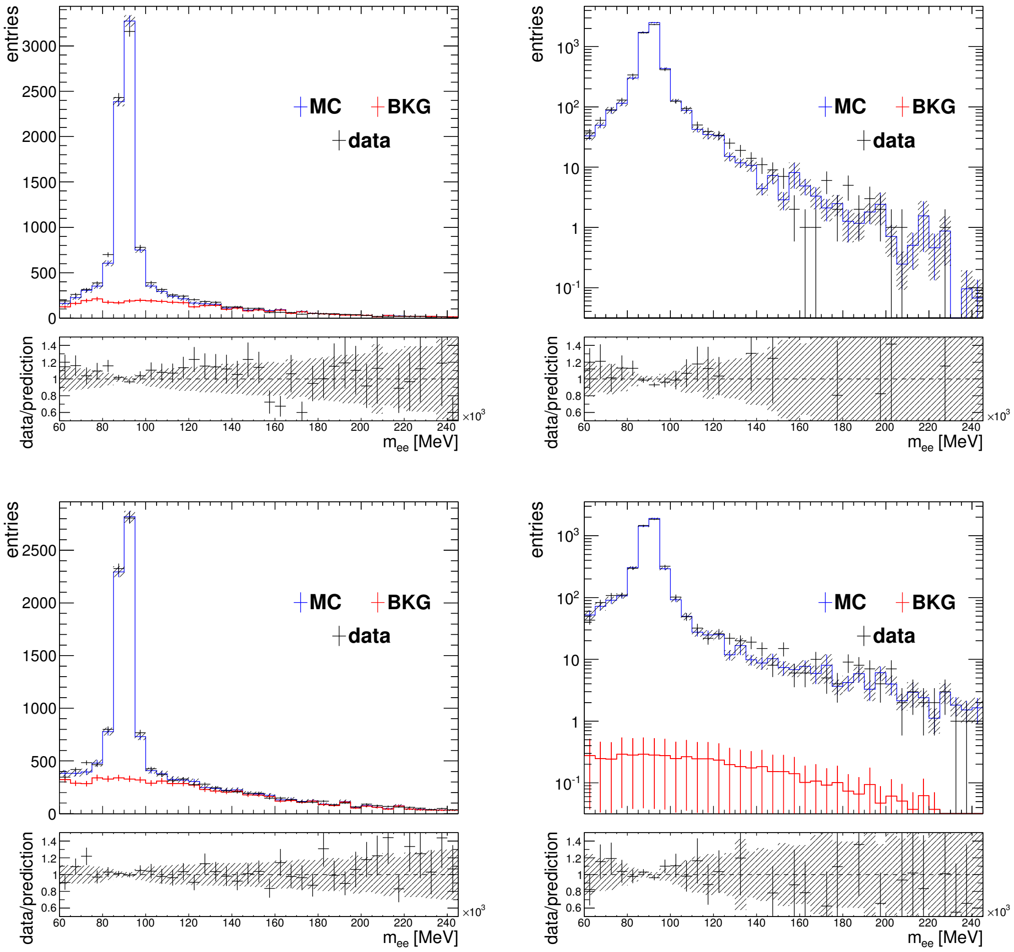

FIGURE 7.11: The data, background template, and MC m_{ee} spectra for the denominator (left) and numerator (right). The lower panel of each figure shows the ratio between data and predicted yields in each bin. The top row shows the spectra for the 35 GeV $< p_T <$ 40 GeV bin. The bottom row shows the spectra for the $0.25 < \Delta R(e, \mathrm{jet}) < 0.30$ bin. The background template shown is derived from same-sign events whose probes fail the *loose++* and isolation cuts. The efficiency calculated using this template is compared to that of the nominal template and the difference is taken as a systematic uncertainty. A log scale is used for the y-axis of the right hand plots so that agreement in the tail of the distribution is visible and to demonstrate the contribution of the background template; note that the background template contribution is less than 0.05 events per bin for the upper right figure. The lower panel of each plot shows the ratio of the data prediction to that of the background template + MC. Only statistical uncertainties are shown.

7.3.6 Uncertainties

The methods described above are altered in three ways in order to assess the scale factors' systematic uncertainty. The nominal definition of the Z-mass window is 80 GeV $< m_{ee} <$ 100 GeV. This is widened to 75 GeV $< m_{ee} <$ 105 GeV, and any differences in efficiency are taken as a systematic uncertainty. The isolation requirement on the tag electron is dropped, and any difference in efficiency is taken as an uncertainty due to the tag identification. Finally, the efficiencies derived using the two non-prompt background templates laid out in Section 7.3.5.3 are compared, and any difference is considered a systematic uncertainty.

Figure 7.12 compares the statistical uncertainty to the combined statistical and systematic uncertainty on the ID efficiency measured in data parameterized by $\Delta R(e, \text{jet})$ and the nearest jet p_T.

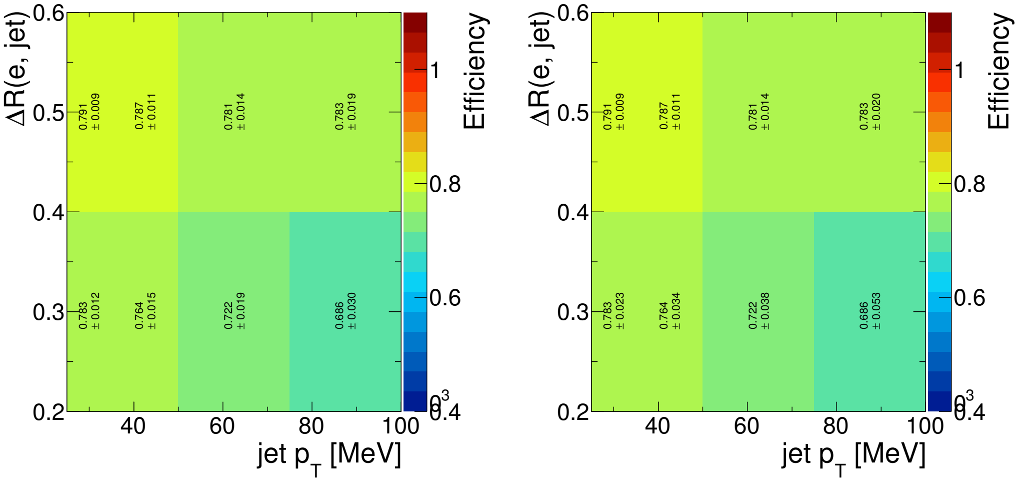

FIGURE 7.12: Comparison between the statistical uncertainty (left) and combined statistical and systematic uncertainty (right) on the ID efficiency measured in data parameterized by $\Delta R(e, \text{jet})$ and the nearest jet p_T.

7.3.7 Data vs prediction control plots

Figures 7.13-7.15 show the agreement between the data and the combined prediction from the MC and nominal background template for relevant kinematic variables. This is illustrated for both the denominator and numerator of the efficiency measurement.

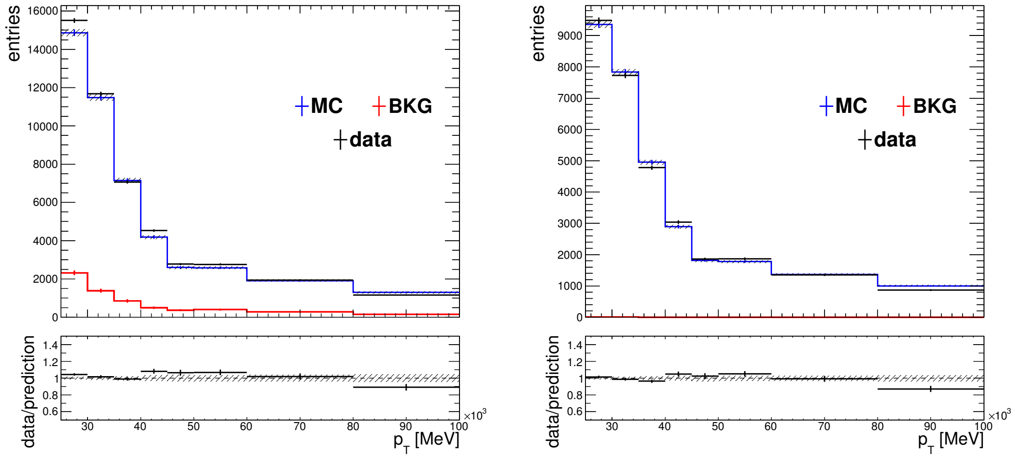

FIGURE 7.13: The p_T spectrum for electrons near jets ($\Delta R < 0.6$) in the denominator (left) and numerator (right). Only statistical uncertainties are shown.

7.3.8 Scale factor parameterization

For electrons reconstructed a distance $\Delta R > 0.6$ from the nearest accepted jet (after having subtracted the electron's four-momentum from the jet's under the conditions in Section 7.3.1), the standard `tight++` identification scale factors and relevant uncertainties are used. For electrons within $\Delta R < 0.6$ of a jet, the scale factors are parameterized as a function of η, p_T, $\Delta R(e, \text{jet})$, and the p_T of the nearest jet.

For electrons within $\Delta R < 0.4$ of the nearest jet, the ID efficiency depends strongly on the p_T of the jet, while for electrons farther than $\Delta R > 0.4$, this is not the case. Figure 7.16 demonstrates this effect. Similarly, the ID efficiency depends differently on the electron p_T for electrons within $\Delta R < 0.4$ of a jet and those without;

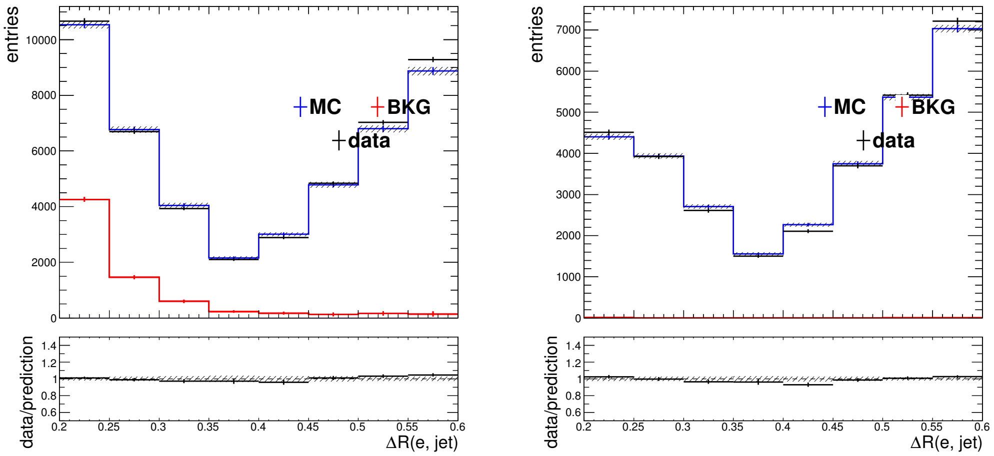

FIGURE 7.14: The closest jet ΔR spectrum for electrons near jets in the denominator (left) and numerator (right). Only statistical uncertainties are shown.

this difference is illustrated in Figure 7.17. For electrons within $\Delta R < 0.4$ of a jet two scale factors are multiplied: one parameterized by the electron p_T and one by the p_T of the nearest jet. For electrons with $\Delta R(e, \text{jet}) > 0.4$ only one, parameterized by the electron p_T, is used. Finally, a scale factor parameterized by the electron η is applied to all electrons with $\Delta R(e, \text{jet}) < 0.6$.

7.3.9 Results

Figures 7.18-7.20 show the final ID efficiency scale factors and uncertainties in both one- and two-dimensional parameterizations. As mentioned at the start of this section, these scale factors are being used in the current iteration of the $t\bar{t}$ resonances search in the single lepton channel at ATLAS.

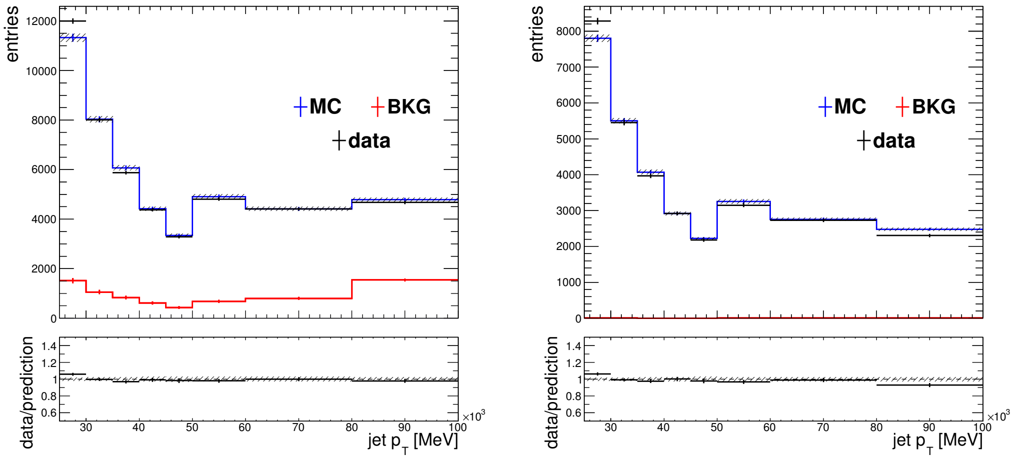

FIGURE 7.15: The closest jet p_T spectrum for electrons near jets ($\Delta R < 0.6$) in the denominator (left) and numerator (right). Only statistical uncertainties are shown.

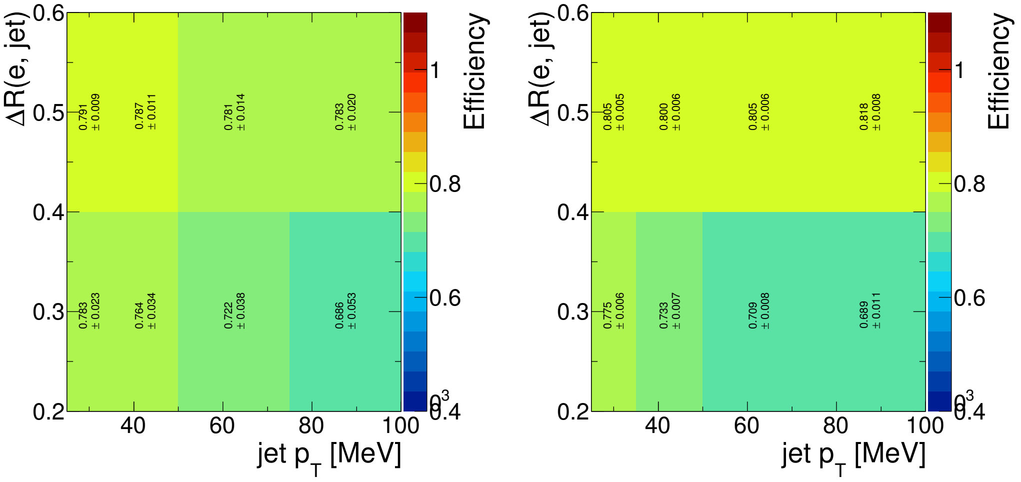

FIGURE 7.16: The electron ID efficiency in data (left) and MC (right) parameterized by the ΔR distance to the nearest jet and the p_T of the nearest jet. The efficiency depends strongly on the nearest jet's p_T for $0.2 < \Delta R(e, \text{jet}) < 0.4$. Statistical and all systematic uncertainties outlined in Section 7.3.6 are included.

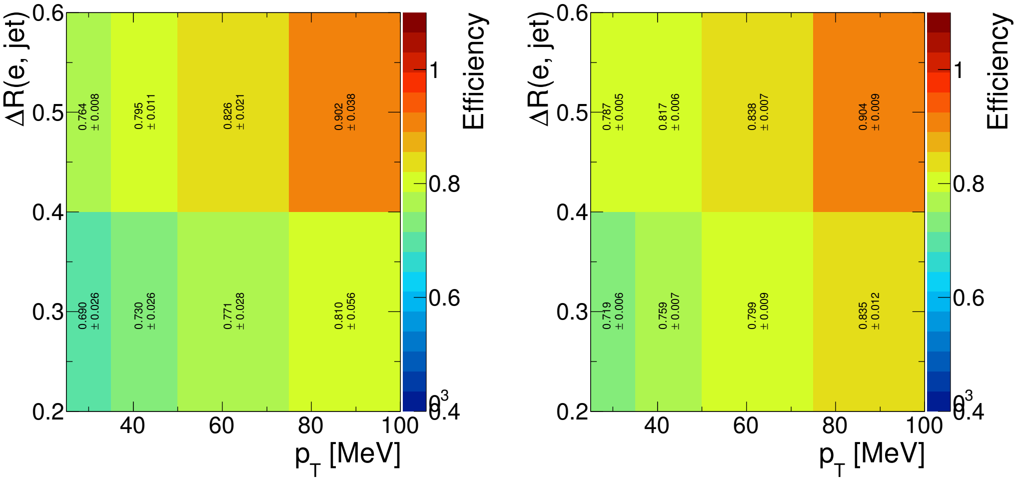

FIGURE 7.17: The electron ID efficiency in (left) data and (right) MC parameterized by the ΔR distance to the nearest jet and the electron p_T. Statistical and all systematic uncertainties outlined in Section 7.3.6 are included.

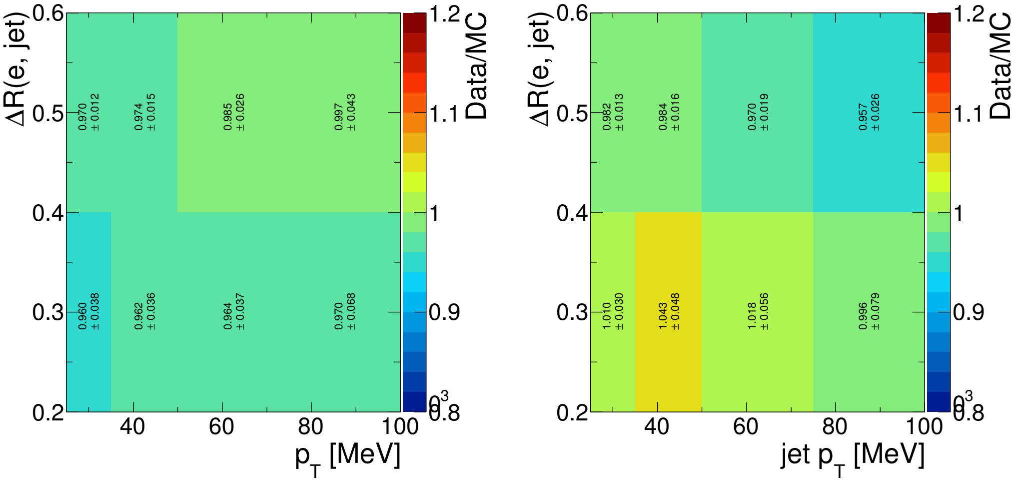

FIGURE 7.18: The derived efficiencies in data and and MC for electrons near jets ($\Delta R < 0.6$) parameterized by $\Delta R(e, \mathrm{jet})$ and electron p_T (left) and jet p_T (right). The lower panels of each figure show the ratio between data and MC efficiencies (the scale factor) in each bin. Statistical and all systematic uncertainties outlined in Section 7.3.6 are included.

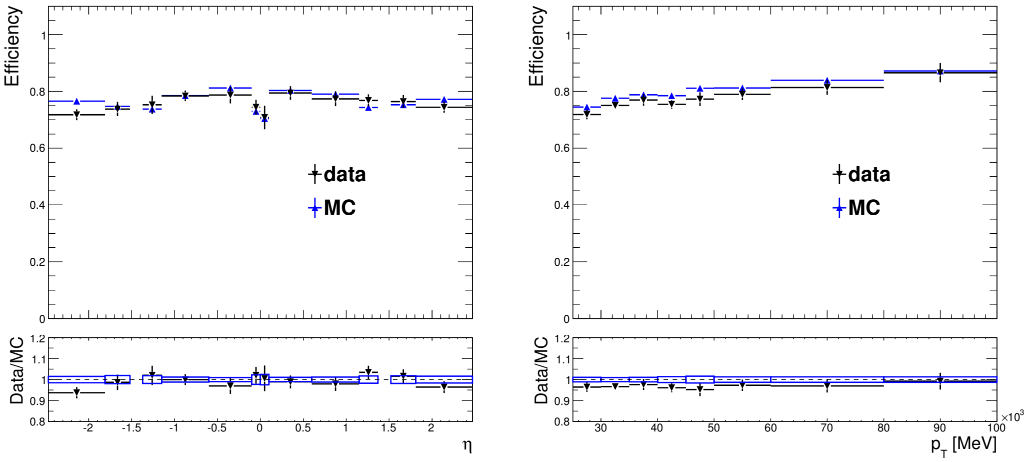

FIGURE 7.19: The derived efficiencies in data and and MC for electrons near jets ($\Delta R < 0.6$) parameterized by η (left) and p_T (right). The lower panels of each figure show the ratio between data and MC efficiencies (the scale factor) in each bin. Statistical and all systematic uncertainties outlined in Section 7.3.6 are included.

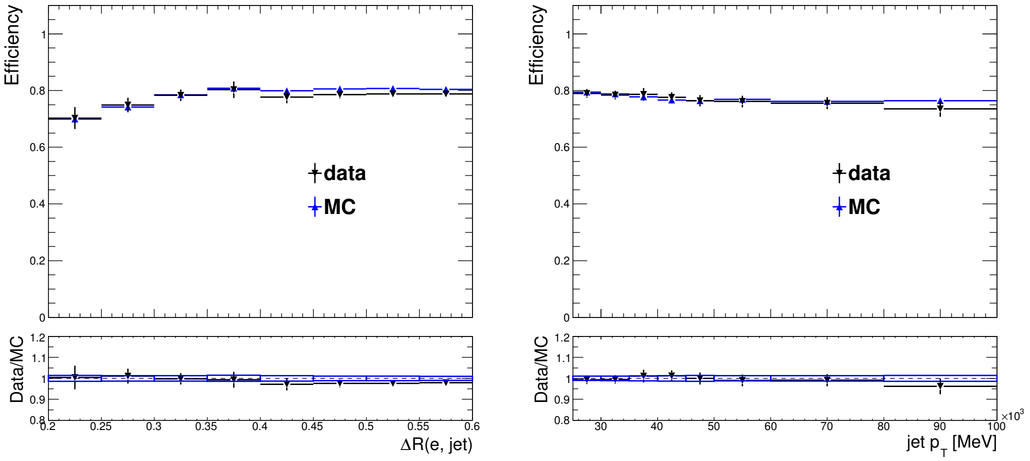

FIGURE 7.20: The derived scale factors for electrons near jets ($\Delta R < 0.6$) parameterized by ΔR to the nearest jet (left) and the p_T of the nearest jet (right). Statistical and all systematic uncertainties outlined in Section 7.3.6 are included.

8

Beyond the Standard Model Physics at a High Luminosity LHC with ATLAS

In addition to searching for exotic signatures with the LHC Run 1 data, it is also important to plan for future upgrades to both the ATLAS detector and the LHC itself. Understanding the expected sensitivity to BSM processes under various upgrade scenarios is necessary for the prioritization of detector and collider development projects and for planning the scope of the next generation of collider experiments.

This chapter discusses ATLAS's predicted sensitivity to several BSM benchmarks covering a range of physics topics under the High Luminosity LHC (HL-LHC) upgrade scenario, in which up to a predicted 3000 fb^{-1} of integrated luminosity would be delivered to the detector collaborations, with an instantaneous luminosity of up to $5\times10^{34}\ \mathrm{cm}^{-2}\ \mathrm{s}^{-1}$ [81]. This is a factor of ten increase over the currently projected 300 fb^{-1} delivered by 2021 [82]. Several anticipated upgrades to the ATLAS detector itself, known collectively with the concurrent LHC upgrades as the Phase-II upgrade, are also assumed in these studies.

The ATLAS sensitivity to new physics depends on jet, lepton, and missing energy reconstruction in the high-pile-up regime, with an expected average of between 140 and 200 interactions per bunch crossing for the 3000 fb^{-1} scenario. Detailed studies have been carried out using full simulations of the upgraded ATLAS detector [83], and the resulting reconstruction performance has been parameterized in terms of particle p_T and η, the number of interactions per crossing, and other relevant kinematic event information. In the analyses presented in this chapter, the parameterized reconstruction performance is applied to truth-level objects in order to quickly simulate the detector response for a given particle or event.

The feasibility studies outlined below were included in whole or in part in the ATLAS submission to the European Strategy Meeting [84], ATLAS Phase-II Letter of Intent [85], the Snowmass effort [86], and the ATLAS submission to the 2013 European Committee for Future Accelerators.

The work presented in this chapter was performed entirely by the author unless otherwise noted.

8.1 Software framework for ATLAS Phase-II upgrade physics feasibility studies

A suitable software framework was necessary to perform the analyses discussed in this chapter. The diversity of object and event selections required extreme flexibility to complete the studies efficiently. The software was designed in modules in order to accommodate the range of analyses carried out while keeping as much as possible common across analyses for economical use of time and disk resources.

The analysis chain is broken down into four distinct stages: event generation and parton showering (EG/PS), object selection, event selection, and plotting and limit setting. By splitting the procedure into several subtasks, common backgrounds are generated only once but passed through several different selection criteria required by different analyses.

The EG/PS stage is largely implemented through PYTHIA 8.1's C++ interface [63]. By default, the requested physics process is simulated and showered at leading order by PYTHIA, but user-supplied simulated events from any MC generator can also be read in for showering provided the data is formatted according to the Les Houches Accord [87]. Outgoing electrons, photons, and hadrons are clustered into anti-k_t jets immediately after showering is completed. The clustering algorithm is implemented as part of the FastJet library [79].

The object selection phase takes event data from the EG/PS step and selects photons, electrons, muons, and jets which pass the threshold and quality criteria required for a particular analysis. Before selection can occur, the expected efficiency and resolution of each object in the ATLAS detector is taken into account. Reconstruction efficiencies are simulated using random numbers thrown in the range [0,1]; an object whose number falls above the appropriate efficiency is marked as not reconstructed and discarded from the event before it may be selected. The trigger efficiency of each object is treated similarly. The $E_{\mathrm{T}}^{\mathrm{miss}}$ is calculated during this stage and is defined as the negative vector sum of the transverse momenta of all selected photons, electrons, muons and anti-k_t jets with $R = 0.4$.

Once object selection has taken place, analysis-dependent kinematic cuts are imposed on each event. The spectra used to compute the expected sensitivity to new physics are built from those that pass these final requirements. Expected limits are calculated using Bayesian methods similar to those outlined in Section 6.10.2 using the Bayesian Analysis Toolkit [88].

8.2 Vector boson scattering beyond the Standard Model

A major design goal of the LHC and its associated detectors is to probe physics at the TeV scale. One important reason for this is the predicted unchecked growth of the vector boson scattering (VBS) cross section above 1 TeV in the absence of the

Higgs boson. In VBS processes, electroweak bosons interact directly through SM quartic couplings and t- and u-channel trilinear couplings. In vector boson fusion (VBF) processes, they fuse through trilinear vertices to form intermediate bosons which subsequently decay. In the Standard Model, diagrams involving the Higgs damp the VBS cross section at high invariant mass, but it is crucial that this effect be confirmed experimentally. Many models predict the production of other BSM resonances at or above the TeV scale which similarly interfere with VBS processes.

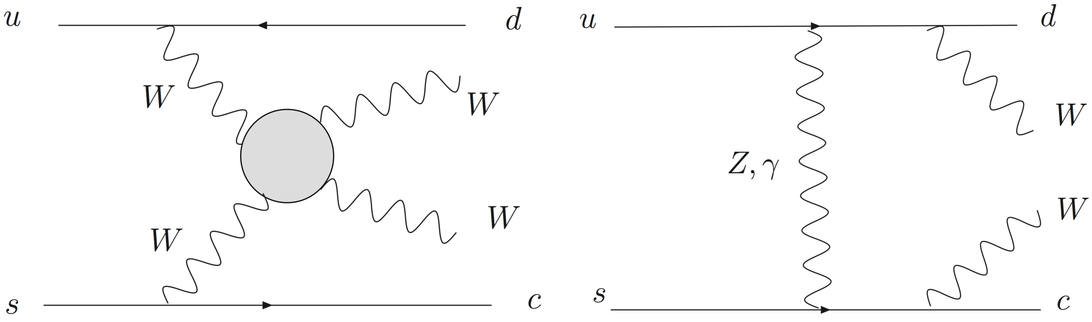

FIGURE 8.1: Feynman diagrams of an example vector boson scattering or fusion process (left) and an example non-VBS/F background diagram (right) with the same initial and final states, $us \to WWdc$ [89]. Another important non-VBS/F background is t-channel gluon exchange between two quarks with two radiated W-bosons. It has the same topology as the background illustrated in the right-hand diagram, with the Z/γ line replace by a gluon one.

Two studies of sensitivity to BSM scenarios are presented: the WW and ZZ final states in their fully leptonic decay modes. Loss of branching fraction notwithstanding, fully leptonic channels yield certain advantages over those involving hadronic boson decays. Lepton reconstruction performance is less sensitive to high pile-up conditions than that of jets, and lepton decay modes are less susceptible to backgrounds which are difficult to model, e.g. QCD. This is particularly true in the case of highly boosted topologies in which the adequate reconstruction of hadronically decaying high-p_T bosons is critical to separate signal from backgrounds.

An important kinematic feature of vector boson scattering and fusion processes at hadron colliders is the production of two forward, high-p_T quarks ("tag jets"). This characteristic event topology provides a powerful means of reducing the non-VBS/F diboson background.

8.2.1 Theory

In the generalized electroweak chiral Lagrangian (EWChL), there are eleven bosonic terms beyond those found in the Standard Model Lagrangian that are C and CP-invariant at next-to-leading order. Five introduce anomalous quartic couplings, and of these, two also conserve weak isospin to all orders. The coefficients of these two operators are labeled a_4 and a_5.

There are several proposed methods for unitarizing the scattering amplitudes arising from the EWChL, and two in particular are considered here. The first is founded on Padé unitarization and implemented in the model of Dobado et al. [90]. This method induces unitarization through a new resonance whose couplings are determined by the a_4 and a_5 coefficients. The second uses a minimal K-matrix unitarization technique but similarly includes high-mass resonances which couple to the electroweak bosons [91].

8.2.2 Object selection

Objects are required to pass these selection criteria in both analyses below:

- Electrons: $E_T > 25$ GeV, $|\eta| < 2.47$ (excluding $1.37 < |\eta| < 1.52$)
- Muons: $p_T > 25$ GeV, $|\eta| < 2.4$
- Anti-k_t jets with $R = 0.4$: $p_T > 50$ GeV, $|\eta| < 4.9$

Note in particular that jets in the forward calorimeter region of the detector are included in the following VBS/F analyses in order to reject non-VBS/F backgrounds. The rejection of forward jets originating from pile-up vertices is not possible since the inner detector tracking systems only operate for $|\eta| < 2.5$. To mitigate the effect of pile-up jets, a higher p_T threshold of 50 GeV is applied.

8.2.3 WW in the $e\mu$ final state

The WW scattering cross section is strongly dependent on a_4 and a_5 at high invariant mass. For simplicity, in this study a_5 is set to its Standard Model value of zero, and only ATLAS's sensitivity to a_4 is presented.

In the dilepton channel, the dominant background SM background is $t\bar{t}$ after applying $E_{\mathrm{T}}^{\mathrm{miss}}$ and jet multiplicity cuts. The $e\mu$ channel is relatively free from Z+jets. The contribution of non-prompt lepton backgrounds from W+jets and QCD in the dilepton channel is much smaller than that of $t\bar{t}$ and therefore not included in this study.

Standard Model $t\bar{t}$ and non-VBS WW production were simulated using PYTHIA 8.1. PYTHIA 6 with an EWChL extension was used to generate WW scattering events for several values of a_4, including the SM scattering prediction for $a_4 = 0$. Table 8.1 shows the cross sections of the main $t\bar{t}$ background and of WW scattering for various values of a_4 in the dilepton channel at pp collisions of $\sqrt{s} = 14$ TeV.

Table 8.1: Summary of WW production cross sections at $\sqrt{s} = 14$ TeV with $a_5 = 0$.

Process	σ BR (fb)
$t\bar{t}$	43.0×10^3
$a_4 = 0$	2.21
$a_4 = 0.003$	3.33
$a_4 = 0.01$	7.11
$a_4 = 0.03$	18.7

8.2.3.1 Event selection

Events are considered WW VBS candidates provided they meet the following criteria:

- there is exactly one selected muon and one selected electron with opposite charges;
- at least one selected lepton fires the trigger;
- there are at least two selected jets;
- the $E_{\mathrm{T}}^{\mathrm{miss}}$ of the event is greater than 50 GeV.

Reconstructing the true WW invariant mass is not possible since there are two final-state neutrinos in the dilepton channel. m_{lljj}, defined as the 4-body invariant mass of the two selected leptons and the two leading jets in the event, was found to be strongly correlated with m_{WW} and is used in its stead. The large η gap between the two tag jets in VBS events is naturally taken into consideration by this variable since greater jet angular separations result in higher m_{lljj} values.

8.2.3.2 Statistical analysis

ATLAS's expected sensitivity to non-zero a_4 is calculated by constructing templates of the m_{lljj} spectrum for backgrounds plus WW scattering signal for various values of a_4. For each value of a_4 the likelihood function is defined as the Poisson probability product over all m_{lljj} bins for the background plus signal (pseudodata) given an expectation derived from the $a_4 = 0$ spectrum. The normalization of the diboson background is given by the theory cross section, while the $t\bar{t}$ normalization is constrained by the pseudodata in the low-m_{lljj} region.

The expected upper limits on a_4, used here as a measure of sensitivity, are shown in Table 8.2. The distribution of m_{lljj} and a representative limit curve as a function of a_4 are shown in Figure 8.2.

Table 8.2: Summary of expected upper limits for a_4 at the 95% confidence level using the $pp \to WW + 2j \to e\mu + 2j$ search at pp collision center-of-mass energy of 14 TeV.

model	300 fb^{-1}	1000 fb^{-1}	3000 fb^{-1}
a_4	0.066	0.025	0.016

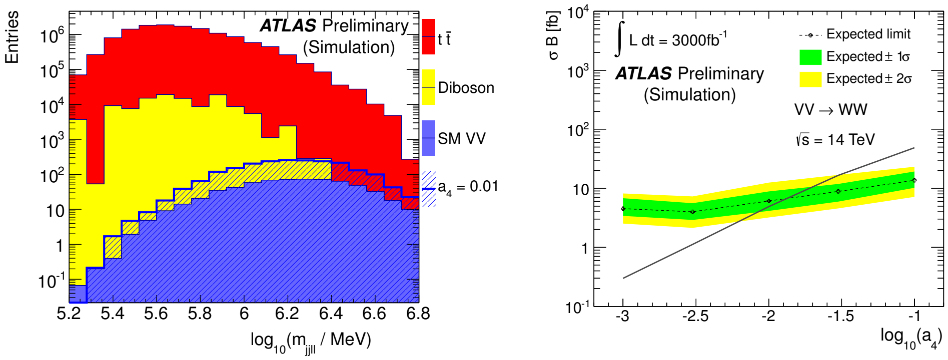

FIGURE 8.2: The reconstructed 4-body mass spectrum using the two leading leptons and jets (left) and expected limits as a function of a_4 (right) using the $e\mu$ channel with 3000 fb^{-1} at pp center-of-mass collision energy of 14 TeV. The background labeled "SM VV" corresponds to $a_4 = 0$.

8.2.4 ZZ in the four lepton final state

Vector boson scattering in the $ZZ \to \ell\ell\ell\ell$ final state has a relatively small cross section, but unlike the case of $WW \to \ell\nu\ell\nu$, reconstruction of the ZZ invariant mass is possible and extremely clean. As in the WW channel, two jets are required in addition to the four leptons in order to reduce the non-VBS Standard Model diboson production, which is the only appreciable background.

MadGraph 1.4.2 [33] was used to generate the non-VBS background where ZZ production is accompanied by two jets with a minimum p_T of 20 GeV. SM and non-SM ZZ production via vector boson scattering was simulated using WHIZARD 2.1.0 [92]. In both cases Z bosons were required to decay to electron or muon pairs. Table 8.3 enumerates the cross sections of various relevant processes in the four-lepton channel at $\sqrt{s} = 14$ TeV.

The model implemented in WHIZARD induces resonances with two free parameters: the resonance pole mass and its coupling to the vector bosons, g. g is measured in units of the coupling between the SM Higgs and W bosons and is set to values between 1.0 and 2.5.

Table 8.3: Summary of $ZZ \to 4\ell$ production cross sections at $\sqrt{s} = 14$ TeV. The non-VBS $ZZjj$ background was generated with a jet $p_T > 20$ GeV requirement.

Process	σ BR (fb)
non-VBS $ZZjj$	6.66
SM VBS ZZ	0.80
SM VBS + 500 GeV Resonance, $g = 1.0$	1.03
SM VBS + 1 TeV Resonance, $g = 1.75$	0.91
SM VBS + 1 TeV Resonance, $g = 2.5$	0.98

8.2.4.1 Event selection

Events are considered ZZ VBS candidates provided they meet the following criteria:

- there are exactly four selected leptons which can be separated into two opposite sign, same flavor pairs;
- at least one selected lepton fires the trigger;
- there are at least two selected jets;
- $m_{jj} > 1$ TeV, where m_{jj} is the invariant mass of the two highest-p_T selected jets.

The m_{jj} requirement of 1 TeV greatly reduces the contribution from jets accompanying non-VBS diboson production. Figure 8.3 shows the jet-jet invariant mass distribution before this cut and the reconstructed 4-lepton invariant mass distribution after it. The resonance peak is clearly seen above the background contribution in this simulated dataset normalized to 3000 fb^{-1}.

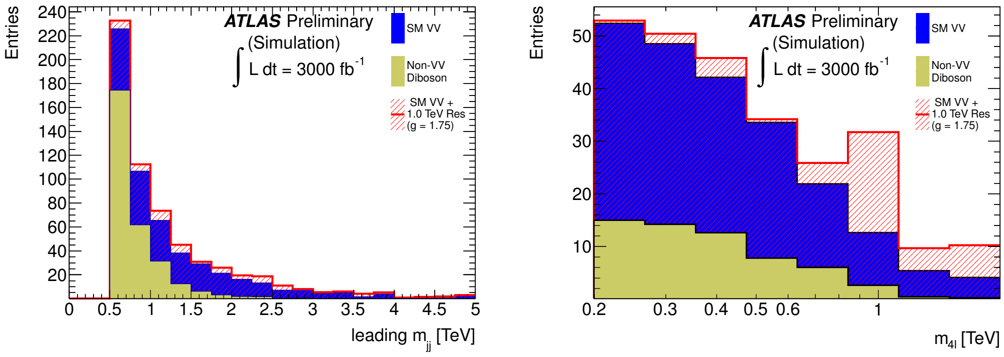

FIGURE 8.3: The leading jet-jet invariant mass (m_{jj}) distribution for simulated events in the $pp \to ZZ + 2j \to \ell\ell\ell\ell + 2j$ channel (left), and the reconstructed 4-lepton mass ($m_{4\ell}$) spectrum for this channel after requiring $m_{jj} > 1$ TeV (right). The spectra are normalized to $3000\,\text{fb}^{-1}$.

8.2.4.2 Statistical analysis

In order to determine the expected sensitivity to BSM ZZ resonances, the background-only p_0-value expected for signal+background is calculated using the $m_{4\ell}$ spectrum. In Table 8.4 the p_0-values have been converted to the corresponding number of Gaussian σ in significance. The increase in significance with integrated luminosity is shown for different resonance masses and couplings. It is clear that the luminosity gains are significant for a range of ZZ resonances and couplings, with significance improvements as much as 6.4σ.

Table 8.4: Summary of expected sensitivity to anomalous VBS ZZ signal at $\sqrt{s} = 14$ TeV, quoted in the terms of the expected number of Gaussian σ in significance. The coupling constant, g, is measured in units of the W boson's coupling to the Higgs boson.

model	$300\,\text{fb}^{-1}$	$3000\,\text{fb}^{-1}$
$m_{\text{resonance}} = 500$ GeV, $g = 1.0$	2.4σ	7.5σ
$m_{\text{resonance}} = 1$ TeV, $g = 1.75$	1.7σ	5.5σ
$m_{\text{resonance}} = 1$ TeV, $g = 2.5$	3.0σ	9.4σ

In the signal-enhanced kinematic region of $m_{4\ell} > 200$ GeV, a measurement of the integrated VBS $pp \to ZZ + 2j \to 4\ell + 2j$ cross section is possible with a precision of 10% given 3000 fb^{-1} of integrated luminosity; cf. 30% given 300 fb^{-1}.

8.2.5 Conclusions

Results of sensitivity studies for high-mass WW and ZZ scattering have been presented, comparing ATLAS datasets of 300 fb^{-1}, 100 fb^{-1}, and 3000 fb^{-1} of integrated luminosity at a pp collision energy of 14 TeV. The increase of a factor of ten in integrated luminosity makes ATLAS sensitive to potential high-mass BSM VV resonances and a_4 values smaller by up to a factor of four.

For a range of parameter values in models of new physics, new resonances in weak boson scattering in the $ZZ \to 4\ell$ final state can only be discovered with the increased integrated luminosity. The increased integrated luminosity is also needed to make a definitive measurement of the SM cross section and demonstrate that unitarization of the high-energy VV-scattering amplitudes is occurring as predicted by the SM Higgs mechanism.

8.3 Exotic dilepton and $t\bar{t}$ resonances

Upgrades to the LHC will naturally boost ATLAS's sensitivity to exotic high-mass resonances due to improved statistics at higher center-of-mass energies. Across the range of BSM models and corresponding parameters, the near-universal characteristic of massive particle decays is the production high-p_T final state leptons, photons, and jets. It is important that upgrades to the detector sustain the reconstruction performance of these objects under the new accelerator conditions. This section discusses the expected sensitivity to new high-mass resonances given an ATLAS dataset of 300, 1000, and 3000 fb^{-1} at $\sqrt{s} = 14$ TeV. Several benchmarks of high-mass resonances with various production and decay modes are considered in order to gauge detector performance over the wide variety of possible new BSM particles.

8.3.1 Object selection

The following object selection cuts were used for all exotic resonance analyses unless otherwise noted.

- Electrons: $E_T > 25$ GeV, $|\eta| < 2.47$ (excluding $1.37 < |\eta| < 1.52$)
- Muons: $p_T > 25$ GeV, $|\eta| < 2.4$
- Anti-k_t jets with $R = 0.4$: $p_T > 25$ GeV, $|\eta| < 2.5$
- Anti-k_t jets with $R = 1.0$: $p_T > 250$ GeV, $|\eta| < 2.5$

8.3.2 Search for exotic dilepton resonances

The search for high-mass particles decaying to a pair of leptons is one of the simplest of exotic searches, but it pushes the limits of the detector's lepton reconstruction performance. The Sequential Standard Model (SSM) Z' boson is used as a benchmark model for high-mass dilepton resonances in this study [93]. The SSM Z' boson inherits the fermion couplings of the Standard Model Z boson, and its width scales with the pole mass from that of the Z boson. Since the momentum resolutions of electrons and muons are governed by different mechanisms at high-p_T, the sensitivity in the dielectron and dimuon decay channels are presented separately.

The dominant background to a potential resonance is high-mass Standard Model Drell-Yan production. $t\bar{t}$ and diboson production are both significantly smaller, and their effect on the expected sensitivity is therefore not considered in this study. Events with non-prompt electrons from photon conversions may also pass the selection of this analysis, but it is assumed that the necessary rejection of this process will be attained by the upgraded detector.

PYTHIA 8.1 was used to generate leading order predictions for both the Drell-Yan background and SSM Z' signal.

8.3.2.1 Event selection

Events are considered $Z' \to \ell\ell$ candidates provided they meet the following criteria:

- there are exactly two selected same-flavor leptons;
- at least one selected lepton fires the trigger.

The charge misidentification rate is significantly lower for muons than for electrons at high-p_T due to the additional tracking hits at a large radius provided by the muon spectrometer. Therefore, muons in $Z' \to \mu\mu$ candidate events are additionally required to be oppositely charged.

8.3.2.2 Statistical analysis

In order to gauge the expected sensitivity to SSM Z' bosons, templates of the $m_{\ell\ell}$ spectrum are constructed for the Drell-Yan background plus varying amounts of signal at different resonance masses and cross sections. The likelihood function for a particular mixture of signal and background (pseudodata) is defined as the Poisson probability product over all $m_{\ell\ell}$ bins for the pseudodata given the background-only expectation in each bin. The normalization of the Drell-Yan background is constrained by the low-$m_{\ell\ell}$ region of the pseudodata, which is dominated by SM Z boson production.

The expected limits in the absence of signal, which are used as a measure of sensitivity using statistical errors only, are shown in Table 8.5. The $m_{\ell\ell}$ distribution and the resulting limits as a function of Z'_{SSM} pole mass are illustrated in Figures 8.4 and 8.5 for the ee and $\mu\mu$ channels, respectively. The increase of a factor of ten in integrated luminosity raises the sensitivity to high-mass dilepton resonances by up to 1.3 TeV.

Table 8.5: Summary of the expected limits for $Z'_{SSM} \rightarrow ee$ and $Z'_{SSM} \rightarrow \mu\mu$ searches in the Sequential Standard Model for pp collisions at $\sqrt{s} = 14$ TeV. All limits are quoted in TeV.

model	$300\,\mathrm{fb}^{-1}$	$1000\,\mathrm{fb}^{-1}$	$3000\,\mathrm{fb}^{-1}$
$Z'_{SSM} \rightarrow ee$	6.5	7.2	7.8
$Z'_{SSM} \rightarrow \mu\mu$	6.4	7.1	7.6

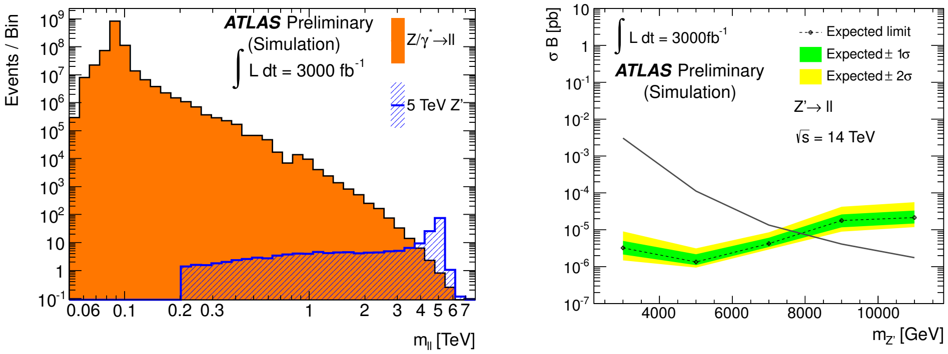

FIGURE 8.4: The reconstructed dielectron mass spectrum (left) and expected limits (right) for the Z'_{SSM} search with $3000\,\mathrm{fb}^{-1}$ for pp collisions at $\sqrt{s} = 14$ TeV. The highest-mass bin includes the overflow.

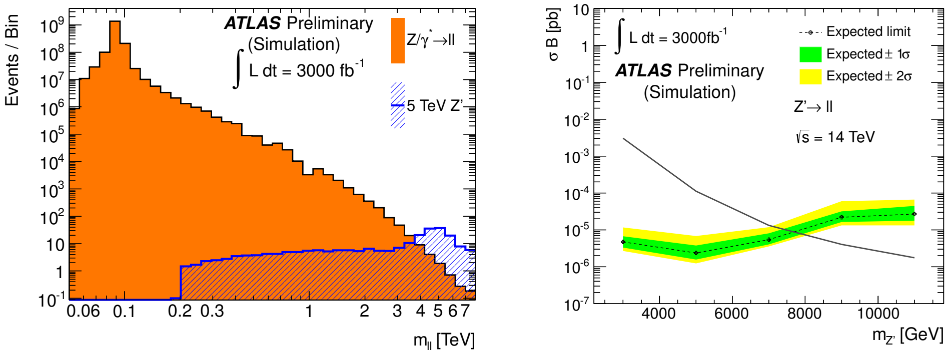

FIGURE 8.5: The reconstructed dimuon mass spectrum (left) and expected limits (right) for the Z'_{SSM} search with $3000\,\mathrm{fb}^{-1}$ for pp collisions at $\sqrt{s} = 14$ TeV. The highest-mass bin includes the overflow.

8.3.3 Searches for $t\bar{t}$ resonances

While searches for $t\bar{t}$ resonances are interesting in their own right, their performance also serves as a benchmark for analyses involving cascade decays to $E_{\mathrm{T}}^{\mathrm{miss}}$, leptons, and light- and heavy-flavor jets. Techniques for the reconstruction of complex decays involving highly boosted topologies become more important as exclusion limits of exotic particles are pushed to higher masses. It is therefore crucial to assess the reach of searches at high mass with complicated final states, such as those for $t\bar{t}$ resonances, given the HL-LHC scenario.

Two benchmark scenarios are considered: the RS KK gluon and topcolor Z' boson introduced in Section 2.2. This combination provides coverage of strongly- and weakly-produced resonances as well as resonance widths narrower (Z') and wider (KK gluon) than the detector $m_{t\bar{t}}$ resolution. The expected sensitivity to exotic $t\bar{t}$ resonances in both the dilepton and lepton plus jets decay modes of the $t\bar{t}$ pair is presented in this study.

The lepton plus jets final state is completely reconstructible after leveraging the W-mass constraint for the leptonically decaying top quark. This improves the sensitivity of the search, especially for the narrow topcolor Z' resonance. However, the lepton plus jets mode has significant non-$t\bar{t}$ backgrounds, including W+jets and QCD, and is susceptible to the merging of the hadronic top decay products at high-p_T.

The dilepton decay channel is less affected by decay product merging because leptons, and muons in particular, are still generally identifiable when reconstructed near the b-quark jet. Its main non-$t\bar{t}$ backgrounds are Z+jets and diboson production, each of which are largely mitigated by vetoing events with a dilepton invariant mass near the Z boson mass peak. The dilepton channel does not allow for reconstruction of the resonance mass, though, due to the presence of two final state neutrinos.

Nevertheless, by studying both channels in tandem sensitivity gains from the lepton plus jets channel can be compared to those of the less sensitive, but more robust, dilepton channel.

PYTHIA 8.1 was used to generate leading order predictions for all signal and background processes.

8.3.3.1 Lepton plus jets event selection

Events are considered $t\bar{t}$ candidates in the lepton plus jets channel provided they meet the following criteria:

- there is exactly one selected lepton which fires the trigger;
- there is at least one selected anti-k_t jet with $R = 0.4$ (the leptonic top b jet);
- there is at least one selected anti-k_t jet with $R = 1.0$ and mass $m_{\text{jet}} > 120$ GeV (the hadronic top quark jet);
- the $E_{\mathrm{T}}^{\text{miss}}$ of the event is greater than 50 GeV.

The selected lepton and hadronic top quark jet are required to be separated by $\Delta R > 1.0$. If there are multiple hadronic top quark jet candidates which fulfill this criterion, the one with the highest p_T is chosen. In order to prevent the double-counting of calorimeter deposits in jets originating from different clustering algorithms, the leptonic top b jet and hadronic top quark jet are required to be separated by $\Delta R > 1.5$. If there are multiple leptonic top b jet candidates that pass this requirement, the one with the highest p_T is chosen.

The p_z of the neutrino is determined by imposing the W boson mass constraint on the lepton-neutrino system, as introduced in Section 6.6.1. If there are two real-valued p_z solutions, the one with the smallest $|p_z|$ is used. If there are no real-valued p_z solutions, the $E_{\mathrm{T}}^{\text{miss}}$ vector is varied minimally to obtain one real solution.

The four-momentum of the $t\bar{t}$ system is defined as the sum of the four-momenta of the selected lepton, neutrino, leptonic top b jet, and top-jet. $m_{t\bar{t}}$ is the invariant mass of this sum.

8.3.3.2 Dilepton event selection

Events are considered $t\bar{t}$ candidates in the dilepton channel provided they meet the following criteria:

- there are exactly two selected opposite-sign leptons;
- at least one lepton fires the trigger;
- there are at least two selected anti-k_t jets with $R = 0.4$ (b quark jets);
- the $E_{\mathrm{T}}^{\mathrm{miss}}$ of the event is greater than 60 GeV.

In order to reduce the Z+jets background, selected same-flavor leptons are required to have a combined invariant mass outside of the Z boson mass window, defined as 81 GeV $< m_{\ell\ell} <$ 101 GeV.

The H_T of an event is defined as the scalar sum of the transverse momenta of the two selected leptons, the two leading jets, and the $E_{\mathrm{T}}^{\mathrm{miss}}$. It is correlated to the invariant mass of the two top quarks in the event and is used as the sensitive variable to distinguish signal from background in the statistical analysis below.

8.3.3.3 Statistical analysis

The statistical analysis performed is similar to that outlined in Section 8.3.2.2. The expected sensitivity to each resonance model is determined using templates of the $m_{t\bar{t}}$ spectrum for the SM background and signals of varying masses and cross sections in the lepton plus jets channel. H_T is used as the sensitive variable in the dilepton channel. The likelihood function for a particular mixture of signal and background

Table 8.6: Summary of the expected limits for $g_{KK} \to t\bar{t}$ and $Z'_{\text{topcolor}} \to t\bar{t}$ searches in the lepton plus jets (dilepton) channel for pp collisions at $\sqrt{s} = 14$ TeV. All limits are quoted in TeV.

model	$300\,\text{fb}^{-1}$	$1000\,\text{fb}^{-1}$	$3000\,\text{fb}^{-1}$
g_{KK}	4.3 (4.0)	5.6 (4.9)	6.7 (5.6)
Z'_{topcolor}	3.3 (1.8)	4.5 (2.6)	5.5 (3.2)

(pseudodata) is defined as the Poisson probability product over all $m_{t\bar{t}}$ or H_T bins for the pseudodata given the background-only expectation in each bin.

In the lepton plus jets channel, the W+jets background normalization is given by the theory cross section, while the SM $t\bar{t}$ background is constrained by the low-$m_{t\bar{t}}$ region. In the dilepton channel the theory cross section is used to normalize the Z+jets and diboson backgrounds, while the $t\bar{t}$ background normalization is constrained by the low-H_T region. The resulting expected limits in the absence of signal, which are used as a measure of sensitivity using statistical errors only, are shown in Table 8.6.

The $m_{t\bar{t}}$ (H_T) distribution and the resulting limits as a function of the g_{KK} pole mass for the lepton plus jets (dilepton) channel are shown in Figure 8.6 (Figure 8.7). Equivalent information for the topcolor Z' in the lepton plus jets channel is shown in Figure 8.8. The increase of a factor of ten in integrated luminosity raises the masses at which the Kaluza Klein gluon (topcolor Z') can be probed in the $t\bar{t}$ decay mode from 4.3 (3.3) TeV to 6.7 (5.5) TeV—a gain of up to 2.4 TeV in exclusion reach.

8.4 BSM Higgs resonances in the $\mu\mu$ final state

In this section the expected gain in sensitivity to the neutral Minimal Supersymmetric Standard Model (MSSM) Higgs bosons, H and A, in the dimuon channel is discussed if the ATLAS dataset were increased from 300 fb^{-1}to 3000 fb^{-1}. The production cross sections are computed as a function of m_ϕ and $\tan\beta$ under the m_h^{max} scenario [94], where ϕ refers to H or A.

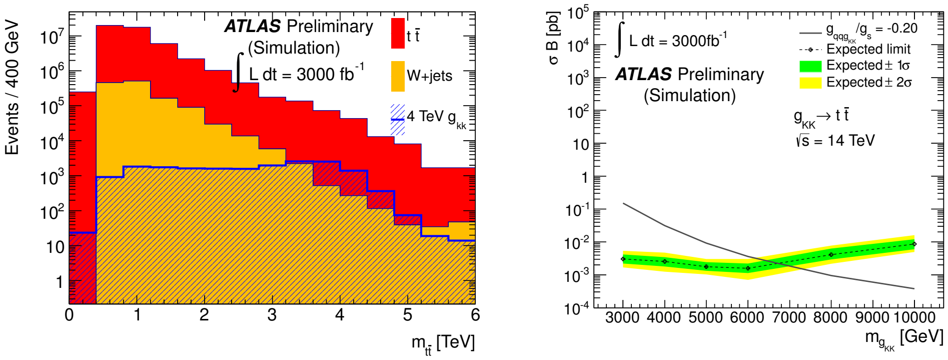

FIGURE 8.6: The reconstructed resonance mass spectrum (left) and expected limits (right) for the $g_{KK} \to t\bar{t}$ search in the lepton plus jets channel with $3000\,\text{fb}^{-1}$ for pp collisions at $\sqrt{s} = 14$ TeV. The highest-mass bin includes the overflow.

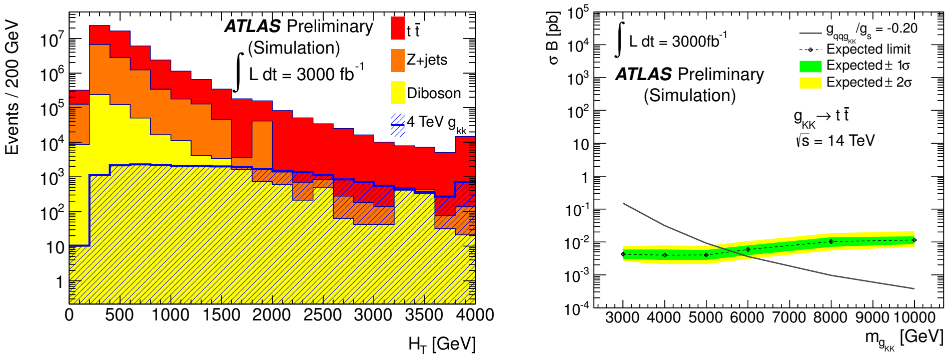

FIGURE 8.7: The reconstructed resonance H_T spectrum (left) and expected limits (right) for the $g_{KK} \to t\bar{t}$ search in the dilepton channel with $3000\,\text{fb}^{-1}$ for pp collisions at $\sqrt{s} = 14$ TeV. The highest-H_T bin includes the overflow.

If these BSM Higgs bosons have already been discovered in the $\tau\tau$ channel with the 300 fb^{-1} dataset, it is important to establish the pattern of their leptonic couplings and to check that the coupling is proportional to the lepton mass. Some of the parameter space in the MSSM m_h^{max} scenario has been ruled out by analysis of the 2011 ATLAS dataset [95], but a large portion of the high m_ϕ region is yet to be excluded. The increased integrated luminosity is required to observe the $\phi \to \mu\mu$ signal in the corresponding mass range.

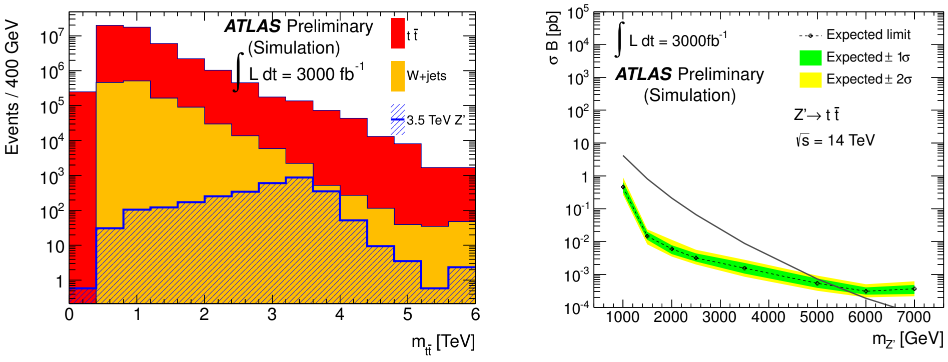

FIGURE 8.8: The reconstructed resonance mass spectrum (left) and expected limits (right) for the $Z'_{\text{topcolor}} \to t\bar{t}$ search in the lepton plus jets channel with 3000 fb^{-1} for pp collisions at $\sqrt{s} = 14$ TeV. The highest-mass bin includes the overflow.

8.4.1 Monte Carlo simulation

The SM background is dominated by the Drell-Yan process, followed by $t\bar{t}$ production; diboson production is substantially smaller. Therefore, only the Drell-Yan and $t\bar{t}$ backgrounds are considered in this study. PYTHIA 8.1 [63] was used to generate the $Z/\gamma^* \to \mu\mu$ and $t\bar{t}$ backgrounds. MadGraph 1.5.7 [33] was used to generate the $\phi \to \mu\mu$ signal.

The Drell-Yan and $t\bar{t}$ cross sections are taken from PYTHIA at leading order, while the $\phi \to \mu\mu$ signal cross sections were calculated by the LHC Higgs Cross Section Working Group [96] at next-to next-to leading order (NNLO). Both gluon-gluon fusion and bbA production modes are included in the MSSM Higgs cross sections, and the bbA production cross section in the 5-flavor scheme is used.

8.4.2 Event selection

Events are considered $\phi \to \mu\mu$ candidates provided they meet the following criteria:

- there are exactly two reconstructed muons with $p_T > 25$ GeV, $|\eta| < 2.5$;
- at least one selected muon fires the trigger;

Table 8.7: Summary of expected sensitivity to a heavy MSSM Higgs boson $\phi \to \mu\mu$ signal quoted in terms of the number of Gaussian σ in significance. For each of the three $\tan\beta$ values shown, the signal significance has been computed for m_ϕ values between 200 GeV and 1 TeV in steps of 100 GeV. A subset of these results are shown above.

	b-veto		b-tag		combined	
m_ϕ [GeV]	300 fb^{-1}	3000 fb^{-1}	300 fb^{-1}	3000 fb^{-1}	300 fb^{-1}	3000 fb^{-1}
$\tan\beta = 20$						
300	5.2	16.5	3.1	9.9	6.2	19.3
400	1.9	6.0	1.4	4.5	2.4	7.6
500	0.6	2.0	0.6	2.0	0.9	2.8
$\tan\beta = 40$						
500	3.8	12.1	4.0	12.8	5.6	17.6
600	2.4	7.6	3.1	9.8	3.9	12.4
700	1.5	4.7	2.2	7.0	2.7	8.5
$\tan\beta = 60$						
800	1.9	6.1	3.9	12.3	4.3	13.7
900	1.1	3.4	2.9	9.3	3.1	9.9
1000	0.8	2.6	2.3	7.6	2.4	7.7

- the reconstructed muons are oppositely charged.

In the *bbA* production mode, the BSM Higgs boson is produced in association with two b-quarks. The Z+jets background can be greatly reduced by b-tagging the resulting jets. To optimize the sensitivity of this search, events are categorized by the presence or absence of at least one b-tagged jet. These categories are labeled as "b-veto" and "b-tag", respectively.

8.4.3 Statistical analysis

Figure 8.10 shows the dimuon invariant mass spectrum after event selection. In order to determine the expected sensitivity to MSSM Higgs bosons, the background-only p_0-value expected for signal+background is calculated using the $m_{\mu\mu}$ spectrum. The production cross sections for $A \to \mu\mu$ and $H \to \mu\mu$ have been combined, as shown

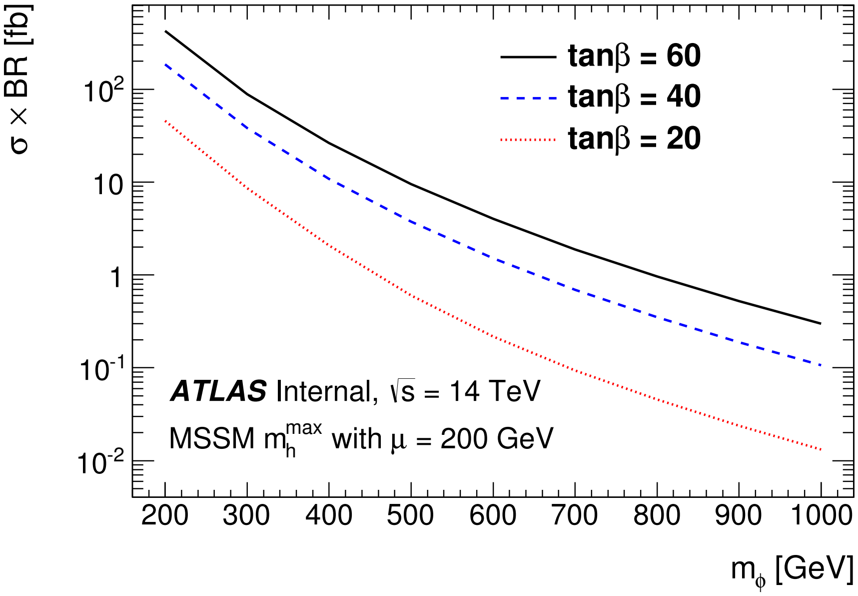

FIGURE 8.9: The MSSM $H/A \to \mu\mu$ cross section at $\sqrt{s} = 14$ TeV for three values of $\tan\beta$.

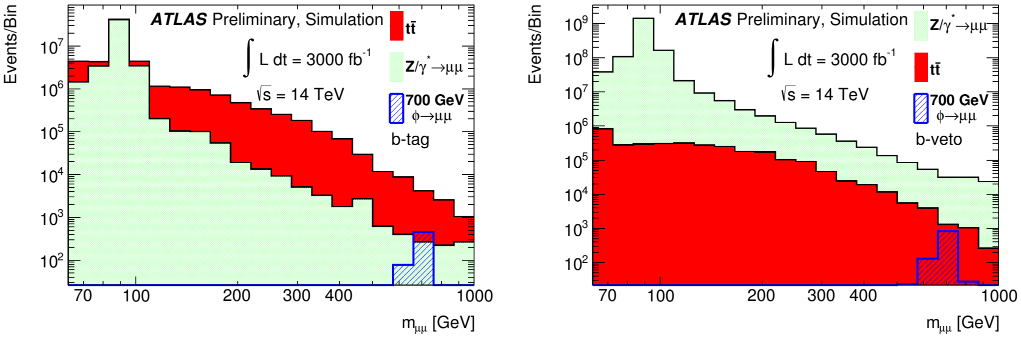

FIGURE 8.10: The dimuon invariant mass, $m_{\mu\mu}$, distribution is shown for the b-tag category (left) and the b-veto category (right). The signal assumed here corresponds to MSSM m_h^{max} with $m_\phi = 700$ GeV and $\tan\beta = 40$.

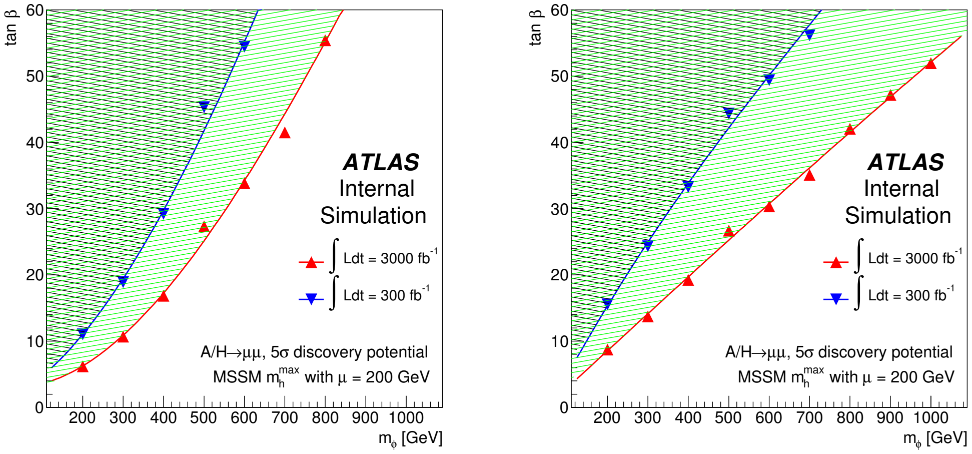

FIGURE 8.11: The 5-σ contours of the expected significance of an excess over the background for the $H/A \to \mu\mu$ search in the MSSM parameter space in the b-veto (left) and b-tag (right) categories.

in Fig. 8.9, under the assumption that the two bosons are degenerate in mass.

In Table 8.7 the p_0-values have been converted to the corresponding number of Gaussian σ in significance. The increase in significance with integrated luminosity is shown for different m_ϕ and $\tan\beta$ values. Only statistical uncertainties are used to determine the p_0-values. Figures 8.11 and 8.12 show the expected 5σ discovery region in the $(m_\phi,\, \tan\beta)$ plane for 300 fb^{-1} and 3000 fb^{-1} of integrated luminosity.

8.5 Conclusions

The results of many studies measuring the improvement in sensitivity to BSM physics at ATLAS with an integrated luminosity increase from 300 fb^{-1} to 3000 fb^{-1} have been presented in this chapter. A wide range of physics topics were covered by these studies, spanning extension to the electroweak sector manifest in vector boson scattering and fusion processes, exotic resonances, and BSM Higgs scenarios. With these and other results in hand, the high energy collider physics community can understand which analyses have the most to gain from the increased LHC dataset.

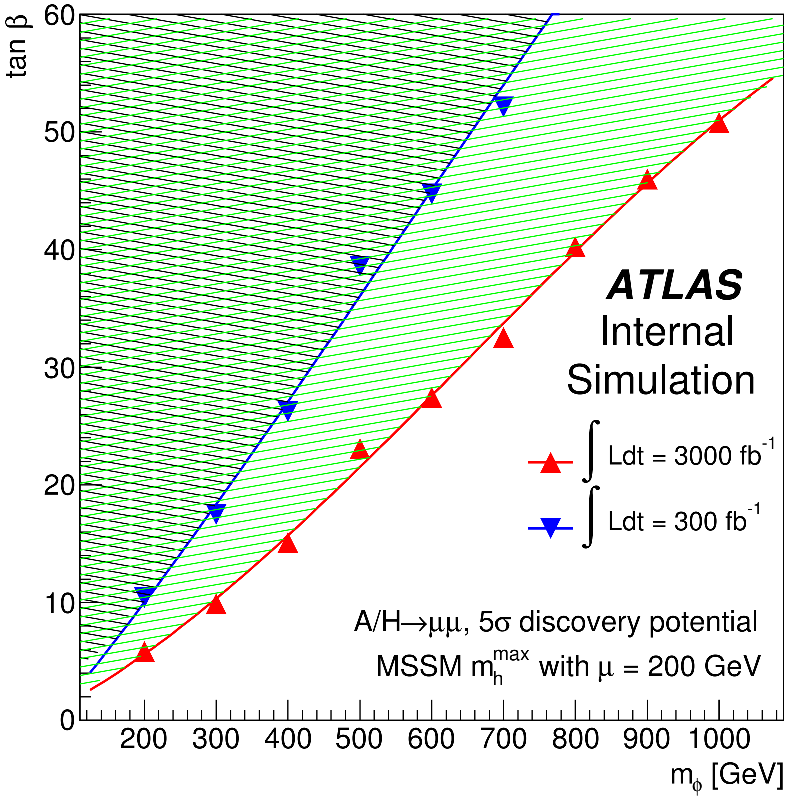

FIGURE 8.12: The 5-σ contours of the expected significance of an excess over the background for the $H/A \to \mu\mu$ search in the MSSM parameter space for the statistical combination of the b-tag and b-veto categories.

Bibliography

[1] S. Glashow, *Partial Symmetries of Weak Interactions*, Nucl.Phys. **22** (1961) 579–588.

[2] S. Weinberg, *A Model of Leptons*, Phys.Rev.Lett. **19** (1967) 1264–1266.

[3] A. Salam, *Weak and Electromagnetic Interactions*, Conf.Proc. **C680519** (1968) 367–377.

[4] ATLAS Collaboration, *Observation of a new particle in the search for the Standard Model Higgs boson with the ATLAS detector at the LHC*, Phys.Lett. **B716** (2012) 1–29, `arXiv:1207.7214 [hep-ex]`.

[5] CMS Collaboration, *Observation of a new boson at a mass of 125 GeV with the CMS experiment at the LHC*, Phys.Lett. **B716** (2012) 30–61, `arXiv:1207.7235 [hep-ex]`.

[6] C. Quigg, *Unanswered Questions in the Electroweak Theory*, Ann.Rev.Nucl.Part.Sci. **59** (2009) 505–555, `arXiv:0905.3187 [hep-ph]`.

[7] C. T. Hill, *Topcolor assisted technicolor*, Phys.Lett. **B345** (1995) 483–489, `arXiv:hep-ph/9411426 [hep-ph]`.

[8] C. T. Hill, *Topcolor: Top quark condensation in a gauge extension of the standard model*, Phys.Lett. **B266** (1991) 419–424.

[9] W. A. Bardeen, C. T. Hill, and M. Lindner, *Minimal Dynamical Symmetry Breaking of the Standard Model*, Phys.Rev. **D41** (1990) 1647.

[10] R. M. Harris and S. Jain, *Cross Sections for Leptophobic Topcolor Z' Decaying to Top-Antitop*, Eur.Phys.J. **C72** (2012) 2072, `arXiv:1112.4928 [hep-ph]`.

[11] R. M. Harris, C. T. Hill, and S. J. Parke, *Cross-section for topcolor Z-prime(t) decaying to t anti-t: Version 2.6*, `arXiv:hep-ph/9911288 [hep-ph]`.

[12] T. Kaluza, *Zum Unittsproblem in der Physik*, Sitzungsber. Preuss. Akad. Wiss. Berlin. (Math. Phys.) (1921) 966972.

[13] O. Klein, *Quantentheorie und fnfdimensionale Relativittstheorie*, Zeitschrift fr Physik A **37** (1926) 895–906.

[14] L. Randall and R. Sundrum, *A Large mass hierarchy from a small extra dimension*, Phys.Rev.Lett. **83** (1999) 3370–3373, `arXiv:hep-ph/9905221 [hep-ph]`.

[15] K. Agashe, A. Belyaev, T. Krupovnickas, G. Perez, and J. Virzi, *LHC Signals from Warped Extra Dimensions*, Phys.Rev. **D77** (2008) 015003, `arXiv:hep-ph/0612015 [hep-ph]`.

[16] G. A. Schuler and T. Sjostrand, *Hadronic diffractive cross-sections and the rise of the total cross-section*, Phys.Rev. **D49** (1994) 2257–2267.

[17] H1 and ZEUS Collaborations, *Proton structure functions at HERA*, Int.J.Mod.Phys.Conf.Ser. **31** (2014) 1460280.

[18] BCDMS Collaboration, A. Benvenuti et al., *A Comparison of the Structure Functions F2 of the Proton and the Neutron From Deep Inelastic Muon Scattering at High* Q^2, Phys.Lett. **B237** (1990) 599.

[19] E665 Collaboration, A. V. Kotwal, *Recent results from E665*, .

[20] CHORUS Collaboration, G. Onengut et al., *Measurement of nucleon structure functions in neutrino scattering*, Phys.Lett. **B632** (2006) 65–75.

[21] NuTeV Collaboration, M. Tzanov, *NuTeV structure function measurement*, AIP Conf.Proc. **792** (2005) 241–244, `arXiv:hep-ex/0507040 [hep-ex]`.

[22] A. Martin, W. Stirling, R. Thorne, and G. Watt, *Parton distributions for the LHC*, Eur.Phys.J. **C63** (2009) 189–285, `arXiv:0901.0002 [hep-ph]`.

[23] Particle Data Group Collaboration, K. Nakamura et al., *Review of Particle Physics, 2010-2011. Review of Particle Properties*, J. Phys. G **37** (2010) no. 7A, 075021.

[24] T. Han, *Collider phenomenology: Basic knowledge and techniques*, `arXiv:hep-ph/0508097 [hep-ph]`.

[25] M. Aliev, H. Lacker, U. Langenfeld, S. Moch, P. Uwer, et al., *HATHOR: HAdronic Top and Heavy quarks crOss section calculatoR*, Comput.Phys.Commun. **182** (2011) 1034–1046, `arXiv:1007.1327 [hep-ph]`.

[26] D. C. Tevatron Electroweak Working Group, CDF Collaboration, *Combination of CDF and DO results on the mass of the top quark using up to 8.7fb-1 at the Tevatron*, `arXiv:1305.3929 [hep-ex]`.

[27] S. S. A. Livermore and C. Issever, *A search for massive top quark resonances with the ATLAS detector at the Large Hadron Collider*. PhD thesis, Oxford U., Oxford, Jan, 2013. Presented 01 Mar 2013.

[28] ATLAS Collaboration, *The ATLAS Experiment at the CERN Large Hadron Collider*, JINST **3** (2008) S08003.

[29] ATLAS Collaboration, *The ATLAS Simulation Infrastructure*, Eur.Phys.J. **C70** (2010) 823–874, `arXiv:1005.4568 [physics.ins-det]`.

[30] M. L. Mangano, M. Moretti, F. Piccinini, R. Pittau, and A. D. Polosa, *ALPGEN, a generator for hard multiparton processes in hadronic collisions*, JHEP **0307** (2003) 001, `arXiv:hep-ph/0206293 [hep-ph]`.

[31] S. Frixione, P. Nason, and C. Oleari, *Matching NLO QCD computations with Parton Shower simulations: the POWHEG method*, JHEP **0711** (2007) 070, `arXiv:0709.2092 [hep-ph]`.

[32] C. Oleari, *The POWHEG-BOX*, Nucl.Phys.Proc.Suppl. **205-206** (2010) 36–41, `arXiv:1007.3893 [hep-ph]`.

[33] J. Alwall, R. Frederix, S. Frixione, V. Hirschi, F. Maltoni, et al., *The automated computation of tree-level and next-to-leading order differential cross sections, and their matching to parton shower simulations*, `arXiv:1405.0301 [hep-ph]`.

[34] T. Sjostrand, S. Mrenna, and P. Z. Skands, *PYTHIA 6.4 Physics and Manual*, JHEP **0605** (2006) 026, `arXiv:hep-ph/0603175 [hep-ph]`.

[35] G. Corcella, I. Knowles, G. Marchesini, S. Moretti, K. Odagiri, et al., *HERWIG 6.5 release note*, `arXiv:hep-ph/0210213 [hep-ph]`.

[36] A. Buckley, J. Butterworth, S. Gieseke, D. Grellscheid, S. Hoche, et al., *General-purpose event generators for LHC physics*, Phys.Rept. **504** (2011) 145–233, `arXiv:1101.2599 [hep-ph]`.

[37] B. Andersson, G. Gustafson, G. Ingelman, and T. Sjostrand, *Parton Fragmentation and String Dynamics*, Phys.Rept. **97** (1983) 31–145.

[38] B. Webber, *A QCD Model for Jet Fragmentation Including Soft Gluon Interference*, Nucl.Phys. **B238** (1984) 492.

[39] M. Asai, *Geant4-a simulation toolkit*, Trans.Amer.Nucl.Soc. **95** (2006) 757.

[40] J. Allison, K. Amako, J. Apostolakis, H. Araujo, P. Dubois, et al., *Geant4 developments and applications*, IEEE Trans.Nucl.Sci. **53** (2006) 270.

[41] J. Boudreau and V. Tsulaia, *The GeoModel Toolkit for Detector Description*, .

[42] T. Cornelissen, M. Elsing, S. Fleischmann, W. Liebig, E. Moyse, and A. Salzburger, *Concepts, Design and Implementation of the ATLAS New Tracking (NEWT)*, Tech. Rep. ATL-SOFT-PUB-2007-007. ATL-COM-SOFT-2007-002, CERN, Geneva, Mar, 2007.

[43] ATLAS Collaboration, *Performance of the ATLAS Inner Detector Track and Vertex Reconstruction in the High Pile-Up LHC Environment*, Tech. Rep. ATLAS-CONF-2012-042, CERN, Geneva, Mar, 2012.

[44] ATLAS Collaboration, *ATLAS Approved 2012 Beam Spot Plots*, https://twiki.cern.ch/twiki/bin/view/AtlasPublic/BeamSpotPublicResults .

[45] W. Lampl, S. Laplace, D. Lelas, P. Loch, H. Ma, et al., *Calorimeter clustering algorithms: Description and performance*, .

[46] ATLAS Collaboration, *Electron efficiency measurements with the ATLAS detector using the 2012 LHC proton-proton collision data*, Tech. Rep. ATLAS-CONF-2014-032, CERN, Geneva, Jun, 2014.

[47] ATLAS Collaboration, *Improved electron reconstruction in ATLAS using the Gaussian Sum Filter-based model for bremsstrahlung*, Tech. Rep. ATLAS-CONF-2012-047, CERN, Geneva, May, 2012.

[48] ATLAS Collaboration, *Preliminary results on the muon reconstruction efficiency, momentum resolution, and momentum scale in ATLAS 2012 pp collision data*, Tech. Rep. ATLAS-CONF-2013-088, CERN, Geneva, Aug, 2013.

[49] ATLAS Collaboration, *Jet energy resolution in proton-proton collisions at $\sqrt{s} = 7$ TeV recorded in 2010 with the ATLAS detector*, Eur.Phys.J. **C73** (2013) 2306, `arXiv:1210.6210 [hep-ex]`.

[50] S. D. Ellis and D. E. Soper, *Successive combination jet algorithm for hadron collisions*, Phys. Rev. **D48** (1993) 3160–3166, `arXiv:hep-ph/9305266 [hep-ph]`.

[51] ATLAS Collaboration, *Jet energy measurement and its systematic uncertainty in proton-proton collisions at $\sqrt{s} = 7$ TeV with the ATLAS detector*, `arXiv:1406.0076 [hep-ex]`.

[52] M. Cacciari and G. P. Salam, *Pileup subtraction using jet areas*, Phys.Lett. **B659** (2008) 119–126, `arXiv:0707.1378 [hep-ph]`.

[53] D. Krohn, J. Thaler, and L.-T. Wang, *Jet Trimming*, JHEP **1002** (2010) 084, `arXiv:0912.1342 [hep-ph]`.

[54] S. Catani, Y. L. Dokshitzer, M. Seymour, and B. Webber, *Longitudinally invariant K_t clustering algorithms for hadron hadron collisions*, Nucl.Phys. **B406** (1993) 187–224.

[55] ATLAS Collaboration, *Performance of large-R jets and jet substructure reconstruction with the ATLAS detector*, Tech. Rep. ATLAS-CONF-2012-065, CERN, Geneva, Jul, 2012.

[56] ATLAS Collaboration, *Performance of Missing Transverse Momentum Reconstruction in ATLAS studied in Proton-Proton Collisions recorded in 2012 at 8 TeV*, Tech. Rep. ATLAS-CONF-2013-082, CERN, Geneva, Aug, 2013.

[57] C. Collaboration, *Search for new particles decaying to $t\bar{t}$ in $p\bar{p}$ collisions at $\sqrt{s} = 1.8$ TeV*, Phys.Rev.Lett. **85** (2000) 2062–2067, `arXiv:hep-ex/0003005 [hep-ex]`.

[58] D. Collaboration, *Search for a Narrow $t\bar{t}$ Resonance in $p\bar{p}$ Collisions at $\sqrt{s} = 1.96$ TeV*, Phys.Rev. **D85** (2012) 051101, `arXiv:1111.1271 [hep-ex]`.

[59] ATLAS Collaboration, *A search for $t\bar{t}$ resonances with the ATLAS detector in 2.05 fb^{-1} of proton-proton collisions at $\sqrt{s} = 7$ TeV*, Eur.Phys.J. **C72** (2012) 2083, `arXiv:1205.5371 [hep-ex]`.

[60] ATLAS Collaboration, *A search for $t\bar{t}$ resonances in lepton+jets events with highly boosted top quarks collected in pp collisions at $\sqrt{s} = 7$ TeV with the ATLAS detector*, JHEP **1209** (2012) 041, `arXiv:1207.2409 [hep-ex]`.

[61] ATLAS Collaboration, *Search for $t\bar{t}$ resonances in the lepton plus jets final state with ATLAS using 4.7 fb^{-1} of pp collisions at $\sqrt{s} = 7$ TeV*, Phys.Rev. **D88** (2013) no. 1, 012004, `arXiv:1305.2756 [hep-ex]`.

[62] ATLAS Collaboration, *Prospects for top anti-top resonance searches using early ATLAS data.*, Tech. Rep. ATL-PHYS-PUB-2010-008, CERN, Geneva, Jul, 2010.

[63] T. Sjostrand, S. Mrenna, and P. Z. Skands, *A Brief Introduction to PYTHIA 8.1*, Comput. Phys. Commun. **178** (2008) 852–867, `arXiv:0710.3820 [hep-ph]`.

[64] H.-L. Lai, M. Guzzi, J. Huston, Z. Li, P. M. Nadolsky, et al., *New parton distributions for collider physics*, Phys.Rev. **D82** (2010) 074024, `arXiv:1007.2241 [hep-ph]`.

[65] M. Czakon and A. Mitov, *Top++: A Program for the Calculation of the Top-Pair Cross-Section at Hadron Colliders*, `arXiv:1112.5675 [hep-ph]`.

[66] B. P. Kersevan and E. Richter-Was, *The Monte Carlo event generator AcerMC versions 2.0 to 3.8 with interfaces to PYTHIA 6.4, HERWIG 6.5 and ARIADNE 4.1*, Comput.Phys.Commun. **184** (2013) 919–985, `arXiv:hep-ph/0405247 [hep-ph]`.

[67] *Calibration of b-tagging using dileptonic top pair events in a combinatorial likelihood approach with the ATLAS experiment*, Tech. Rep. ATLAS-CONF-2014-004, CERN, Geneva, Feb, 2014.

[68] *Calibration of the performance of b-tagging for c and light-flavour jets in the 2012 ATLAS data*, Tech. Rep. ATLAS-CONF-2014-046, CERN, Geneva, Jul, 2014.

[69] T. Chwalek, *Messung der W-Boson-Helizittsanteile in Top-Quark-Zerfllen mit dem CDF II Experiment und Studien zu einer frhen Messung des ttbar-Wirkungsquerschnitts mit dem CMS Experiment.* PhD thesis, Karlsruhe U., Karlsruhe, 2010. Presented 12 Feb 2010.

[70] ATLAS Collaboration, *Study of jets produced in association with a W boson in pp collisions at $\sqrt{s} = 7$ TeV with the ATLAS detector*, Phys.Rev. **D85** (2012) 092002, `arXiv:1201.1276 [hep-ex]`.

[71] C.-H. Kom and W. J. Stirling, *Charge asymmetry in W + jets production at the LHC*, Eur.Phys.J. **C69** (2010) 67–73, `arXiv:1004.3404 [hep-ph]`.

[72] M. Botje, J. Butterworth, A. Cooper-Sarkar, A. de Roeck, J. Feltesse, et al., *The PDF4LHC Working Group Interim Recommendations*, `arXiv:1101.0538 [hep-ph]`.

[73] R. D. Ball, V. Bertone, S. Carrazza, C. S. Deans, L. Del Debbio, et al., *Parton distributions with LHC data*, Nucl.Phys. **B867** (2013) 244–289, `arXiv:1207.1303 [hep-ph]`.

[74] ATLAS Collaboration, *Measurement of $t\bar{t}$ production with a veto on additional central jet activity in pp collisions at sqrt(s) = 7 TeV using the ATLAS detector*, Eur.Phys.J. **C72** (2012) 2043, `arXiv:1203.5015 [hep-ex]`.

[75] ATLAS Collaboration, *ATLAS Approved 2012 Jet Energy Scale Uncertainty Plots*, https://twiki.cern.ch/twiki/bin/view/AtlasPublic/JetEtmissApproved2013JESUncertainty .

[76] ATLAS Collaboration, *Jet mass and substructure of inclusive jets in $\sqrt{s} = 7$ TeV pp collisions with the ATLAS experiment*, JHEP **1205** (2012) 128, `arXiv:1203.4606 [hep-ex]`.

[77] G. Choudalakis, *On hypothesis testing, trials factor, hypertests and the BumpHunter*, `arXiv:1101.0390 [physics.data-an]`.

[78] D0 Collaboration, I. Bertram et al., *A Recipe for the construction of confidence limits*, .

[79] M. Cacciari, G. P. Salam, and G. Soyez, *FastJet User Manual*, Eur. Phys. J. **C72** (2012) 1896, `arXiv:1111.6097 [hep-ph]`.

[80] K. Rehermann and B. Tweedie, *Efficient Identification of Boosted Semileptonic Top Quarks at the LHC*, JHEP **1103** (2011) 059, `arXiv:1007.2221 [hep-ph]`.

[81] L. Rossi and O. Brning, *High Luminosity Large Hadron Collider A description for the European Strategy Preparatory Group*, Tech. Rep. CERN-ATS-2012-236, CERN, Geneva, Aug, 2012.

[82] A. Collaboration, *Letter of Intent for the Phase-I Upgrade of the ATLAS Experiment*, Tech. Rep. CERN-LHCC-2011-012. LHCC-I-020, CERN, Geneva, Nov, 2011.

[83] ATLAS Collaboration, *Performance assumptions based on full simulation for an upgraded ATLAS detector at a High-Luminosity LHC*, Tech. Rep. ATL-PHYS-PUB-2013-009, CERN, Geneva, Sep, 2013.

[84] ATLAS Collaboration, *Physics at a High-Luminosity LHC with ATLAS*, Tech. Rep. ATL-PHYS-PUB-2012-001, CERN, Geneva, Aug, 2012.

[85] C. ATLAS, *Letter of Intent for the Phase-II Upgrade of the ATLAS Experiment*, Tech. Rep. CERN-LHCC-2012-022. LHCC-I-023, CERN, Geneva, Dec, 2012. Draft version for comments.

[86] K. Agashe, O. Antipin, M. Backovi, A. Effron, A. Emerman, et al., *Warped Extra Dimensional Benchmarks for Snowmass 2013*, `arXiv:1309.7847 [hep-ph]`.

[87] J. Alwall, A. Ballestrero, P. Bartalini, S. Belov, E. Boos, et al., *A Standard format for Les Houches event files*, Comput.Phys.Commun. **176** (2007) 300–304, `arXiv:hep-ph/0609017 [hep-ph]`.

[88] F. Beaujean, A. Caldwell, D. Kollar, and K. Kroninger, *BAT: The Bayesian analysis toolkit*, J.Phys.Conf.Ser. **331** (2011) 072040.

[89] E. Accomando, A. Ballestrero, A. Belhouari, and E. Maina, *Isolating Vector Boson Scattering at the LHC: Gauge cancellations and the Equivalent Vector Boson Approximation vs complete calculations*, Phys.Rev. **D74** (2006) 073010, `arXiv:hep-ph/0608019 [hep-ph]`.

[90] A. Dobado, M. Herrero, J. Pelaez, and E. Ruiz Morales, *CERN LHC sensitivity to the resonance spectrum of a minimal strongly interacting electroweak symmetry breaking sector*, Phys. Rev. **D62** (2000) 055011, `arXiv:hep-ph/9912224 [hep-ph]`. (and references therein).

[91] A. Alboteanu, W. Kilian, and J. Reuter, *Resonances and Unitarity in Weak Boson Scattering at the LHC*, JHEP **0811** (2008) 010, `arXiv:0806.4145 [hep-ph]`.

[92] W. Kilian, T. Ohl, and J. Reuter, *WHIZARD: Simulating Multi-Particle Processes at LHC and ILC*, Eur.Phys.J. **C71** (2011) 1742, `arXiv:0708.4233 [hep-ph]`.

[93] P. Langacker, *The Physics of Heavy Z' Gauge Bosons*, Rev.Mod.Phys. **81** (2009) 1199–1228, `arXiv:0801.1345 [hep-ph]`.

[94] A. Djouadi, *The Anatomy of electro-weak symmetry breaking. II. The Higgs bosons in the minimal supersymmetric model*, Phys.Rept. **459** (2008) 1–241, `arXiv:hep-ph/0503173 [hep-ph]`.

[95] ATLAS Collaboration, *Search for the neutral Higgs bosons of the Minimal Supersymmetric Standard Model in pp collisions at $\sqrt{s} = 7$ TeV with the ATLAS detector*, JHEP **1302** (2013) 095, `arXiv:1211.6956 [hep-ex]`.

[96] L. H. C. S. W. Group
https://twiki.cern.ch/twiki/bin/view/LHCPhysics/MSSMNeutral .

Biography

Christopher Pollard was born 15 April 1986 in Springfield, Illinois, USA. He grew up in Harrison, Tennessee before receiving his bachelor's degree in physics from Yale University, New Haven, Connecticut in 2009. He performed his graduate research in high energy particle physics at Duke University in Durham, North Carolina.